IJAMMP

International Journal of
Advanced Manufacturing and Material Processing

Volume 1 | Issue 1

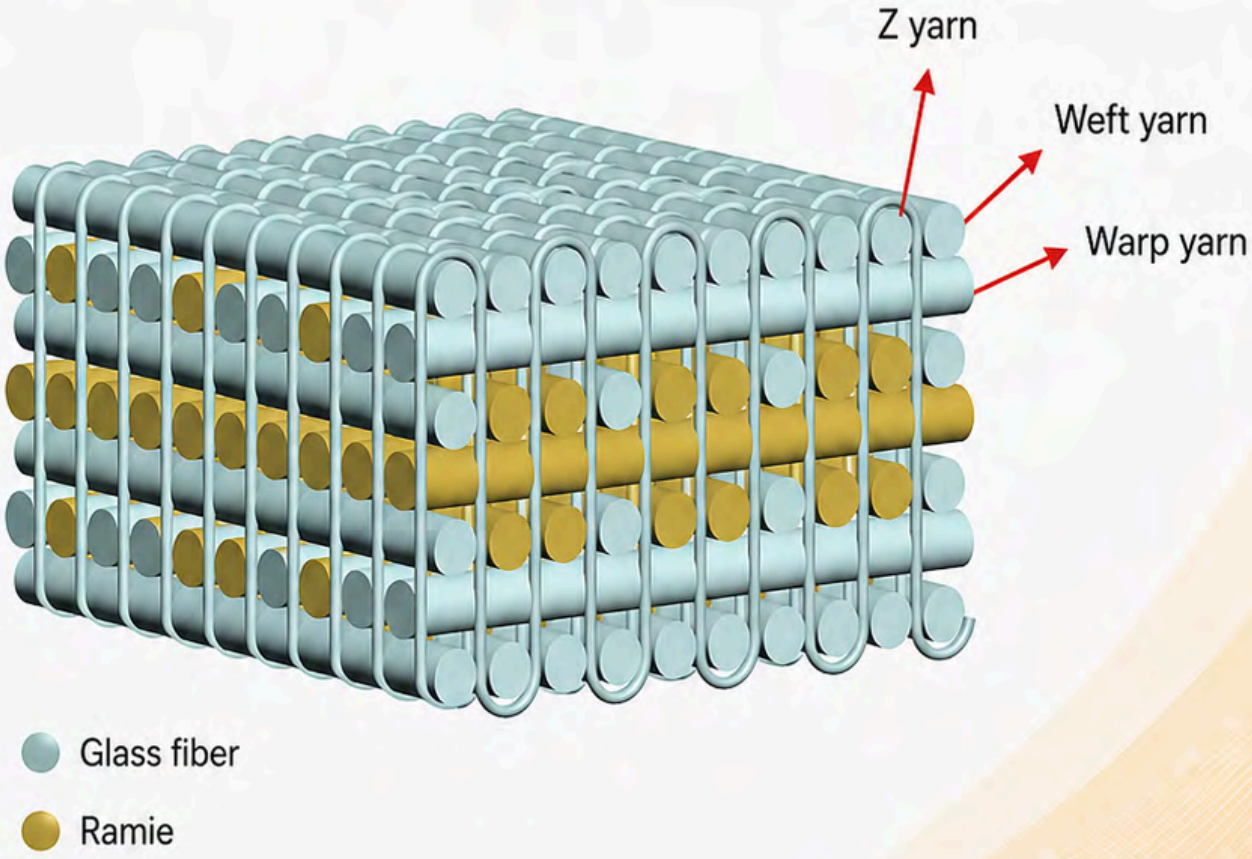

EDITORS
M.Hamdi
David Hui

Published twice yearly by
Centre of Advanced Manufacturing and Material Processing (AMMP Centre)
Universiti Malaya
50603 Kuala Lumpur
Malaysia

Edited by
Mohd Hamdi Abd Shukor
David Hui

M.Hamdi, David Hui (Eds.)

International Journal of Advanced Manufacturing and Material Processing

EDITORIAL BOARD

EDITORS-IN-CHIEF

EDITORS

EDITORIAL BOARD

MANAGING EDITOR

PREFACE

Volume 1, Issue 1 — Inaugural Issue, 2026

It is with great pleasure and a profound sense of purpose that we present this inaugural issue of the International Journal of Advanced Manufacturing and Material Processing (IJAMMP). Launched as a biannual publication, IJAMMP has been established to serve as a dedicated forum for original research, critical reviews, and practical advances at the intersection of manufacturing science, materials engineering, and processing technology.

The vision behind IJAMMP is rooted in a simple observation: modern manufacturing is no longer confined to a single discipline. It draws on metallurgy and polymer science, on mechatronics and data analytics, and increasingly on artificial intelligence, sustainability, and even the preservation of material culture. Through this journal we hope to bring together researchers, engineers, educators, and industry practitioners whose work cuts across these boundaries, and to share findings that inform both fundamental understanding and applied practice. We are particularly committed to publishing work that connects laboratory discovery to the shop floor and the classroom.

The contributions gathered in this first issue reflect that breadth. They span advanced materials characterization and provenance studies, the development and testing of hybrid fiber-reinforced composites, and new approaches to severe plastic deformation and metal forming. They examine joining technologies for both thin sheet steel and light alloys, and look toward the digital and intelligent factory through work on cooperative scheduling and vibration-based predictive maintenance. They also engage with the practical side of the discipline, from the design of teaching-oriented machine tools to a critical review of emerging directions in sheet metal forming.

Read alongside one another, these papers sketch the territory IJAMMP intends to cover: traditional craft and advanced characterization, conventional and severe forming, polymer composites and metallic alloys, arc welding and solid-state joining, intelligent scheduling and condition monitoring, and the equipment and pedagogy that underpin all of it. Although diverse in topic and method, the studies share a common orientation toward processes and materials that can be measured, modelled, optimised, and ultimately put to use.

We extend our sincere thanks to the authors who entrusted their work to a new journal at a moment when it had yet to prove itself, to the reviewers whose careful reading sharpened every manuscript, and to the editorial team and institutional supporters who made this launch possible. Further information about IJAMMP, its scope, editorial policies, and submission guidelines is available at https://ijammp.zecttron.com/.

As a biannual publication, IJAMMP will continue to evolve with the community it serves. We invite readers to engage critically with the articles that follow, and we warmly welcome submissions for forthcoming issues.

Mohd Hamdi Abd Shukor

Editor

CONTENTS

IJAMMP

Impact Properties of Three-Dimensional Orthogonal Woven Composites with Ramie/Glass Fiber Grid Hybridization

Han Shaokun,Yang Chunbing,Chen Wei, Zhang Liwen, Xu Fujun*

RESEARCH ARTICLE

ARTICLE INFO

Keywords:

Three-dimensional orthogonal woven composites; Grid hybridization; Low-velocity impact properties; Environmentally friendly; High damage tolerance

Article History

*Received:*24 October 2025
*Revised:*19 February 2026
*Accepted:*28 February 2026
Published: 15 June 2026

ABSTRACT

To enhance the damage tolerance of ramie fiber reinforced composites, a novel three-dimensional (3D) orthogonal structure with graded ramie/glass fiber hybridization (warp/weft gradient hybridization, Z-direction glass fiber reinforcement) was proposed. After the 3D orthogonal woven fabrics as preforms woven by a self-built 3D woven loom, the composites penetrated by epoxy resin were fabricated via vacuum-assisted resin transfer molding (VARTM). In this work, the impact properties of three-dimensional orthogonal woven composites with ramie/glass fiber grid hybridization were investigated. Compared to pure glass fiber reinforced three-dimensional orthogonal composites and traditional laminates, the grid hybrid composites showed highest peak force and smallest damage area under 15 J impact. Furthermore, the post-impact residual strength of grid hybrid composites showed highest strength retention rate (over 90%), indicating its superior ability to preserve load-bearing capacity after impact. Notably, the GH-3DOWC demonstrated superior damage tolerance, reducing the damage area by 61.5% and maintaining a compressive strength retention rate of over 90% under 15 J impact. This study demonstrated the advantages of the grid hybrid 3D composites reinforced by ramie and glass fibers, providing new insights for developing low-cost, high-damage-tolerance green engineering materials.

1. Introduction

Three-dimensional orthogonal woven fabric (3DOWF), characterized by its unique interlocking structure with Z-direction yarns along the thickness, significantly mitigates the weaknesses of traditional laminated composites such as weak interlaminar performance and susceptibility to delamination (Boroomand et al.,2023; Hu et al, 2020; Zhao et al. , 2024). This structure enables the Z-direction fibers to effectively bridge cracks and suppress damage propagation when the composite is subjected to impact or shear loads. It has found widespread applications in high-strength and high-reliability fields including aerospace (engine nacelles, radomes), wind power (shear webs for blades), and transportation (lightweight crash-resistant structures). Compared to two-dimensional laminates, the 3D orthogonal structure demonstrates revolutionary potential in damage tolerance, particularly in suppressing barely visible impact damage (BVID) caused by low-velocity impacts (e.g., tool drop, bird strike) (Bulut & Erkliğ, 2017; Kim & Park, 2021; Umair et al., 2022).

Key Laboratory of Textile Science & Technology, Ministry of Education, College of Textiles, Donghua University, China

*Corresponding author : fjxu@dhu.edu.cn

To further optimize performance and cost, researchers have attempted to hybridize high-performance synthetic fibers (e.g., glass, carbon fibers) with natural fibers (e.g., flax, bamboo) to create 3DOWF. However, current researches face two key challenges: a lack of studies on dynamic impact performance and oversimplified hybrid structural designs. Existing literatures primarily focuses on static mechanical properties (tensile, flexural) or quasi-static interlaminar shear strength (ILSS) (Niu et al., 2025; Ramakrishnan, Ramnath, Elanchezhian, Kumar, & Gowtham, 2018), with insufficient attention paid to low-velocity impact behavior. Furthermore, most current studies adopt uniform hybridization, where different fibers are evenly distributed within the fabric (Fazeli, Kern, Hoffmann, & Cherif, 2015; Singh, Singh, & Gill, 2018; Wang et al., 2017). This design struggles to reconcile conflicting requirements: high-modulus fibers (e.g., glass) need to bear the primary load, while high-toughness fibers (e.g., flax) should maximize energy absorption (Kuang et al., 2018; M. Li, Wang, Boussu, & Soulat, 2020; Wang et al., 2017).

The incorporation of natural fibers contributes not only to reduced density and cost, but also enhances toughness, damping, and energy absorption. For instance, flax/glass hybrids improve post-impact residual strength in laminates,

while bamboo/carbon systems enhance damage tolerance without compromising stiffness. Nevertheless, prevailing research predominantly focuses on uniform hybridization, wherein fibers are distributed evenly or randomly throughout the composite. Although such configurations offer certain performance trade-offs, they often fail to achieve optimal functional synergy between high-stiffness and high-toughness fibers under impact loading.

By contrast, gradient or non-uniform hybridization allows for tailored performance through controlled variations in fiber type, content, and arrangement along the thickness direction. This approach promotes more regulated and progressive damage propagation, thereby improving damage tolerance and energy absorption efficiency. However, existing studies on gradient hybridization remain largely confined to conventional laminates and quasi-static conditions, leaving the underlying mechanisms in three-dimensional orthogonal woven composites under dynamic impact insufficiently explored.

Furthermore, low-velocity impact testing is of paramount importance for evaluating the mechanical properties of composite materials. Such testing not only serves as a fundamental method for assessing a composite's resistance to external accidental loads, but also constitutes a crucial experimental step for revealing the mechanism by which three-dimensional integral structures suppress delamination, and for verifying the effectiveness of gradient hybrid designs in enhancing impact energy dissipation and damage tolerance.

Inspired by the concept of non-uniform hybridization, this paper designs and fabricates a grid hybrid three-dimensional orthogonal woven fabric (GH-3DOWF) based on hybrid 3DOWF, and prepares grid hybrid three-dimensional orthogonal woven composite (GH-3DOWC) using VARTM. The study focuses on their mechanical properties and failure modes under low-velocity impact.

Additionally, all glass plain-woven composite (AG-PWC) and all-glass 3D orthogonal woven composites (AG-3DOWC) are fabricated for comparison, to investigate the influence of different structures and materials on their low-velocity impact performance. This experiment employed the method of mean and standard deviation for standardisation.

2. Structure design and experiment method

2.1 Raw materials

The GH-3DOWF was produced using E-glass fibers (model EDR13-300-386, supplied by China Ju shi Co., Ltd.) and 9-ply ramie yarns (provided by Shanghai Zhang dan Garment Accessories Co., Ltd.). The resin matrix system consisted of bisphenol-A epoxy resin (model JL-235, epoxy value 0.56 mol/100g) and hardener (model JH-242), both produced by Hangmo Jiafa New Materials (Suzhou) Co., Ltd.

2.2 Structure design

Fig.1 illustrates the structural schematic of the GH-3DOWF. The glass fiber content progressively decreases from 100% at the top layer to 0% at the core layer (e.g., the second layer achieves 67% glass fiber content through alternating arrangements of two glass fibers and one ramie yarn per pattern repeat), then symmetrically increases toward the bottom layer, creating a grid hybridization. Z-direction yarns, exclusively glass fibers, interlace to bind the warp and weft yarns, thereby enhancing delamination resistance. Table 1 summarizes the detailed weaving parameters of the GH-3DOWF.

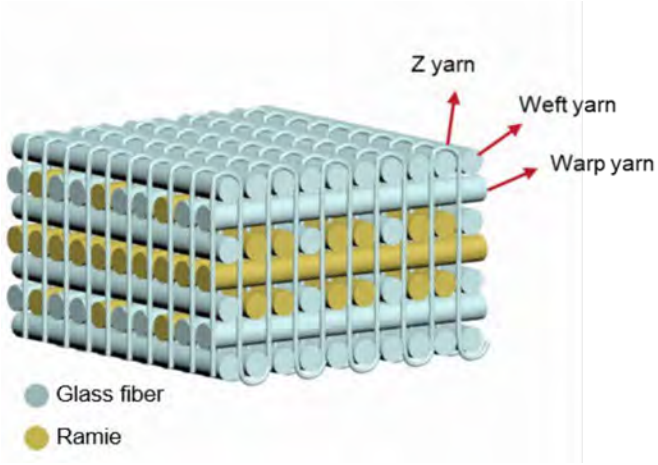

Figure 1. Structural schematic of the GH-3DOWF

Table 1. Specific weaving parameters of GH-3DOWF

Name	First Layer	Second Layer	Third layer	Forth layer	Fifth layer	Sixth layer	Seventh layer
AG-3DOWF	G	G	G	G	G	G	G
GH-3DOWF	G	G/R (67:33)	G/R (33:67)	R	G /R (33:67)	G /R (67:33)	G

2.3 Fabrication and molding of 3DOWF

The weaving process of the 3DOWF is illustrated in Fig.2. The warp yarns and Z-yarns also called pillar yarns are drawn from the creel, pass through the reed, and interlace/bind with the weft yarns by controlling the movement of the heddle frames, forming an integrated three-dimensional textile structure.The GH-3DOWC were fabricated using VARTM, with the specific molding process illustrated in Fig.3. Pre-cure at 50°C for 3 hours, then heat to 70°C for a further 7 hours to complete curing.Detailed composite material parameters as the Table 2.

Table 2. Composite Material Parametes

Name	Fiber volume fraction	Density	Thickness
GH-3DOWC	48%	1.45g/cm^3	5.43mm
AG-3DOWC	45%	1.88g/cm^3	4.32mm
AG-PWC	52%	1.92g/cm^3	4.53mm

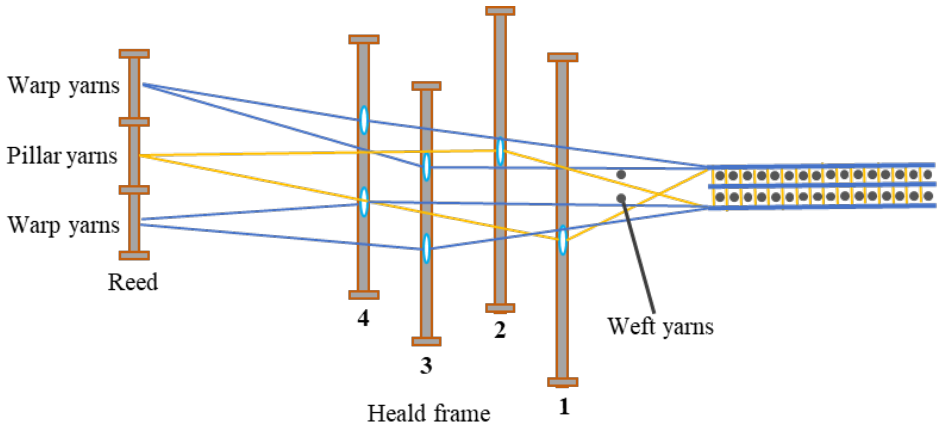

Figure 2. Weaving Process of 3DOWF

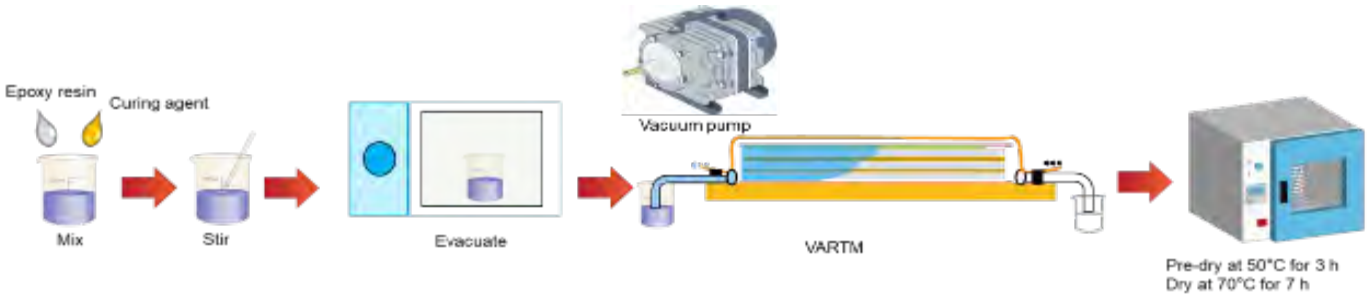

Figure 3. Process schematic of for VARTM

2.4 Low-velocity impact testing

Low-velocity impact tests were conducted on a drop-weight impact tester (Xusai) in accordance with ASTM D7136/D7136M (Standard Test Method for Measuring the Damage Resistance of a Fiber-Reinforced Polymer Matrix Composite to a Drop-Weight Impact Event). Specimen dimensions were 100 mm × 100 mm, with three parallel samples tested per group.

2.5 Post-impact residual strength testing

The post-impact residual strength was determined by measuring the transverse compressive strength of the impacted specimens. Tests were performed on a universal testing machine (INSTRON, Model 5967) in accordance with ISO 14126 and ASTM D7137/D7137M (Standard Test Method for Compressive Residual Strength Properties of Damaged Polymer Matrix Composite Plates).

For comparison with the pre-impact compressive strength, the impacted specimens were trimmed to dimensions of 100 mm × 58 mm. A constant loading rate of 2 mm/min was applied, with three parallel specimens tested per group. The instrumentation and testing methodology are presented in Fig.4.

3. Results and analysis

3.1 Contact force-time curves of the impact test

Fig.5 shows the fabricated GH-3DOWC sample and its cross-sectional views. The ramie fiber and glass fiber showed good interface adhesion in GH-3DOWC. Fig.6 presents the force-time curves of materials under 15J low-velocity impact. As shown in picture, the curve of AG-3DOWC is characterized by the highest peak force (approximately 3700 N), yet it is followed by a sharp decline, indicating that the material primarily resists impact through high stiffness and undergoes catastrophic failure

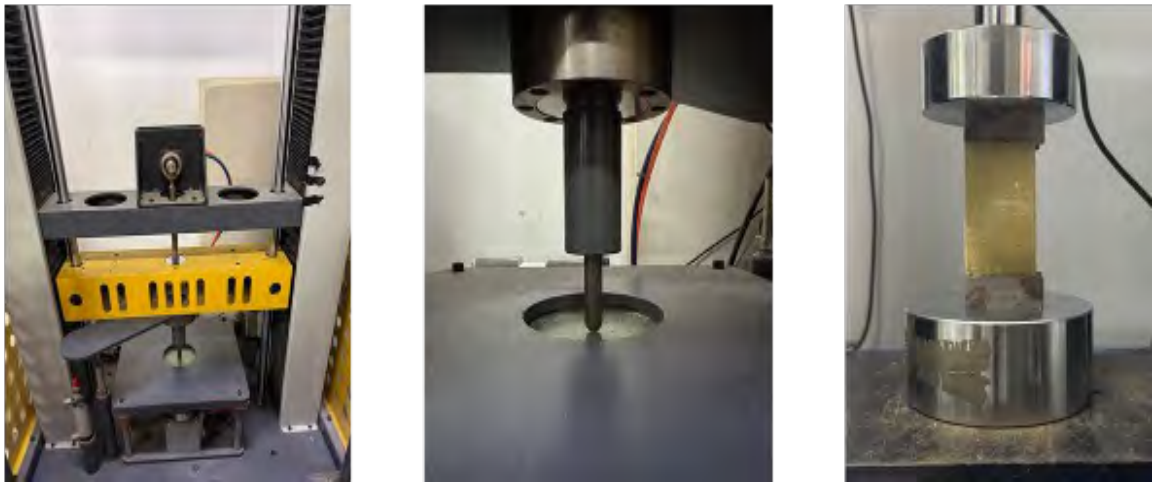

(a) (b) (c)

Figure 4. (a) Low-velocity impact instrument, (b) Impact process, (c) The process of post-impact residual strength testing

due to brittle fracture. In contrast, the AG-PWC displays the gentlest curve with a lower peak force (approximately 3300 N) and a broad force plateau. The GH-3DOWC exhibits a curve intermediate between the other two, with the lowest peak force (approximately 3000 N) but a more gradual post-peak decay, demonstrating superior toughness. This reflects the synergistic effect of ramie fibers and the three-dimensional gradient structure, facilitating a multi-stage energy absorption process involving mechanisms from fiber fracture to pull-out, thereby enhancing the material's damage tolerance and energy absorption efficiency.

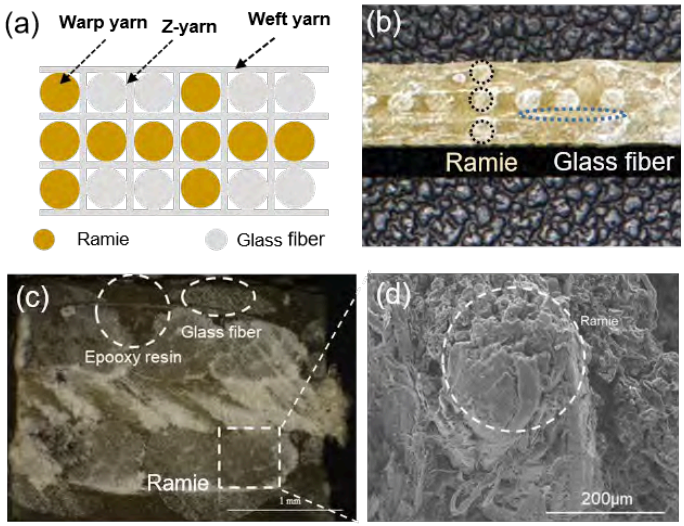

Figure 5. GH-3DOWC: (a) Schematic diagram and (b) Picture of Warp-direction view , (c) Amplified picture and (d) its SEM image of cross-sectional view

3.2 Analysis of impact damage morphology

Fig.7 show the surface damage morphology of the GH-3DOWC, the AG-3DOWC, and the AG-PWC after 15 J impact tests. The 15 J impact led to increased damage severity and larger surface damage areas in all three composite materials.

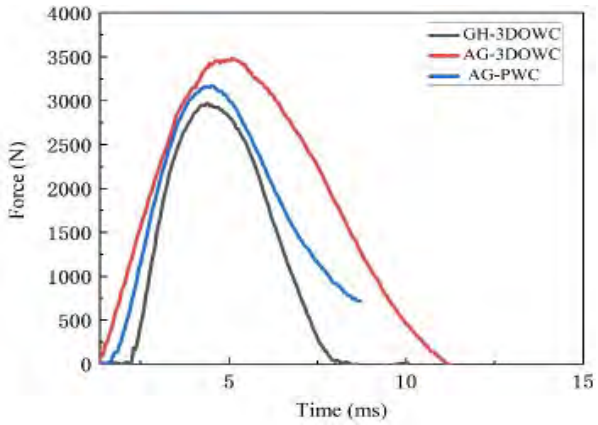

Figure 6. Impact contact force-time curves of composites under 15J impact energy

The GH-3DOWC exhibited enlarged resin whitening zones on the upper surface. Similarly, both the AG-3DOWC and the AG-PWC showed expanded resin whitening areas, with the latter also developing a deeper impact-induced depression. When comparing the PW-GFL, the AG-3DOWC, and the ramie-integrated GH-3DOWF, a clear reduction in both the extent of damage and the affected surface area was observed.

The damage area on the upper surface was quantified using Image-J analysis software. As shown in the magnified views of the damaged regions, the GH-3DOWC exhibited significantly less damage compared to the other two materials. Both the AG-3DOWC and the AG-PWC showed extensive surface resin damage, with measured damage areas of 45.273 mm² and 61.129 mm² under 15 J impact, respectively. In contrast, the GH-3DOWC displayed only minor surface resin damage at 15 J. None of the three composite types experienced full penetration of the upper surface, though they exhibited varying degrees of surface damage. The lower surface of the grid hybrid composite showed slight resin damage, while the other two materials displayed more pronounced damage traces.

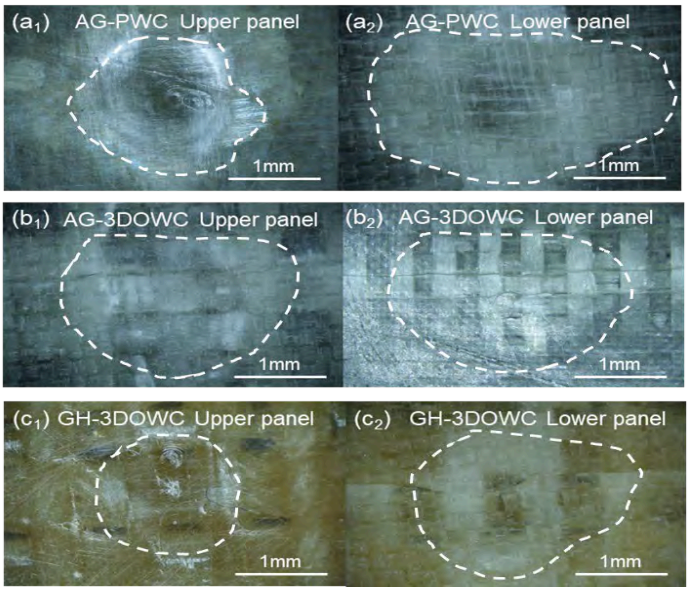

Figure 7. Panel damage morphology: (a_1) AG-PWC Upper panel, (a_2) PW-GFL Lower panel, (b_1) AG-3DOWC Upper panel, (b_2) AG-3DOWC Lower panel, (c_1) GH-3DOWC Upper panel (c_2) GH-3DOWC Lower panel

3.3 Post-impact residual strength

Fig.8 presents the post-impact residual strength test results of the composites. Fig.8 (a) compares the transverse compressive strength after 15 J impacts with the original (pre-impact) transverse compressive strength for the GH-3DOWC, the AG-3DOWC, and the AG-PWC. Fig.8 (b) shows the corresponding compressive strength retention rates after impact at these energy levels. As observed in the figure, all composites exhibited a noticeable decrease in transverse compressive strength due to impact damage. Furthermore, the extent of strength reduction increased with higher impact energy, leading to a corresponding decline in the strength retention rate. Owing to its minimized damage during impact, the GH-3DOWC demonstrated a significantly higher retention of transverse compressive strength compared to the AG-3DOWC and the AG-PWC. Its strength retention reached 95.54% after the 15 J impact—far exceeding the values of the other two composites. In contrast, the plain-woven glass fiber laminate exhibited severe damage on both the upper and lower panels after the 15 J impact, resulting in a strength retention of only 81.57%.

4. Conclusions

In this work, a grid hybrid three-dimensional orthogonal woven composite (GH-3DOWC) reinforced by ramie and glass fiber were designed and fabricated. Then the mechanical performance under low-velocity impact as well as their post-impact residual strength were investigated. The main conclusions are as follows:

The 3D orthogonal woven structure showed significantly improved impact resistance compared to traditional laminates.

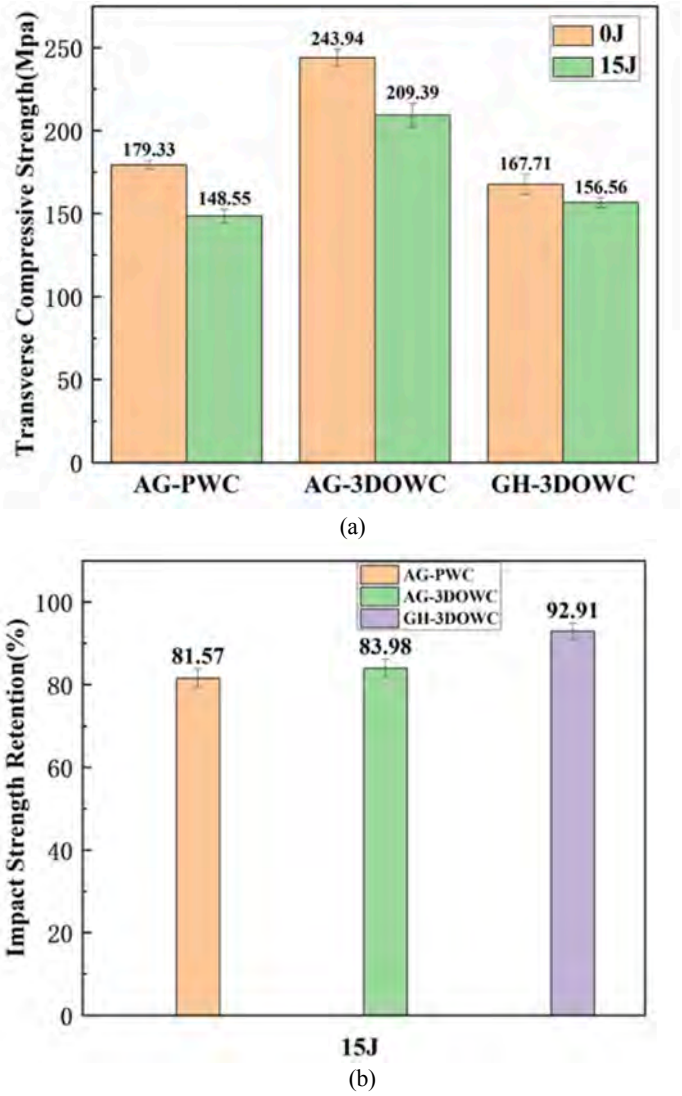

Figure 8. Post-impact residual strength of composites: (a) Lateral compressive strength before and after impact, (b) Strength retention

The GH-3DOWC showed higher peak force under 15 J impact, attributed to the synergistic effect of its 3D orthogonal architecture and grid glass/ramie hybrid design on overall rigidity. The lower peak of the GH-3DOWC indicates a softer initial response.The Z-yarn reinforcement also endowed the AG-3DOWC with superior stiffness over the AG-PWC.The post-peak force decay reveals the damage evolution.

Compared with AG-3DOWC the damage area of GH-3DOWC was reduced by 25.9% under 15 J impact. Furthermore, the grid hybrid 3DOWF incorporating ramie fibers demonstrated even greater improvement, reducing the damage area by 61.5% compared to conventional laminates. The residual strength of both the AG-3DOWC and the AG-PWC fell below 85% strength retention under 15 J impact, while the GH-3DOWC maintained over 90% strength retention, indicating its superior ability to preserve load-bearing capacity after impact. The fibrillation fracture of hemp fibres in the SEM image resulted in lower peaks and reduced damage area for GH-3DOWC.

References

Boroomand, M. H., Alamdar-Yazdi, A., & Ahmadi, M. S. (2023). Numerical simulation of tensile, flexural, and impact behavior of three dimensional orthogonal hybrid jute/HTPET woven fabric composites. *The Journal of The Textile Institute*. doi:10.1080/00405000.2023.2272789

Bulut, M., & Erkliğ, A. (2017). An experimental investigation on damage characteristics of laminated hybrid composites subjected to low velocity impact. *Polymer Composites*. doi:10.1002/pc.24319

Fazeli, M., Kern, M., Hoffmann, G., & Cherif, C. (2015). Development of three-dimensional profiled woven fabrics on narrow fabric looms. *Textile Research Journal*. doi:10.1177/0040517515606361

Hu, Y., He, Z., & Xuan, H. (2020). Impact Resistance Study of Three-Dimensional Orthogonal Carbon Fibers/BMI Resin Woven Composites. *Materials*. doi:10.3390/ma13194376

Kim, H., & Park, J. (2021). Improved Modeling Method for 3-Dimensional Woven Composites Using Weaving Parameters. *International Journal of Aeronautical and Space Sciences*. doi:10.1007/s42405-021-00365-z

Kuang, Y., Yao, L., Yu, S.-H., Tan, S., Fan, X.-J., & Qiu, Y.-P. (2018). Design and Electromagnetic Properties of a Conformal Ultra Wideband Antenna Integrated in Three-Dimensional Woven Fabrics. *Polymers*. doi:10.3390/polym10080861

Li, M., Wang, P., Boussu, F., & Soulat, D. (2020). A review on the mechanical performance of three-dimensional warp interlock woven fabrics as reinforcement in composites. *Journal of Industrial Textiles*. doi:10.1177/1528083719894389

Li, Y., Li, L., Li, Y., Wang, H., Wang, P., & Zhang, Y. (2023). The through-thickness thermal conductivity and heat transport mechanism of carbon fiber three-dimensional orthogonal woven fabric composite. *The Journal of The Textile Institute*. doi:10.1080/00405000.2023.2201029

Niu, Z., Li, W., Huang, Y., Liu, Y., Xu, W., & Ouyang, Y. (2025). Preparation and improved mechanical properties of three-dimensional woven fabrics reinforced thermoplastic composites based on intra-yarn hybrid flax/basalt fibers. *Industrial Crops and Products*. doi:10.1016/j.indcrop.2025.121957

Ramakrishnan, G., Ramnath, B. V., Elanchezhian, C., Kumar, A. A., & Gowtham, S. (2018). Investigation of Mechanical Behaviour of Basalt-Banana Hybrid Composites. *Silicon*. doi:10.1007/s12633-018-0009-8

Singh, S., Singh, R., & Gill, S. S. (2018). Investigations for Surface Hardness of Aluminum Matrix Composites with Hybrid Reinforcement. *Transactions of the Indian Institute of Metals*. doi:10.1007/s12666-018-1472-z

Umair, M., Hussain, M., Shaker, K., & Nawab, Y. (2022). Impact Performance of Three-dimensional Woven Composites with Novel Binding Yarn Patterns. *Journal of Natural Fibers*. doi:10.1080/15440478.2022.2064399

Wang, W., Zhu, J., Zhang, R., Li, Y., Ji, F., & Yu, J. (2017). Numerical characterization and simulation of the three-dimensional tubular woven fabric. *Journal of Industrial Textiles*. doi:10.1177/1528083717720206

Zhao, S., Chen, L., Gao, Z., & Wang, J. (2024). Bending fatigue performance of three-dimensional woven composites—A review. *Polymer Composites*. doi:10.1002/pc.28951

IJAMMP

Determination of Kendi's Provenance Through the Panofsky Approach and Combination of Handheld Raman Spectroscopy, X-Ray Fluorescence

Md Saifur Rahman[1], A R Bushroa[2,3,*], Hendrik Simon Cornelis Metselaar[2,4], SZ Salleh[3], Geneviève Gamache[5], Raja Jamilah Raja Yusof[6] and Faridah Noor Mohd Noor[7]

RESEARCH ARTICLE

ARTICLE INFO

Keywords:

Ceramic Kendi; Ming Dynasty; Provenance Study; Panofsky Method; X-Ray Fluorescence Analysis

Article History

Received:24 October 2025
Revised:19 February 2026
Accepted:28 February 2026
Published:

ABSTRACT

This study focuses on ceramic artifacts, specifically Kendi I and Kendi II, housed in the Museum of Asian Art (MoAA) at Universiti Malaya. The artifacts exhibit similarities that complicate their originality, authenticity, age, and provenance assessments. To address this, the research integrates both art historical analysis and scientific material characterization. Employing Panofsky's approach, the study analyzes ceramic types and decorative elements-colors, patterns, and shapes-reflecting the expected dynasty's reign. Concurrently, modern scientific techniques, including portable X-Ray Fluorescence (XRF) and handheld Raman Spectroscopy, are used to identify the chemical compositions (silica, alumina, and various fluxing agents) and mineralogical phases (quartz, mullite, anatase, albite). Raman peaks indicative of quartz and albite, along with XRF ratios aligning with known Ming Jingdezhen compositions, support the findings. The combined data from both analytical methods suggest that Kendi I likely originated from Jingdezhen during the Ming Dynasty, with Kendi II potentially having the same origin. The robust evidence from Panofsky's approach and material characterization helps clarify ambiguities regarding the artifacts' originality.

1. Introduction

Archaeological ceramic artefacts are typically kept as collections at universities, museums, or other institutions. The Museum of Asian Art (MoAA) at Universiti Malaya holds among the largest public collection of ancient kendi, with 156 kendis and 24 related vessels. The MoAA collection of ancient kendi is believed to originate from various countries in East and South-East Asia including Cambodia, China, India, Indonesia, Japan, Pakistan, Thailand, and Vietnam. Protection and conservation of rare specimens are for display and future research (Khoo and Rooney, 1991). For these reasons, MoAA kendi collection is continuously being studied, reassessed, and perfected through re-cataloguing, research, and exhibitions.

1 Department of Industrial and Production Engineering, National Institute of Textile Engineering and Research, Dhaka-1350, Bangladesh
2 Mechanical Engineering, Faculty of Engineering, Universiti Malaya, 50603 Kuala Lumpur, Malaysia
3 Centre of Advanced Manufacturing and Material Processing, Faculty of Engineering, Universiti Malaya, 50603, Kuala Lumpur, Malaysia
4 Centre of Advanced Materials, Faculty of Engineering, Universiti Malaya, 50603, Kuala Lumpur, Malaysia
5 Cultural Center, Universiti Malaya, 50603, Kuala Lumpur, Malaysia
6 Software Engineering, Faculty of Computer Science and Information Technology, Universiti Malaya, 50603, Malaysia
7 Culture Working Group, Asia Pacific Advanced Network (APAN), Room 101, Block B, Cyberport 4100, Cyberport Road, Hong Kong
*Corresponding author : bushroa@um.edu.my

Kendi is a liquid-holding and pouring pitcher with a spout that is positioned diagonally between the body and shoulders to facilitate pouring. This shape is widely known across East and Southeast Asia, with special historical significance in the latter region. Despite its significance, little is known about kendi (Cort, 2017). The uniformity of pottery in terms of form, look, and quality may imply local manufacturing, according to archeological data (Lahlil etal., 2009). Ceramic identification is essential for archaeological research because ceramic fragments can provide information about the sources of clay and the tools used (Xanthopoulou et al., 2020).

Art historical techniques are a well-established method for artefact identification, assessing formal qualities, provenance, and context. Many methods have been used, including Panofsky's three-stage analysis (Iconographical Description, Iconographical Analysis, and Iconological Interpretation) (Abdullah et al., 2020; Franklin and Boak, 2019). According to Dias et al. (2013) and Ionescu and Hoeck (2020), traditional identification focuses on visual inspection of shape, decoration, color, texture, and manufacturing style, but it can be unreliable and inconsistent (Ionescu and Hoeck, 2020; Dias et al., 2013).

Scientific characterization supplements traditional methods by providing objective data on raw materials, production techniques, and provenance. Crystalline structures, chemical composition, thermal stability, and microstructural changes in ceramics can be revealed by methods like Fourier Transform Infra-Red (FTIR), Raman Spectroscopy, X-Ray Diffraction (XRD), and Therma Gravimetric Analysis (TGA) (Xanthopoulou et al., 2020; Maritan, 2020; Montana, 2020; Gliozzo, 2020, Liu et al., 2023). For dating and determining origin, geochemical study of glazes and ceramic bodies is especially helpful (Bronitsky, 1986; Pollard and Hatcher, 1994; Pradell and Molera, 2020). Current research shows how integrating scientific analysis with art historical approaches improves knowledge of provenance, cultural context, and ceramic technology (Freitas et al., 2018; Botticelli et al., 2020; Quinn, 2018).

The MoAA kendi collection, which was catalogued by Oxford University Press in 1991 (Khoo and Rooney, 1991), contains a lot of information on the nation and time period. The provenance and authenticity of these vessels can be further ascertained by examining the quality of the raw materials, decorative elements, and production processes. Using both art historical and scientific methodologies, this study attempts to forecast the authenticity, age, and provenance of certain kendi vessels. The goal of the combined method is to provide a more precise understanding of these old artifacts while also reducing ambiguity.

2. Materials and Methods

This study focused on two East Asian kendi vessels that were identified from the 1990's catalogue of which their exact site of origin had not been identified with certainty. There were two types of kendi provided by the MoAA catalogue. The first vessel, Kendi I, (Serial number UM 78.774), was identified in the catalogue as a Ming Dynasty (1368-1644 CE) porcelain of the late 15th century. This was a miniature kendi with a dimension of 7.5 cm height X 8.2 cm depth. It had a distinctive spout in the shape of a hen's head with a decorative tail on the opposite shoulder as shown in Fig 1. It had a cup-shaped neck with flaring lips and broad shoulders, with a thick body and unglazed foot. It was decorated with a greyish blue and white underglaze decorated with tendrils, buds, and flowers (Khoo and Rooney, 1991). As shown in Fig 2, the second vessel is Kendi II (Serial number UM 78.646), identified in the 1991 catalogue as a 17th century celadon porcelain ware with a dimension of 17 cm height X 9.7 cm depth. The globular body, tall tubular neck, mammiform spouts, dry foot ring, and glazed base had an embossed ring and ribbed decoration (Khoo and Rooney, 1991).

The provenance of the two ancient ceramic kendi vessels were identified by using two combined methods, namely, Panofsky's approach and devices for materials characterization. The three stages in Panofsky's approach consist of iconographical description, iconographical analysis, and iconological interpretation (Cui, 2017).

Figure 1. Kendi I (Serial number: UM 78.774) Late 15th century porcelain

Figure 2. Kendi II (Serial number: UM 78.646) 17th century celadon porcelain.

For Kendi I, notable features include a globular body, distinct mouth shape, ruyi lappets on the shoulders, thin-lined foot, and blue-and-white glaze marked by crazing and grey weathered spots. Kendi II showcases a globular body with a tall tubular neck and mammiform spouts, ribbed decorations, and a solid light-greenish celadon body. Applying Panofsky's approach, observations made on the vessels were determined and defined visuals and highlighted any prior literary, cultural, or artistic features. The historical approach was employed to look into civilizations, classes, societal attitudes, and philosophical and theological viewpoints. Consequently, the origin of the kendi can be predicted by reconstructing and understanding the development of art history.

The body and glaze signature of the kendi were recorded using a handheld Rigaku ResQ Raman Spectrometer with an advanced 1064 nm excitation laser to acquire Raman spectra at 9-10.5 cm-1 resolution over a spectra range of 200-2500 cm-1. The measurements were performed on the glazed surface region of the body and the rim at the bottom of each kendi. The total observation time is 15 seconds with an exposure time of 2000 ms for all cases. Well-defined crystalline phases were revealed, and the peaks for specific atom bonding were correlated to the existence of chemical compounds in the body and the glaze of the vessels.

In addition to the Raman spectroscopy, the aforementioned evidence was supported by utilizing devices such as the handheld X-Ray Fluorescence (XRF). It extracted material components in the body and on the surface of the kendi. The XRF enabled the identification of any heavy metal oxide presence within the body of the kendi. The XRF was performed using the Thermo Scientific Niton XL3T Goldd+ at 50 kV and 200 μA. The beam was channelled towards the body of each kendi with a spot size of 20 mm.

The art historical approach of ceramic artefacts were based on a quantitative analysis of attributes based on its aesthetics. Material characterization described the fundamental properties of the material.The art historical approaches with different scientific material characterization techniques were carried out to determine the provenance of the ceramic artefacts. Thus, the main aim was to explore the possibility of supporting the historical approach with data from modern material characterization techniques.

3. Results and Discussion

The origin of the kendi can be predicted by reconstructing through understanding its development in art history. Panofsky's approach of combining the meaning of images with Cassirer's philosophy and Warburg's cultural history is applied in this study (Elsner and Lorenz, 2012).

3.1 Panofsky's Approach

The MoAA catalogue of the kendi collection published by the Oxford University Press in 1991 was used in this analysis (Khoo and Rooney, 1991). Additionally, other historical facts about the kendi based on the published catalogues from various museums and auction websites were also referred to as reliable resources in this study (Cornell University, 2020; Metropress Ltd., 2016). The Herbert F. Johnson Museum of Art, Cornell University, identified a vessel like Kendi I in their catalogues (Christie Manson & Woods Ltd, 2016). Based on the catalogues from these two auction websites, namely, LiveAuctioneers (LiveAuctioneers, 2015), and Metropress Ltd, (t/a Auction Technology Group) (Metropress Ltd, 2016), Kendi II may possibly originate from China or Japan. However, the 1991 MoAA's kendi catalogue identified Kendi II as a Japanese ware. The vessels in Fig 1 have ruyi lappets on the shoulders and flowers with tendrils on the main body. The MoAA kendi, i.e., Kendi I, does not have any decoration on the foot other than a thin line and a different opening mouth shape. The blue glaze section has crazy glazing with grey weathered spots in the dark and light blue areas and the white glaze section had crazed glazing in a vivid bluish-white tint.

In Fig 2, Kendi II had a round dry foot ring, a globular body, a tall tubular neck, mammiform spouts, and a glazed base. It also had a ribbed design on the body and spout, and an embossed ring at the point where the neck and body meet. The analysed shape and design are similar to Chinese kendi (University 2020; Metropress Ltd, 2016).

Based on art-historical facts, the shape and decorations of ancient China porcelain was full of auspicious symbols. The visual characteristics of Kendi I was closely related to ancient Chinese porcelain in the shape of a chicken (Welch, 2013). During the Ming dynasty between 1368 – 1644, the chicken was attributed to have five merits, namely. literacy, martial, bravery, benevolence, and honesty (Cui, 2017). The rise of chicken motifs on porcelain during the Chenghua Emperor was due to his desire for peace, harmony, and family. Kendi I was evidence of the antiquarian tradition in the 15th century of the Chinese dynasty (Miller and Louis, 2012). The symbol of ruyi on Kendi I was related to the Daoist symbols of longevity and a wish for a peaceful life (Jenjarassakul et al., 2000). Meanwhile, plants and flowers symbolize a maxim, moral attribute, or personification through their tendrils, buds, and flowers (Welch, 2013). Porcelain from Jingdezhen in Jiangxi Province had become a major part of Chinese culture by the late 17th century, with white and cobalt blue underglaze designs (Witkowski, 2016). Blue-and-white porcelain was widely sold to Western nations during the Ming dynasties, and later successive Qing dynasties (of around the year 1632 – 1912), making it an iconic Chinese ceramic (Wen et al., 2019).

The art-historical fact based on the catalogues published by auction websites Strausso&Co (Strausso&Co, 2019) and Ashmolean Museum, University of Oxford (Ashmolean Museum, 2013) indicates that Kendi II was highly likely a celadon kendi made in Japan. Arita ware was the main celadon manufacturing centre in Japan in the mid-17th century that produced Chinese-style celadon and blue-and-white porcelain for the Southeast Asian export trade (Lim, 2011). The Japanese wares were exported via Dutch and Chinese trading ships (Cullen, 2017). In fact, when it came to exports to the Southeast Asian market, Japanese production started in earnest at the end of the Ming dynasty to replace what was no longer available from China (Ford and Impey, 1989).

This was due to the impact of maritime bans on trading ceramics during the Ming and Qing dynasties (Tai et al., 2020). Based on the similarity in colour and shape, Kendi II could have originated from China (Metropress Ltd, 2016; Welch 2013). The kendi's solid, light-greenish body is typical of Longquan celadon ware, which China classifies as a form of porcelain (Prinsloo et al., 2005). Thus, it was possible that Kendi I and Kendi II both originated from China, but further investigation using the scientific method was still required to determine their origin. Further investigation based on material characterization was presented next.

3.2 Modern Analytical Characterization

Based on Panofsky's Approach, Kendi I and Kendi II were highly probable to be from China. However, the scientific evidence may support the kendi's uniqueness by qualitatively detecting materials that was present in the body as well as the glaze on its surface. The information was compared with the data obtained from other reported literature to predict the originality of the kendi.

3.2.1 Raman Spectroscopy Analysis of Bodies of Kendis

Raman Spectroscopy generated a spectrum of components in the material as shown in Fig 3. Fig 3 (a) and (b) are the spectrums taken at the bottom rim of both spouted vases. The bottom spot is the best location to represent the body of the kendi since all other parts are covered with glaze.

Fig 3(a) displayed a spectrum representing Kendi I. The figure shown that it was silica-rich with α-quartz peak at 462 cm^{-1}. That was consistent with the documented ingredients of raw materials used in South Chinese high-fired ceramics (Prinsloo et al., 2005). Meanwhile, calcite was found at 159 cm^{-1}, and it was also reported to be present in old ceramics (Lahlil et al. 2009). Oxide mineral of rutile was found at 609 cm^{-1} (Ricci et al., 2016). Its presence leads to the lack of any purification of the raw materials such as clay, kaolin and sand during the fabrication of the ancient Asian porcelain (Simsek Franci et al., 2020). Its presence also suggests that it was probably fired at a higher temperature during the Yuan or early Ming period (Prinsloo et al., 2005). In Fig 3 the Raman spectrum also showed a small peak at 685 cm^{-1} indicating Hematite (Simsek Franci et al., 2020). In addition to hematite, illite, anatase, polycrystalline mullite, and amorphous carbon were observed at 772 cm^{-1}, 198 cm^{-1}, 776 cm^{-1}, 306 cm^{-1} as well as 1107 cm^{-1}, and 1481 cm^{-1}, respectively (Prinsloo et al., 2005; Shoval et al., 2011). The presence of a large peak of polycrystalline mullite itself was a phase of well-fired porcelain (Prinsloo et al., 2005). The presence of all these elements confirms that Kendi I was an ancient Chinese ceramic.

Fig 3(b) showed a spectrum representing element presence in Kendi II. Quartz peaks were observed at 185 cm^{-1} (Widjaja et al., 2011), 456 cm^{-1} (Prinsloo et al., 2005; Shoval et al. 2011), and 1087 cm^{-1} (Bahçeli et al., 2016). Meanwhile, α-quartz covered a broad band at 458 cm^{-1} which was typical of glassy silica (Prinsloo et al., 2005).

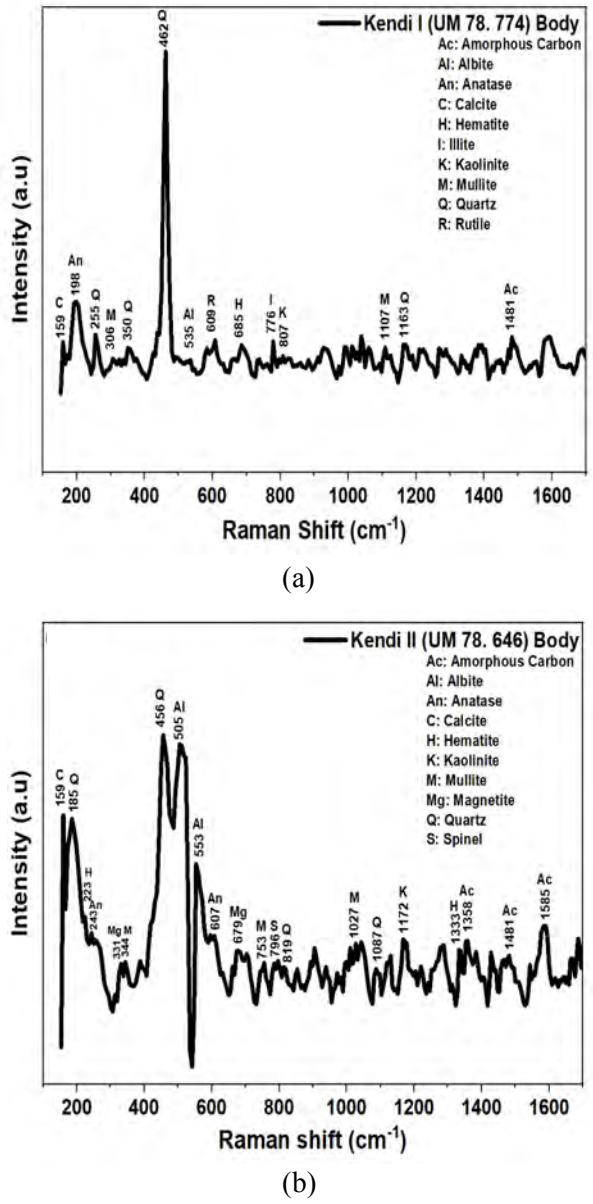

Figure 3. Raman pattern of kendi bodies **(a)** Kendi I **(b)** Kendi II

A peak of 159 cm^{-1} was identified as calcite (Bahçeli et al., 2016; Wen et al., 2019; Kock and De Waal, 2007). The presence of calcite and quartz in ceramics had a significant historical role in understanding the evolution of ancient Chinese ceramics (Wen et al., 2019). Additionally, hematite and magnetite appeared at 223 cm^{-1} (Ricci et al., 2016; Bahçeli et al., 2016), 1333 cm^{-1} (Bahçeli et al., 2016), and 331 cm^{-1} (Simsek Franci et al., 2020), 679 cm^{-1} (Bahçeli et al., 2016), respectively. Magnetite had a high atomic number and its presence beneath the burnished surface was caused the body to appear bright (Ionescu and Hoeck, 2020). The observation of such brightness could be observed in Kendi II. Among the peaks in this spectrum, albite was found at 505 cm^{-1} and 553 cm^{-1} peaks. A combination of quartz and albite indicated that these elements were utilized as the porcelain stone at the main manufacturing site in Jingdezhen as reported by Dias et al. (2013). The rest of the peaks were listed as: 243 cm^{-1} and 607 cm^{-1} which included anatase (Kock and De Waal, 2007); mullite: 344 cm^{-1}, 753 cm^{-1}, and 1027 cm^{-1} (Shoval et al., 2011), amorphous carbon: 1358 cm^{-1} (Kock and De Waal, 2007), and 1481 cm^{-1} (Bahçeli et al., 2016), and spinel: 796 cm^{-1} (Simsek Franci et al., 2020). The presence of amorphous carbon in ancient Chinese ceramics at 1481 cm^{-1} (Ricci et al., 2016; Ionescu and Hoeck, 2020) was reported to had firing temperature of 800-850 °C. The collection of these elemental compositions was consistent with the literature. Therefore, it was with cautious, evidence-linked that Kendi II originated from ancient China.

3.32 Raman Spectroscopy Analysis of Glazes of Kendis

Fig 4 (a) showed elements of glazes based on Raman spectroscopy. The primary peaks of quartz were located at 350 cm^{-1} (Widjaja et al., 2011) 462 cm^{-1} (Bahçeli et al., 2016; Prinsloo et al., 2005; Kock and De Waal, 2007) accordingly. Besides, calcite was displayed at 154 cm^{-1} and 274 cm^{-1} (Wen et al., 2019). The peaks at 492 cm^{-1} (Bahçeli et al., 2016) and 601 cm^{-1} (Kock and De Waal, 2007) indicated the presence of hematite (α-Fe_2O_3) (Simsek Franci et al., 2020) to indicate that Kendi I originated from the Ming dynasty (Kock and De Waal, 2007). Anatase was identified at 633 cm-1 (Prinsloo et al., 2005). The peaks among others were as follows: Brookite with the polymorphs of TiO_2: 320 cm^{-1} (Prinsloo et al., 2005); Mullite: 960 cm^{-1} (Simsek Franci et al., 2020) and 1108 cm^{-1} (Prinsloo et al., 2005); spinel-type phase at a temperature of 1000 °C: 796 cm^{-1} (Simsek Franci et al., 2020); Amorphous Carbon:1585 cm^{-1} (Kock and De Waal, 2007), and cobalt blue: 198 cm^{-1}. Carbon and cobalt blue pigments were mixed in Ming ceramics, resulting in a more intense blue colour (Kock and De Waal, 2007). Cobalt blue was used as a pigment in Chinese porcelain during the Ming Dynasty (Widjaja et al., 2011; Ricci et al., 2016, Germinario et al., 2024). Based on these relevant references and arguments, it was confirmed that Kendi I originated from the Ming Dynasty, China which existed between 1368 to 1644.

Crystalline phases in Kendi II was also displayed in Fig 4 (b). Primary peaks of quartz with glassy alumina silicate were discovered at 450 cm^{-1} and 810 cm^{-1} (Prinsloo et al., 2005). Hematite was also observed at locations 356 cm^{-1}, 730 cm^{-1} (Simsek Franci et al., 2020), and 607 cm^{-1} (Bahçeli et al., 2016). The peak at 191 cm^{-1} was exhibited by the anatase phase of TiO_2. Most Chinese ceramics contained TiO_2 (0.2–2.0%) as a raw material. When it was fired in reducing atmospheric pressure, the relative ratio of TiO_2 to iron oxides influences the shade of green colour in celadon glazes (Prinsloo et al., 2005). Other peaks that could be highlighted are brookite: 249 cm^{-1} (Prinsloo et al. 2005); mullite: 765 cm^{-1} (Simsek Franci et al., 2020); amorphous carbon: 1000 cm^{-1}, and spinel (Fe_2TiO_4): 675 cm^{-1} (Simsek Franci et al., 2020).

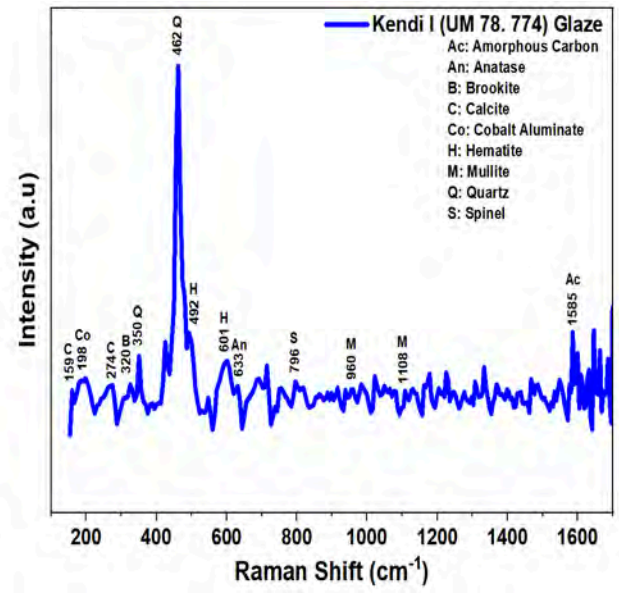

(a)

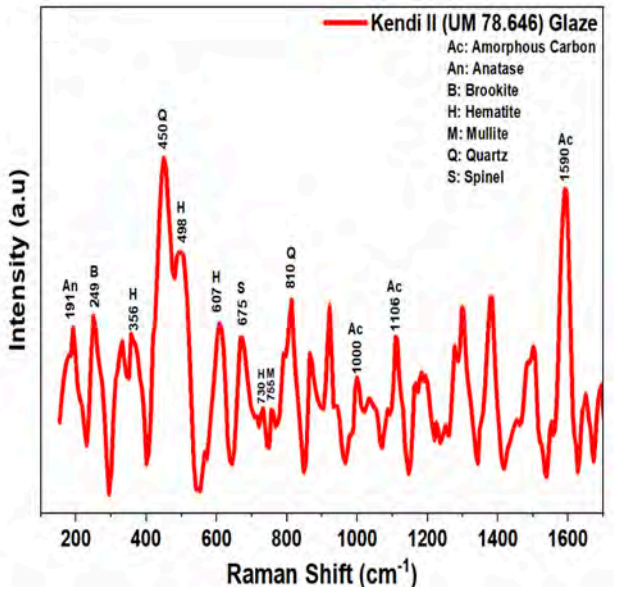

(b)

Figure 4. Raman pattern of kendi glaze for **(a)** Kendi I **(b)** Kendi II

The presence of amorphous carbon was related to carbonaceous which had been reported in pottery glazes for Ming porcelain (Prinsloo et al., 2005). Furthermore, spinel (Fe TiO) was said to had been highly fired at a temperature of more than 1000 °C when used in soft porcelain in 18th century (Simsek Franci et al., 2020). Based on the consistency of the materials found in the literature, Kendi II was hypothesized to have originated from the Ming dynasty in China.

3.2.3 XRF Analysis of Kendi I (Body and Glaze)

Blue-and-white porcelain was one of the most well-known porcelains, which was exported to Western nations during the Ming and Qing dynasties (Wen et al., 2019). The Jingdezhen underglaze blue porcelains were mainly composed of silica-alumina (i.e., SiO2-Al2O3) with the addition of flux agents in which primary components consisted of iron, manganese, cobalt, and nickel (Tite et al., 2012). The porcelain was said to be in abundance in quartz, with a high SiO2/Al2O3 weight percent ratio in the range of 4:1 to 5:1, according to Table 1 (Prinsloo et al., 2005). The main body had contents of low Al2O3, high SiO2, and high K2O concentrations in the range of 19.12% - 21.25%, 71.88% - 74.26%, and 3.61% 3.74% respectively. Other minor metal oxides can also be found as shown in Table 1. Table 1 also tabulated a list of weight percentages of metal oxides in the body of Kendi I as well as its glaze based on the dynasties. Among the familiar dynasties were Song (960-1279), followed by Yuan (1260 – 1368) and Ming (1368 -1644). Table 1 showed that Kendi I had a lower percentage of mullite. Alumina (Al2O3) as a composite in Mullite was thought to originate from Southern China, according to Table 1.

Subsequently, the presence of other metal oxides in Kendi I indicate that it had many similarities with the blue-white porcelain from Yuan or Ming dynasty of Jingdezhen Royal Kiln, South China (Wu et al., 2020). To ascertain these ambiguities, Jinxiu Wen defined a function (F) based on the porcelain compositions to distinguish porcelains from the Yuan, Ming, and Qing dynasties. If F (K2O, CaO, Al2O3) is less than 85.1, it indicated that the dynasty could be either Yuan or Ming. Whereas, if F (K2O, CaO, Al2O3) was greater than 85.1, the Qing dynasty can be proposed (Wen et al., 2019).

$$F(K_2O, CaO, Al_2O_3) = 5.37K_2O + 4.1CaO + 2.81Al_2O_3 \quad (1)$$

Calculations showed that percentage of porcelain in Kendi I was 73.39 which was less than 85.1. Therefore, it was suggested that Kendi I originated from the Ming dynasty located in Jingdezhen, South China.

During Ancient China calcium-rich porcelain glazes were used for centuries, but after the Southern Song Dynasties, potassium-rich glazes replaced them (Simsek et al. 2015). The Mn-rich asbolite ores in the folk kilns of Jingdezhen throughout the Ming dynasties had MnO/CoO ratios ranging from 5.3 to 11.8 (Wen et al., 2019; Fischer and Hsieh, 2017; Simsek Franci, 2020) and similarly for Fe2O3/CoO the range was within 0.4 to 3.7 (Fischer and Hsieh, 2017; Simsek Franci, 2020). For Kendi I the ratio of MnO/CoO of blue-white underglaze porcelain was 9.84 and 2.68 for Fe2O3/CoO. These ratios were like that used in Jingdezhen folk kilns during the Ming dynasty.

Meanwhile, the chemical composition of the glaze can be used to estimate the age of Jingdezhen porcelains manufactured in any dynasty. The formulae of Si (Wen et al. 2019), in which S1, S2 and S3 denote Yuan, Ming and Qing dynasties, respectively, were manipulated in this determination.

Table 1. Chemical Composition of Porcelain Ceramic Bodies and Glazes wt (%) of Kendi I

Location	Dynasty	SiO_2	Al_2O_3	K_2O	CaO	TiO_2	MnO	Fe_2O_3	CoO	Na_2O	MgO	Reference
Body	SC	75.77	17.62	3.37	0.70	0.02	--	1.1	--	<1	0.30	(Tite et al., 2012)
	NS	64.05	28.96	1.8	1.72	0.86	0.05	0.84	--	0.54	1.18	(Tite et al., 2012)
	SS	78.62	15.89	2.80	0.70	0.05	--	0.60	--	0.80	0.20	(Tite et al., 2012)
	Yuan	72.39	20.52	3.40	0.13	0.05	--	1.23	--	1.90	0.16	(Tite et al., 2012)
	Ming	74.04	19.58	3.44	0.61	0.05	--	0.96	--	1.29	0.21	(Simsek et al.,2015)
	Kendi I	75.40	17.83	3.65	0.90	0.04	--	1.44	--	--	--	
Glaze	Kendi I	70.26	6.04	7.79	4.38	0.05	8.17	2.23	0.83	--	--	

*SC: Southern China, NS: Northern Song, SS: Southern Song

$$S_1=22.15K_2O + 6.02CaO + 25.79Na_2O + 10.83MnO - 100.35 \quad (2)$$

$$S_2=25.06K_2O + 5.99CaO + 24.42Na_2O + 13.37MnO - 105.86 \quad (3)$$

$$S_3 =19.47K_2O + 5.03CaO + 18.72Na_2O + 9.99MnO - 67.42 \quad (4)$$

The calculated Si (i=1,2,3) value of Kendi I were 74.39, 100.23, and 89.79 with respect to Yuan, Ming, and Qing Dynasties. The maximum value of Si is found to match S2. Therefore, this proved that the blue-and-white porcelain Kendi I originated from the Ming dynasty from the kiln located in Jingdezhen.

3.2.4 XRF Analysis of Celadon Porcelain Kendi II (Body and Glaze)

It had been reported that the porcelain celadon ceramic kendis of Southern dynasty had relatively high silicon but low iron and aluminium contents. Whereas, celadon from the Northern part showed the contradictory. At the same time, content of specific oxides varied from one dynasty to another (Sang et al., 2019). It had also been reported that celadon bodies from Jingdezhen contained more CaO and raw materials used in Jingdezhen kilns had a significant content of albite. The body composition of celadon ceramics was tabulated in Table 2. It showed that the body is enriched with a combination of Al2O3 and SiO2, with relatively large amounts of flux oxide K2O.

Table 2. Chemical Composition Analysis of Kendi II Compared to Celadon Bodies and Glazes wt (%)

Location	Dynasty	SiO_2	Al_2O_3	TiO_2	Fe_2O_3	CaO	MgO	K_2O	Na_2O	MnO	Reference
	TD	69.39	20.94	0.22	1.69	0.51	0.59	5.13	0.31		(Sang et al., 2019)
	FD	62.93	28.38	1.13	2.5	0.92	1.06	1.75	0.21		(Sang et al., 2019)
	Song	67.03	25.33	0.77	2.06	0.38	0.83	2.28	0.29		(Sang et al., 2019)
	NS	68.99	21.71	0.14	1.86	0.16	0.33	5.51	0.30		(He et al., 2016)
Body	SS	67.85	22.62	0.15	2.28	0.23	0.36	5.16	0.35		(He et al., 2016)
	Jin	70.67	21.36	0.67	1.98	0.41	1.03	2.46	0.39		(Sang et al., 2019)
	Yuan	67.06	23.55	0.67	2.23	0.16	0.36	5.13	0.37		(He et al., 2016)
	Ming	72.40	19.62	0.08	1.28	0.51	0.39	4.20	0.52		(He et al., 2016)
	Kendi II	77.27	14.41	0.10	1.53	2.11	---	4.67	--		
	TD	62.5	11.43	0.18	2.04	15.81	1.62	2.7	--	0.7	(Wu et al., 2015)
	FD	59.4	16.0	0.4	1.8	16.0	2.0	3.4	0.3	0.6	(Prinsloo et al., 2005)
	NS	63.2	16.8	0.2	1.4	13.0	1.1	3.3	0.6	0.4	(Prinsloo et al., 2005)
	SS	68.6	14.3	0.02	0.7	10.4	0.4	5.0	0.1	--	(Prinsloo et al., 2005)
Glaze	Yuan	67.4	16.7	0.2	1.5	6.8	0.6	5.5	1.1	0.4	(Prinsloo et al., 2005)
	Ming	67.6	15.0	0.3	1.4	6.3	1.7	6.5	1.1	--	(Prinsloo et al., 2005)
	LS 1	67.1	15.7	0.2	2.63	4.37	1.22	6.53	0.82	0.22	(Prinsloo et al., 2005)
	LS 2	68.19	15.72	0.13	2.03	4.48	0.52	6.98	0.99	0.19	(Prinsloo et al., 2005)
	Kendi II	68.1	9.00	0.16	3.41	5.02	0.98	10.16	--	0.21	

*TD: Tang Dynasty, FD: Five Dynasty, NS: Northern Song, SS: Southern Song, LS: Literature Sample

The mineral albite was found in the body of Kendi II as observed in the Raman spectroscopy is comparable to the principal raw material of potassium feldspar (He et al., 2016). The body had a relatively low amount of Al2O3 (14.41%) with a high amount of SiO2 (77.27%). Apart from these two minerals, Kendi II also possessed a low amount of Fe2O3 and TiO2 but a higher amount of K2O minerals. These facts match well with the celadon kendis that were found in Jingdezhen, Southern China (Franklin and Boak, 2019; Tite et al., 2012). Low Al2O3, Fe2O3, TiO2 but high SiO2 and K2O indicated that the celadon Kendi II may have originated from Jingdezhen, Southern China during the Ming dynasty (Franklin and Boak, 2019; Tite et al., 2012).

The glaze used to decorate the ceramics basically depends on CaO, Fe2O3, MgO, K2O, and MnO mineral contents. As an example, the density of a green glaze is determined by the iron oxide content which was affected by the fire's redox atmos, ıere (Sang et al., 2019). The analysis by Li shows that Chinese Celadon wares had high concentrations of K2O, CaO, TiO2, Fe2O3, CoO, and MnO. These metal oxides work best as ceramic colours (Li et al., 2012). The main difference between these dynasties was the ratio of CaO to K2O. Fig 5 was plotted to visualize the spread of the ratio based on the different dynasties (Tite et al., 2012). The results include the ratio embedded in Kendi II. It was observed that the ratio gradually decreases as the different dynasties progress. Worth to note that results of the LS 1 and LS 2 were originated from the Ming dynasty. Since the ratio executed from Kendi II had a ratio of 0.5, which is nearest to the Ming dynasty, it is that Kendi II originated in the Ming dynasty. This prediction indirectly refutes the vague claim that Kendi II is Japanese ceramic porcelain as reported by Jee et al. (Khoo and Rooney, 1991).

4. Conclusion

In this study, two kendis named as Kendi I and Kendi II, were investigated to predict their originalities in terms of provenance. This may lead to also determining the dynasty and respective period they came from. The combination of two methods used such as art historical and material characterization techniques to analyse the kendis. For art historical method, the Panofsky Approach was applied for analysing aesthetic views like attributions and motifs. Further confirmation proceeded to determine the composition of materials in body and glaze of the kendis with the help of a handheld XRF and Raman spectroscopy. It is predicted with strong evidence that Kendi I originated from Jingdezhen during the Ming Dynasty (1368-1644 CE), China. Although Kendi II was reported earlier as a Japanese ceramic celadon, this study could safely predict that it originated from China during the Ming Dynasty (1368-1644 CE). The synergy contributed from both methods has enriched the knowledge and technique in predicting the provenance of these two ceramic kendis.

Data Availability

All data produced in this study are available under request.

Funding Information and Acknowledgment

This study is fully funded by the Impact-Oriented Interdisciplinary Research Grant Programme (IIRG), Universiti Malaya Grant Number (IIRG034B-2019) and partially supported by IIRG008C-19SAH. The authors would like to express their gratitude to Mr. Aziz Abdul Rashid, Former Head and Curator of the Museum of Asian Art at Universiti Malaya (MoAA) for providing insightful thought, and fruitful discussions about the Kendi.

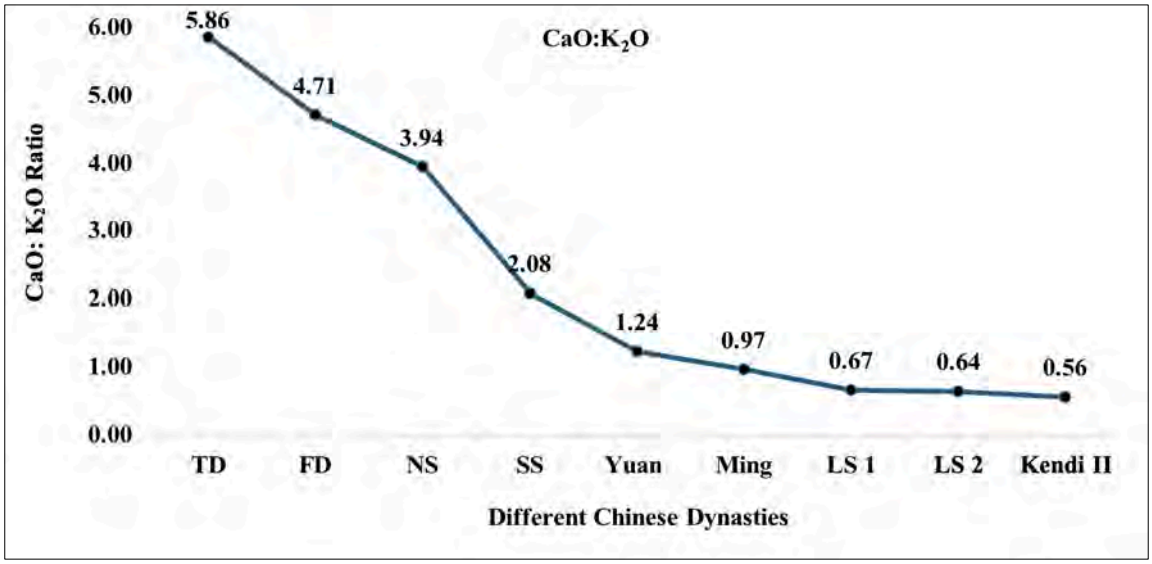

Figure 5. Comparison of $CaO:K_2O$ in different dynasties of celadon glaze.

Conflict of Interest

The authors declare that they have no conflicts of interest.

Declaration

The authors declare that they have no known financial interests or personal relationships that could have influenced the work reported in this paper.

References

Abdullah, A. H., Ibrahim, Y., & Khalid, R. I. R. (2020). An iconographical analysis based on the Erwin Panofsky theory on the Malayness in the paintings of Amron Omar and Haron Mokhtar. International Journal of Academic Research in Business and Social Sciences, 10(9). https://doi.org/10.6007/ijarbss/v10-i9/7835

Ashmolean Museum, University of Oxford. (2013). Beginnings of the European export trade. http://jameelcentre.ashmolean.org/collection/4/1238/128 1

Bahçeli, S., Güleç, G., Erdoğan, H., & Söğüt, B. (2016). Micro-Raman and FT-IR spectroscopic studies of ceramic shards excavated from ancient Stratonikeia city at Eskihisar village in West-South Turkey. Journal of Molecular Structure, 1106, 316–321. https://doi.org/10.1016/jmolstruc.2015.10.036

Botticelli, M., Mignardi, S., de Vito, C., Liao, Y. W., Montanari, D., Shakarna, M., … Medeghini, L. (2020). Variability in pottery production at Khalet al-Jam'a necropolis, Bethlehem (West Bank): From the Early-Middle Bronze to the Iron Age. Ceramics International, 46(10), 16405–16415. https://doi.org/10.1016/j.ceramint.2020.03.200

Bronitsky, G. (1986). The use of materials science techniques in the study of pottery construction and use. Advances in Archaeological Method and Theory, 9, 209–276. https://doi.org/10.1016/b978-0-12-003109-2.50008-8

Christie Manson & Woods Ltd. (2016). An Arita celadon kendi (pouring vessel), Edo period (late 17th century). https://onlineonly.christies.com/s/japanese-art-its-influence-european-court/arita-celadon-kendi-

Cort, L. A. (2017). Container jars from the Maenam Noi kilns, Thailand: Use and reuse along maritime trade routes in Asia. *Bulletin de l'École Française d'Extrême-Orient, 103*(1), 267–296. https://doi.org/10.3406/befeo.2017.6252

Cornell University. (2020). Chicken-shaped ewer. Herbert F. Johnson Museum of Art, Ithaca, New York.

Cui, Y. (2017). *Speaking for the chicken cup: A case study in Chinese art collecting* (Doctoral dissertation, The Australian National University).

Cullen, L. (2017). The Nagasaki trade of the Tokugawa era: Archives, statistics, and management. *Japan Review, 31*, 69–104. https://www.jstor.org/stable/44427700

Dias, M. I., Prudêncio, M. I., Pinto De Matos, M. A., & Rodrigues, A. L. (2013). Tracing the origin of blue and white Chinese porcelain ordered for the Portuguese market during the Ming dynasty using INAA. *Journal of Archaeological Science, 40*(7), 3046–3057. https://doi.org/10.1016/j.jas.2013.03.007

Elsner, J., & Lorenz, K. (2012). The genesis of iconology. *Critical Inquiry, 38*(3), 483–512. https://doi.org/10.1086/664548

Fischer, C., & Hsieh, E. (2017). Export Chinese blue-and-white porcelain: Compositional analysis and sourcing using non-invasive portable XRF and reflectance spectroscopy. *Journal of Archaeological Science, 80*, 14–26. https://doi.org/10.1016/j.jas.2017.01.016

Ford, B. B., & Impey, O. R. (1989). *Japanese art from the Gerry Collection in the Metropolitan Museum of Art*. Metropolitan Museum of Art.

Franklin, K., & Boak, E. (2019). The road from above: Remotely sensed discovery of early modern travel infrastructure in Afghanistan. *Archaeological Research in Asia, 18*, 40–54. https://doi.org/10.1016/j.ara.2019.02.002

Freitas, R. P., Coelho, F. A., Felix, V. S., Pereira, M. O., de Souza, M. A. T., & Anjos, M. J. (2018). Analysis of 19th century ceramic fragments excavated from Pirenópolis (Goiás, Brazil) using FT-IR, Raman, XRF and SEM. *Spectrochimica Acta Part A: Molecular and Biomolecular Spectroscopy, 193*, 432–439. https://doi.org/10.1016/j.saa.2017.12.047

Germinario, C., Cultrone, G., De Bonis, A., Izzo, F., Langella, A., Mercurio, M., Nodari, L., Vyhnal, C. R., & Grifa, C. (2024). μ-Raman spectroscopy as a useful tool for improving knowledge of ancient ceramic manufacturing technologies. *Applied Clay Science.* https://doi.org/10.1016/j.clay.2024.107347

Gliozzo, E. (2020). Ceramic technology: How to reconstruct the firing process. *Archaeological and Anthropological Sciences, 12*(11). https://doi.org/10.1007/s12520-020-01133-y

He, Z., Zhang, M., & Zhang, H. (2016). Data-driven research on chemical features of Jingdezhen and Longquan celadon by energy dispersive X-ray fluorescence. *Ceramics International, 42*(4), 5123–5129. https://doi.org/10.1016/j.ceramint.2015.12.030

Ionescu, C., & Hoeck, V. (2020). Ceramic technology: How to investigate surface finishing. *Archaeological and Anthropological Sciences, 12*(9). https://doi.org/10.1007/s12520-020-01144-9

Jenjarassakul, W., Chinalai, V., & Chinalai, L. J. (2000).*Yao Lin Tan Shaman's Robes* (pp. 94–99). London.

Khoo, J. E., & Rooney, D. (1991). *Kendi: Pouring vessels in the University of Malaya collection*. Oxford University Press

Kock, L. D., & De Waal, D. (2007). Raman studies of the underglaze blue pigment on ceramic artefacts of the Ming dynasty and of unknown origins. *Journal of Raman Spectroscopy, 38*(11), 1480–1487. https://doi.org/10.1002/jrs.1805

Prinsloo, L. C., Wood, N., Loubser, M., Verryn, S. M. C., & Tiley, S. (2005). Re-dating of Chinese celadon shards excavated on Mapungubwe Hill, a 13th century Iron Age site in South Africa, using Raman spectroscopy, XRF and XRD. *Journal of Raman Spectroscopy, 36*(8), 806–816. https://doi.org/10.1002/jrs.1367

Li, L., Feng, S. L., Feng, X. Q., Xu, Q., Yan, L. T., Ma, B., & Liu, L. (2012). Study on elemental features of Longquan celadon at Fengdongyan kiln site in Yuan and Ming dynasties by EDXRF. *Nuclear Instruments and Methods in Physics Research Section B: Beam Interactions with Materials and Atoms, 292*, 25–29. https://doi.org/10.1016/j.nimb.2012.09.034

Lim, T. (2011). Re-centering trade periphery through fired clay: A historiography of the global mapping of Japanese trade ceramics in the premodern global trading space. *Sino-Japanese Studies, 18*.

Liu, S., Wu, H., & Zhao, X. (2023). Non-destructive provenance analysis of 15th–17th century export porcelains to Europe using portable XRF and Raman spectroscopy. *Journal of Archaeological Science: Reports*, 55, 103925. https://doi.org/10.1016/j.jasrep.2023.10392

LiveAuctioneers. (2015). 17th c. Ming dynasty celadon kendi [Auction listing]. https://www.liveauctioneers.com/item/34896239_17th-c-ming-dynasty-celadon-kendi-17th-c-ming-dynasty

Maritan, L. (2020). Ceramic abandonment: How to recognise post-depositional transformations.*Archaeological and Anthropological Sciences, 12*(8). https://doi.org/10.1007/s12520-020-01141-y

Metropress Ltd (t/a Auction Technology Group). (2016). A good 17th/18th century Chinese celadon-glazed porcelain kendi, with ribbed sides and spout [Auction listing]. https://www.the-saleroom.com/en-gb/auction-catalogues/john-nicholson/catalogue-id-srjo10119/lot-dea18a26-3e98-49bb-98a8-a66c00c37f33

Miller, P. N., & Louis, F. (2012). *Antiquarianism and intellectual life in Europe and China, 1500–1800*.University of Michigan Press.

Montana, G. (2020). Ceramic raw materials: How to recognize them and locate the supply basins—Mineralogy, petrography. *Archaeological and Anthropological Sciences, 12*(8). https://doi.org/10.1007/s12520-020-01130-1

Pollard, A. M., & Hatcher, H. (1994). The chemical analysis of Oriental ceramic body compositions: Part 1: Wares from North China. *Archaeometry, 36*(1), 41–62. https://doi.org/10.1111/j.1475-4754.1994.tb00710.x

Pradell, T., & Molera, J. (2020). Ceramic technology: How to characterise ceramic glazes. *Archaeological and Anthropological Sciences, 12*(8). https://doi.org/10.1007/s12520-020-01136-9

Prinsloo, L. C., Wood, N., Loubser, M., Verryn, S. M. C., & Tiley, S. (2005). Re-dating of Chinese celadon shards excavated on Mapungubwe Hill, a 13th century Iron Age site in South Africa, using Raman spectroscopy, XRF and XRD. *Journal of Raman Spectroscopy, 36*(8), 806–816. https://doi.org/10.1002/jrs.1367

Quinn, P. S. (2018). Scientific preparations of archaeological ceramics: Status, value and long term future. *Journal of Archaeological Science, 91*, 43–51 https://doi.org/10.1016/j.jas.2018.01.001

Ricci, G., Caneve, L., Pedron, D., Holesch, N., & Zendri, E. (2016). A multi-spectroscopic study for the characterization and definition of production techniques of German ceramic sherds. *Microchemical Journal, 126*, 104–112. https://doi.org/10.1016/j.microc.2015.12.009

Sang, Z., Wang, F., Duan, X., Mu, T., Ren, Z., Wei, X.,Jiao, Y. (2019). Analysis of the celadon characteristics of the Yaozhou kiln. *Ceramics International, 45*(17), 22215–22225. https://doi.org/10.1016/j.ceramint.2019.07.245

Shoval, S., Boudeulle, M., & Panczer, G. (2011). Identification of the thermal phases in firing of kaolinite to mullite by using micro-Raman spectroscopy and curve-fitting. *Optical Materials, 34*(2), 404–409. https://doi.org/10.1016/j.optmat.2011.08.031

Simsek, G., Colomban, P., Wong, S., Zhao, B.,Rougeulle, A., & Liem, N. Q. (2015). Toward a fast non-destructive identification of pottery: The sourcing of 14th–16th century Vietnamese and Chinese ceramic shards. *Journal of Cultural Heritage, 16*(2), 159–172. https://doi.org/10.1016/j.culher.2014.03.003

Simsek Franci, G. (2020). Handheld X-ray fluorescence (XRF) versus wavelength dispersive XRF: Characterization of Chinese blue-and-white porcelain sherds using handheld and laboratory-type XRF instruments. *Applied Spectroscopy, 74*(3), 314–322. https://doi.org/10.1177/0003702819890645

Simsek Franci, G., Akkas, T., Yildirim, S., Yilmaz, S., & Birdevrim, A. N. (2020). Characterization of a Jian-like sherd with the optical microscope, confocal Raman, wavelength-dispersive X-ray fluorescence, and portable XRF spectrometers. *Journal of Raman Spectroscopy, 51*(8), 1343–1352. https://doi.org/10.1002/jrs.5904

Strausso & Co. (2019). An Arita celadon kendi. https://www.straussart.co.za/auctions/lot/18-mar-2019/124

Tai, Y. S., Daly, P., McKinnon, E. E., Parnell, A., Feener, R. M., Majewski, J., … Sieh, K. (2020). The impact of Ming and Qing dynasty maritime bans on trade ceramics recovered from coastal settlements in northern Sumatra, Indonesia. *Archaeological Research in Asia, 21*, 100174.https://doi.org/10.1016/j.ara.2019.100174

Tite, M. S., Freestone, I. C., & Wood, N. (2012). An investigation into the relationship between the raw materials used in the production of Chinese porcelain and stoneware bodies and the resulting microstructures. *Archaeometry, 54*(1), 37–55. https://doi.org/10.1111/j.1475-4754.2011.00614.x

Welch, P. B. (2013). *Chinese art: A guide to motifs and visual imagery*. Tuttle Publishing.

Wen, J., Chen, Z., Zeng, Q., Hu, L., Wang, B., Shi, J., Zhang, G. (2019). Multi-micro analytical studies of blue-and-white porcelain (Ming dynasty) excavated from Shuangchuan Island. *Ceramics International, 45*(10), 13362–13368. https://doi.org/10.1016/j.ceramint.2019.04.031

Witkowski, T. H. (2016). Early history and distribution of trade ceramics in Southeast Asia. Journal of Historical Research in Marketing, 8(2), 216–237. https://doi.org/10.1108/JHRM-07-2015-0026

Widjaja, E., Lim, G. H., Lim, Q., Mashadi, A. B., & Garland, M. (2011). Pure component Raman spectral reconstruction from glazed and unglazed Yuan, Ming, and Qing shards: A combined Raman microscopy and BTEM study. *Journal of Raman Spectroscopy, 42*(3), 377–382. https://doi.org/10.1002/jrs.2721

Wu, J., Ma, H., Wood, N., Zhang, M., Qian, W., Wu, J., & Zheng, N. (2020). Early development of Jingdezhen ceramic glazes. *Archaeometry, 62*(3), 550–562. https://doi.org/10.1111/arcm.12539

Wu, J., Zhang, M., Hou, T., Li, Q., & Wu, J. (2015) Analysis of the celadon of the Tang and the Five Dynasties unearthed from Nan Kiln and Lantian Kiln site of Jingdezhen, China. *Ceramics International, 41*(5), 6851–6857. https://doi.org/10.1016/j.ceramint.2015.01.134

Xanthopoulou, V., Iliopoulos, I., & Liritzis, I. (2020). Characterization techniques of clays for the archaeometric study of ancient ceramics: A review *Scientific Culture, 6*(2), 73–86. https://doi.org/10.5281/zenodo.3724849

IJAMMP

Deformation Behaviour in the New Backward Extrusion Process of Pure Copper through Different Die Geometries

Moein Shahveh, Ghader Faraji*

RESEARCH ARTICLE

ARTICLE INFO

Keywords:

New backward extrusion;
Finite Element analysis;
Severe plastic deformation;
Optimization process.

Article History

*Received:*24 October 2025
*Revised:*19 February 2026
*Accepted:*28 February 2026
Published:

ABSTRACT

This study investigated the effects of die geometry on the required forces and strains in the new backward extrusion (NBE) process. The force requirements for copper extrusion were determined using the finite element method, and the relationships between die geometry and process parameters on extrusion force and plastic strain were examined. The process efficiency was evaluated under various working conditions by examining the relationship between geometric variables and speed. This innovative approach, which uses hydrostatic pressure techniques, shows potential to transform billets into ultrafine-grained tubes and materials that are difficult to deform. The results indicate that modifications to the fix-punch geometry significantly reduce the required extrusion force. In all cases, the extrusion force initially increased as the billet entered the deformation zone, then decreased as material continued to flow. Maximum extrusion loads of 109 kN and 91.8 kN were obtained for fix-punch designs with inner channel angles of 30° and 45°, respectively. In comparison, a lower maximum load of 94.2 kN was observed for the geometry with an inner channel radius of 12.5 mm. The FEM results further revealed that the equivalent plastic strain (PEEQ) was strongly dependent on fix-punch geometry, with maximum PEEQ values ranging from approximately 2 to 2.5, primarily concentrated near the die corner and along the radial deformation path. Compared with angled channel designs, the radial geometry resulted in reduced force demand and a more gradual strain distribution during the NBE process.

1. Introduction

In recent years, significant research efforts have been directed toward the development of novel manufacturing processes for high-performance materials in advanced applications (H. Rahimi et. al, 2025). Obtaining fine-grained materials with excellent mechanical characteristics is very important (Mao et. al., 2021). Severe plastic deformation (SPD) techniques have garnered substantial interest as efficient methods for generating bulk ultrafine-grained (UFG) and nanostructured metals and alloys while maintaining overall dimensions (Taherkhani et al., 2025). Materials processed by SPD generally exhibit significantly elevated strength, extended fatigue life, superior formability or superplasticity, and, in many cases, greater wear and corrosion resistance, rendering them highly desirable for industrial applications (Ahmadi, et al. 2021; Faraji, et al., 2018). Tubes are of particular importance, especially among the diverse product geometries for applications in heat exchangers, energy systems, and lightweight structures,which has led to the Development of SPD forming techniques (Lowe & Valiev, 2000; Valiev et al., 2016; Zohrevand et al., 2023).

Department of Mechanical Engineering, College of Engineering, University of Tehran, Tehran, 11155-4563, Iran

*Corresponding author : ghfaraji@ut.ac.ir

Several processes have been proposed for producing thin-walled tubular components with large imposed strains, including Parallel Tubular Channel Angular Pressing (PTCAP) (Awasthi et al, 2022), Tube Backward Extrusion (TBE) (Abu-Farha, 2012), High Pressure Tube Twisting (HPTT) (Toth et al., 2019), Friction Stir Back Extrusion (FSBE) (El Mehtedi et al., 2019), and Tube High Pressure Shearing (t-HPS) (Wang et al., 2012).

However, many reported configurations remain limited by disadvantages such as high forming forces, non-uniform strain distribution, complex tools, and limited scalability for long tubes or closed geometries. Consequently, Optimization of existing processes and development of modified mold concepts, especially for industry-relevant alloys and tubular products, remain active research topics to reduce energy consumption and improve strain homogeneity (Faraji et al. 2011; Jafarlou et al., 2016; Majidabad et al., 2023).

To address some of the limitations of SPD Processes for tube production, severl studies have been conducted. Motallebi et al., (2021) showed that applying hydrostatic force in Hydrostatic Tube Cyclic Expansion Extrusion (HTCEE) significantly improves material flow and reduces the required forming load, while creating a more uniform strain distribution. Bakhshi-Jooybari et al. (2006), focused

on reducing deformation load in BE by optimizing the die profile using numerical simulation and experimental methods. Shatermashhadi et al.,(2014) presented the NBE instead of conventional backward extrusion to reduce the force required for backward extrusion and increase plastic strain by including a fix-punch section. Adding this section results in a decrease of more than 25% in the force required for production compared to the standard backward extrusion process. Manaafi et al., (2016) have presented techniques to enhance the NBE process, including the use of hydrostatic force, resulting in an 11% reduction in the process power requirement.

The NBE produces ultrafine-grained metals characterized by enhanced mechanical strength and optimized microstructural properties. This method is suitable for closed-end products and offers benefits compared to alternative production methods. Some benefits of this method include reduced material usage, increased dimensional accuracy and surface quality, appropriate mechanical and microstructural properties, and reduced additional steps. To reduce the force and energy required in the SPD process, the optimization of this group of forming processes has received much attention. Failure to consider die design parameters when studying metal deformation can result in excessive energy requirements and inaccurate results, despite efforts to achieve the best possible outcome.

FEM is an important approach for understanding the plastic deformation behavior of materials in forming processes (Dixit & Dixit, 2008). Numerical analysis using FEM was performed to evaluate material deformation and predict strain and stress distributions. The plastic deformation behaviour during the BE process is mainly controlled by the die geometry, the material, and the process conditions (Zeng et al., 2024). Despite numerical and experimental investigations on NBE, the specific influence of the internal channel geometry of the fix-punch on the force, strain distribution and strain homogeneity in the NBE process has not been systematically determined. In particular, comparative analyses between angle channels and radius geometries under the same processing conditions are still limited. Therefore, this study investigates the plastic deformation characteristics of commercial pure copper in NBE, as assessed by finite element analysis, variations in extrusion force, and strain progression. Previous research has shown that changing the die geometry can increase the applied equivalent strain and facilitate the development of fine-grained and granular structures. This study systematically analyzes the effects of different die geometries on the effective strain distribution and extrusion force requirements in the NBE process of copper, with the aim of establishing design guidelines to optimize die geometry for energy efficiency, strain uniformity in thin-walled and closed-end products.

2. Methodology

Finite element simulations of the NBE process were performed using Abaqus/Explicit 2021 to investigate the effect of die geometry on deformation behavior, extrusion force, and strain distribution. An axisymmetric model that matched the geometry and mechanical properties of the experimental samples was developed to validate FEM results against experimental data. In the next step, boundary conditions were defined to prevent rigid-body motion of the billet while allowing free material flow within the deformation channel. Reaction forces on the movable punch were recorded to evaluate the evolution of the extrusion load throughout the process. CAX4R elements were used to represent the axisymmetric billet, with mesh sizes ranging from 0.05 to 1.4 mm. Adaptive Lagrangian-Eulerian elements (ALE) were specifically designed and tuned to handle significant deformations and are utilized in simulations. Thus, using ALE techniques improved mesh quality during simulation of SPD processes. The workpiece exhibited a friction coefficient of 0.05 when in contact with the die components. Additionally, a friction coefficient (μ) of 0.05 was considered for the billet's contact with other deformed sections during the process.

During the NBE, the movable punch descended while other die components remained stationary. Fig. 1 shows the starting and ending points of the movable punch during the process, along with the material flow direction in various ways. The punching velocity was set to 10 mm/min. To investigate the effect of die geometry on the NBE process, three fix-punch configurations were analyzed, including inner channel angles of 30° and 45°, and an inner channel radius of 12.5 mm. The selected geometric parameters were chosen to represent sharp, intermediate, and smooth material transfer conditions commonly encountered in extrusion die design. The inner channel angle of 30° was considered to impose higher material flow resistance due to the abrupt change in flow direction, whereas the inner channel angle of 45° provided a smoother material transition with reduced geometric constraint. The use of the inner channel radius of 12.5 mm was intended to minimize stress concentration at the die corner and to promote a more gradual and uniform material flow during the NBE process. Other geometric parameters, including billet dimensions, channel length, and final tube thickness, were kept constant to ensure a consistent comparative analysis. Pure copper was the material utilized in the simulation. Since the die remained elastic and underwent negligible deformation, it was modeled as a rigid body (Uyyuru & Valberg, 2006). Table 1 lists the density, Young's modulus (E), Poisson's ratio (ν), yield strength, and ultimate strength of copper. Fig 2 displays the stress-strain curve for pure annealed copper.

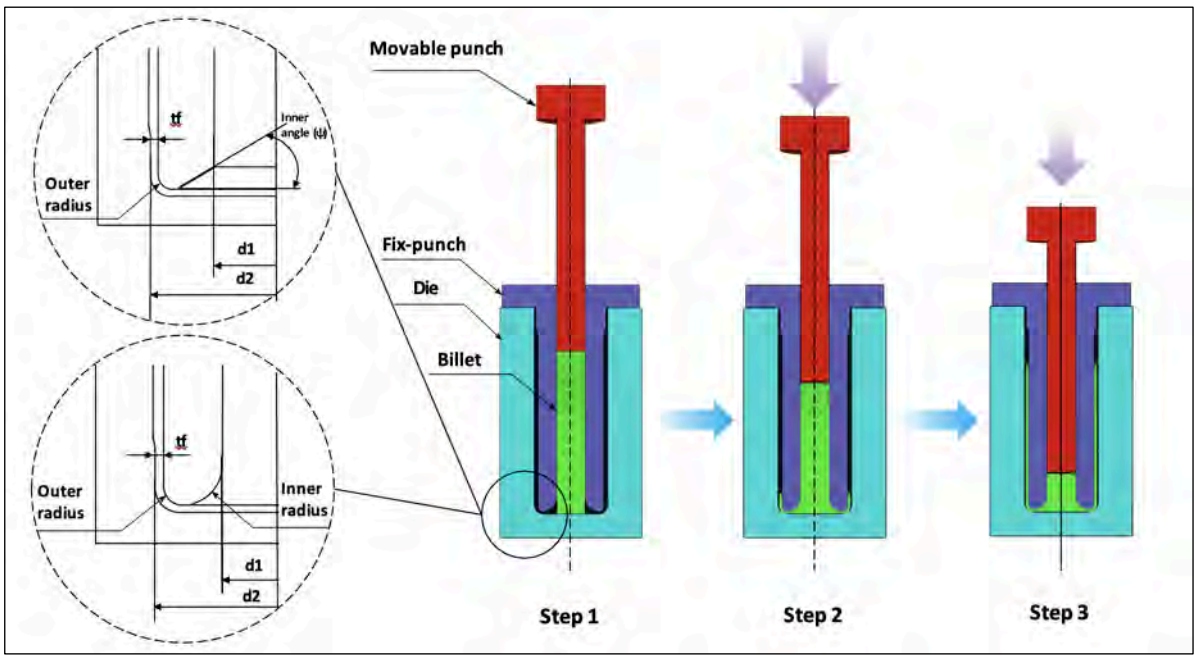

Figure 1. Schematic illustration of the NBE process

Table 1. Mechanical properties of pure copper

Simulation Parameters	Values
Density (kg.m^{-3})	8900
Modulus of Elasticity (GPa)	110
Tensile Strength, Yield (MPa)	33.3
Elongation at Break (%)	60
Poisson's ratio	0.34
Stress-relief annealing temperature (°C)	250-500

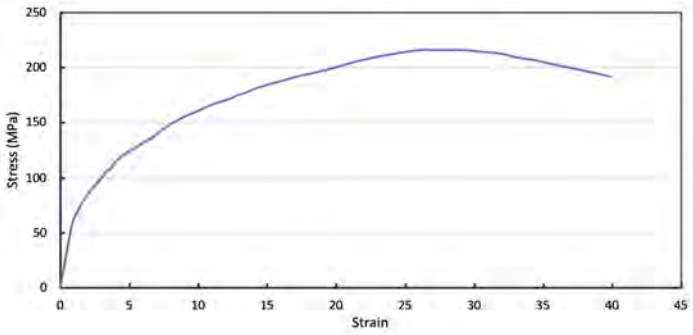

Figure 2. Stress-strain curve of pure copper used in FE modeling

This process involves creating the product from a copper billet that has an initial length of 150 mm and a diameter of 25 mm. Table 1 contains the initial billet parameters. Fig. 1 shows the geometric parameters that have been modified throughout the analysis procedure, with the inner diameters (d1) and outer diameters (d2) and final thickness (tf) remaining constant. FEM simulations were conducted to study deformation patterns and material properties by varying the inner channel angles, the inner channel radius, and the channel shape.

Fixed values are used for additional parameters such as the initial billet diameter, movable punch diameter, and billet height. Initially, the tube is stretched outward through a passage at the inner channel angles of ψ = 45°, 30°, and with the inner channel radius of r1 = 12.5mm, after which the billet thickness is decreased to tf. In the end, the narrow tube with a diameter (d2) inside is flipped through the second channel. Extrusion through angled channels and thickness reduction in the NBE process result in significant deformation of the tube material, producing a thin-walled tube with ultra-fine grain structure. The main factors for analysis are the gap height, channel height, and die shape. Table 2 lists the parameters examined and evaluated in the design. It is important to note that this statement requires experimental evidence.

Table 2. Process parameters and simulation conditions for NBE

Simulation Type	axisymmetric
Die Type	Rigid Body
Billet Type	Deformable
Billet material	Cu
Press speed (mm/min)	10
Billet temperature (°C)	25
Channel length (mm)	180
Channel diameter (mm)	2
Height of billet (mm)	150
Diameter of billet (mm)	25

3. Results and Discussion

FEM simulation results for movable punch load, stress, and applied strains were significant, and the development of Equivalent Plastic Strain (PEEQ) and force at various stages of NBE processing are shown in Figs. 3, 4, and 5.

Fig. 3 shows the movable punch load-displacement behavior for three fix-punch geometries with the inner channel angles of 30° and 45°, and the inner channel radius of 12.5 mm. The maximum movable punch load was evaluated for each geometry. A constant channel height and a friction coefficient of μ=0.05 were maintained throughout the simulations. The load-displacement curves provided valuable insight into the deformation mechanics and force requirements of the manufacturing process. In Zone I, the load increased rapidly as the billet head entered the deformation channel. This stage occurs when the billet head enters the channel. The force difference in this stage was slight. However, the force required in the channel is initially low and increases as material flows through. With the inner channel radius of 12.5 mm, the force remained lower than that of the other geometries at this stage. Zone II represented a transition stage marked by an initial minor load increase, followed by a prominent force surge as the material reached the narrower confined channel section. In the second stage, the load dropped from its peak to a local minimum, followed by a slight increase in Zone III. The cases examined with the inner channel radius of 12.5 mm and the inner channel angle of 45° show that at the onset of Zone III, the billet struck the channel wall. Until the billet was entirely inside the channel, a slight increase in force was observed

A prominent force surge was detected in Zone V for the inner channel angle of 30°, signifying substantial changes in billet shape. Notably, the inner channel angle of 30° requires significantly higher force during this stage than other geometries, leading to less stable material flow and increased load volatility. The peak movable punch load for the inner channel angle of 30° reached approximately 109 kN, and using the inner channel radius of 12.5 mm resulted in approximately an 18% reduction in applied force relative to the inner channel angle of 30°, yielding notable cost and energy savings.

Fig. 4 shows the material flow for each fix-punch geometry at the successive stages of the NBE process. Specifically, Figs. 4(a–d) show the complete deformation geometry and billet configuration for a channel with the inner channel angle of 30°, Figs. 4(e–h) show the corresponding geometry for a channel with an inner angle of 45°, and Figs. 4(i–l) shows the deformation sequence for a channel with the inner channel radius of 12.5 mm. In all three geometries, material continuously fills the channel during all deformation stages. This uninterrupted contact between the material and channel surface is maintained by back pressure, which prevents material separation and ensures continuous deformation. The continuous filling behavior observed across all scenarios underscores the critical role of back pressure in maintaining the integrity of the material flow during extrusion. The deformation patterns observed in all geometries indicate a steady progression of material towards the channel exit. This consistency indicates a steady and uniform flow of material through the channel. Such uniformity is essential to achieve consistent

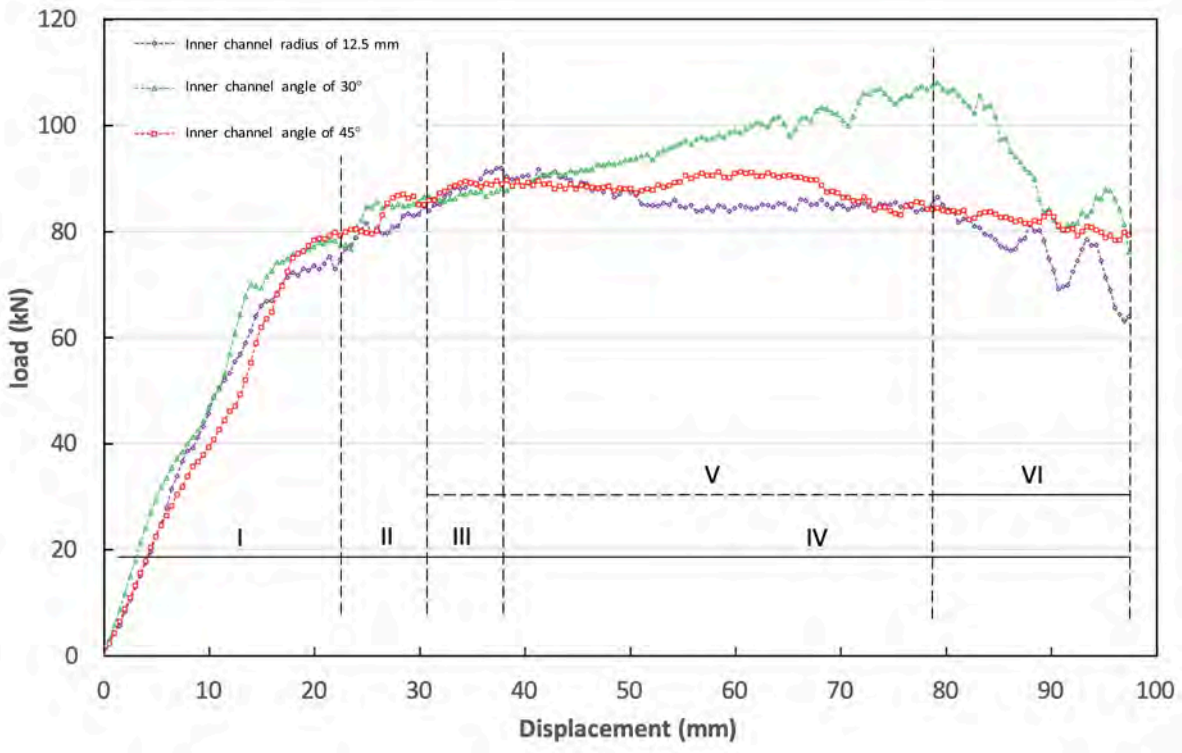

Figure 3. Load-displacement behavior in fix-punch geometries with the inner channel angles of 30°, 45°, and the inner channel radius of 12.5 mm.

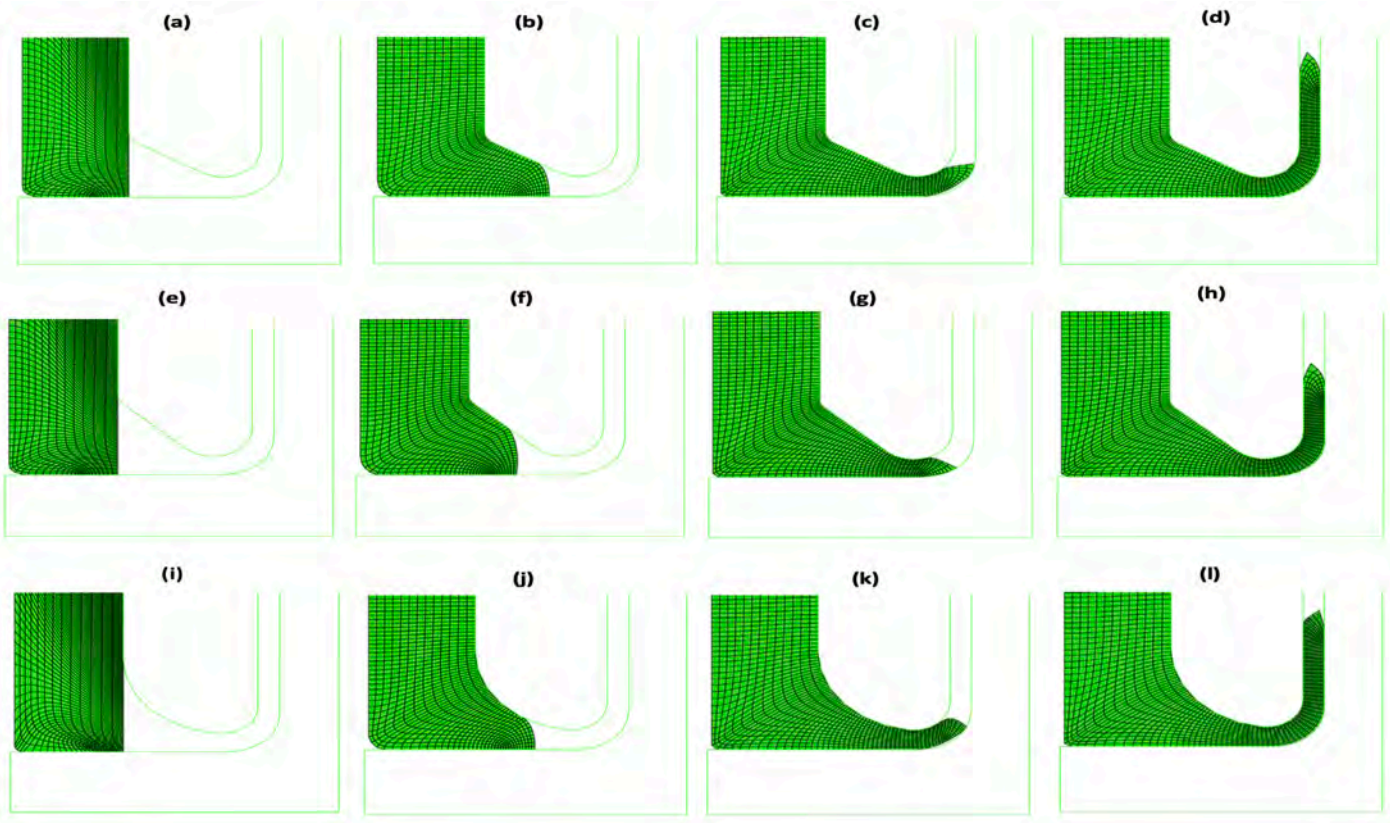

Figure 4. Investigating FEM material flow according to the change of fix-punch geometry parameters with (a-d) channel with the inner channel angle of 30°, (e-h) channel with the inner channel angle of 45°, and (i-l) channel with the inner channel radius of 12.5 mm

microstructural features and mechanical properties in the extruded product. The results show that within the range of geometries studied, the backpressure mechanism effectively controls the material distribution and prevents flow instabilities that may compromise product quality.

Fig. 5 shows the PEEQ distribution in closed-end copper tubes processed with three distinct fix-punch geometries. The results show significant accumulation of PEEQ in the corner and die-entry regions, where the material undergoes the most severe deformation. The strain distribution is highly non-uniform across all examined geometries, with the maximum strains concentrated in regions of highest geometric constraint. The inner channel angle of 30° shows the highest strain in the corner region, while the inner channel angle of 45° and inner channel radius of 12.5 mm show similar, but intensity-dependent, patterns. The variation in strain distribution in these geometries indicates the influence of the die angle and corner radius on the material deformation paths. An important observation is that the spatial distribution and magnitude of strain vary significantly with fix-punch geometry and the progression of the extrusion process. The material in the movable punch region experiences minimal strain, while the material adjacent to the die corner undergoes severe plastic deformation. This inhomogeneous strain field indicates that the die geometry directly controls the intensity of local deformation and the material flow paths. Geometries with larger corner radius or more acute angles produce more gradual material deformation, thereby reducing local strain concentration. The non-uniform strain distribution underscores the need to carefully optimize the die design to achieve balanced material deformation and minimize mechanical property degradation in the extruded product.

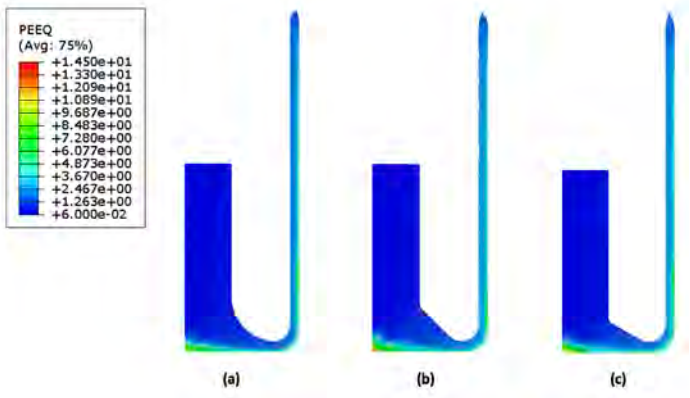

Figure 5. distribution of PEEQ in closed-end copper tubes processed by NBE with varying fix-punch geometries: (a) inner channel radius of 12.5 mm, (b) inner channel angle of 45°, and (c) inner channel angle of 30°.

Some SPD processes, which operate either entirely or partially under pure shear conditions, are derived from conventional metal-forming techniques such as rolling, extrusion, and forging. These procedures involve repeated deformation cycles that generate inhomogeneous strain distributions, resulting in non-uniform microstructure and mechanical properties (Faraji et al., 2024; F. Rahimi et al., 2015). Consistent with this, the non-uniform distribution of

PEEQ in the cross-section of the tube after backward extrusion was observed, as shown in Fig. 5. The PEEQ distribution in the extruded tube was evaluated along two measurement paths. The longitudinal path AD, which extends from the tube inlet (point A) to the closed end (point D), and the radial path EF, which passes through the wall thickness from the inner surface (point E) to the outer surface (point F). Fig. 6 shows the PEEQ profiles for each die geometry investigated.

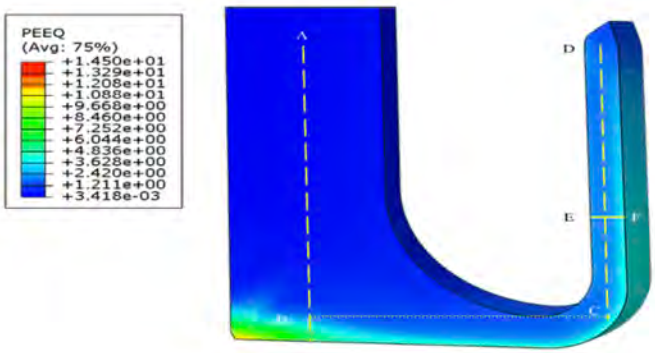

Figure 6. Measurement paths for PEEQ analysis showing radial (EF) and longitudinal (AD) directions on the extruded closed-end tube cross-section

Fig. 7 shows the radial distribution of PEEQ across the tube thickness, examining three distinct die geometries processed via conventional reverse extrusion. The EF measurement path shown in Fig. 6 extends radially from the inner surface of the tube to the outer surface. The strain profiles show a consistent pattern across all geometries. The PEEQ values remain relatively stable in the inner regions, but increase significantly as the material approaches the outer surface. The closed-end tube produced with the inner channel angle of 45° exhibits superior strain uniformity across the wall thickness. The strain variation between inner and outer surfaces is minimal, indicating more consistent properties throughout the wall thickness. The inner channel angle of 30° shows inner PEEQ values averaging 2.69 and outer values reaching 5.76, representing a radial strain increase of approximately 115%.

The inner channel angle of 45° exhibits an internal strain of 2.76 and an external strain of 4.79, corresponding to a radial increase of 74%. The inner channel radius of 12.5 mm exhibits the most pronounced gradient, with inner surface strain of 2.29 and outer surface strain of 6.25, representing a radial increase of 173%. These differential gradients reflect the distinct flow characteristics imposed by each die geometry.

The maximum external surface strain resulting from the inner channel radius of 12.5 mm is 8.6% greater than the inner channel angle of 30° and 28.5% greater than the inner channel angle of 45°. The high plastic deformation on the outer surface promotes progressive grain refinement,

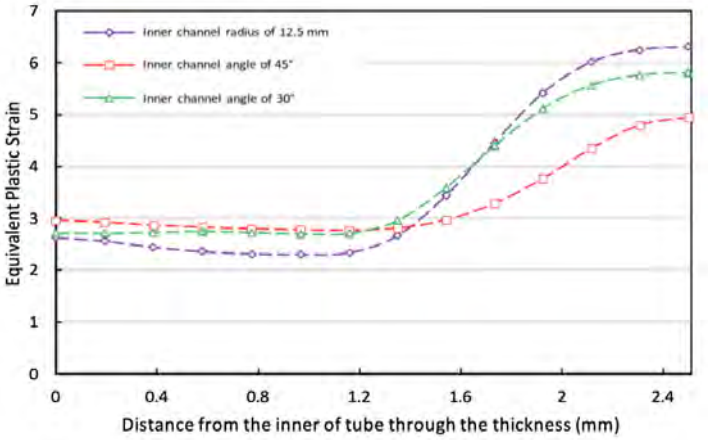

Figure 7. The radial distribution of PEEQ indicates the strain evolution from the inner to the outer surfaces (path EF) of the tube for the three fix-punch geometries examined.

potentially providing superior surface mechanical properties for applications requiring high wear and fatigue resistance (Taherkhani et al., 2024; Taherkhani et al., 2025).

In contrast, the inner channel angle of 45° exhibits better strain uniformity throughout the tube wall thickness. The strain difference between the inner surface (2.76) and outer surface (4.79) is 2.03, representing a 74% radial increase and indicating more uniform property distribution across the cross-section. This differential uniformity reflects an opposing design philosophy. While the inner channel radius of 12.5 mm concentrates deformation toward the outer surface, the inner channel angle of 45° distributes strain more evenly, improving uniformity of the microstructure throughout the tube thickness. In the Accumulative Back Extrusion (ABE) process, a plastic strain of ~4 can be obtained. Higher plastic strain in the inner channel radius of 12.5 mm correlates with a finer grain size and improved mechanical properties (Li et al., 2014). Therefore, the inner channel radius of 12.5 mm offers significant advantages for producing ultrafine-grained copper tubes.

In the direction of AD (shown in Fig. 6), the primary billet underwent significant deformation along the final product due to the strong force from the movable punch. The longitudinal strain distribution along the tube length exhibited distinct deformation characteristics that vary significantly with the die geometry. Fig. 8 shows the evolution of the effective strain in four consecutive zones during a typical reverse extrusion process. In Zone I, the material entered the deformation zone with minimal initial strain (~0.2). However, upon contact with the die geometry, it experienced rapid strain accumulation, with peak values reaching approximately 2.8–3.0 in all geometries. This zone represented the transition from the fix-punch channel entry to the confined channel section. Zone II constituted a transition zone in which strain values stabilized and begin to diverge across the three geometries, and the material gradually fills the channel. Zone III showed stable strain differentiation, with the inner channel angle of 30°

exhibiting significantly higher strain intensity than both the inner channel angle of 45° and the inner channel radius of 12.5 mm geometries, reflecting the stronger geometric constraints of acute angles.

Zone IV, representing the channel exit region, showed stable, convergent strain values of approximately 2.0–2.5 across all geometries, indicating progressive strain homogenization as the material approached the extrusion exit and geometric constraints were reduced. Once the material is fully introduced into the final channel (Zone IV), the effective strain becomes relatively uniform, with less than 10% variation along the channel length across all three geometries. The final PEEQ ranged from 2 to 2.5, indicating significant cumulative deformation. In contrast, achieving comparable strains with equal-channel angular pressing (ECAP) requires multiple passes. Therefore, NBE demonstrated superior efficiency in generating high cumulative plastic strain in a single pass.

Analysis of the simulation results has shown that significant strain inhomogeneities are generated throughout the final product. Die geometry, fix-punch design, and friction conditions affect material flow patterns. The purpose of the strain inhomogeneity index (Ci) is to verify the uniformity of the effective strain distribution within the sample's cross-section (Lee & Kim, 2014). Enhancing uniformity in deformation results in greater consistency in the mechanical characteristics of UFG materials. Specifically, the level of the strain inhomogeneity can be assessed by Eq. 1:

Fig. 9 shows the strain heterogeneity along the tube thickness. The inner channel angle of 45° has the lowest heterogeneity index of 0.60, indicating a relatively uniform and suitable strain distribution. The inner channel angle of 30° produces a higher index of 0.82, while the inner channel radius of 12.5 mm produces the highest heterogeneity of 1.09. These results indicate that the inner channel angle of 45° produces approximately 45% improvement in strain uniformity compared to the inner channel radius of 12.5 mm. The quantitative evaluation presented in Fig. 10 shows that the inner channel angle of 30° has the highest longitudinal strain heterogeneity index of 1.61, confirming that this geometry imparts significant strain variations in the final product. The inner channel angle of 45° yields an average value of 1.56.

In contrast, the inner channel radius of 12.5 mm yielded the lowest strain heterogeneity index of 1.52, indicating the most uniform strain distribution in the direction of material flow in the extrusion. This superior longitudinal uniformity in the inner channel radius of 12.5 mm resulted from the smooth, gradual transition provided by the curved geometry, which progressively loaded the material rather than creating sharp geometric discontinuities. This uniformity in longitudinal strain indicated more stable material flow throughout the deformation region. These findings emphasized that the geometric design significantly influenced the plastic strain distribution, with potential implications for microstructural development and property uniformity in the final extruded product.

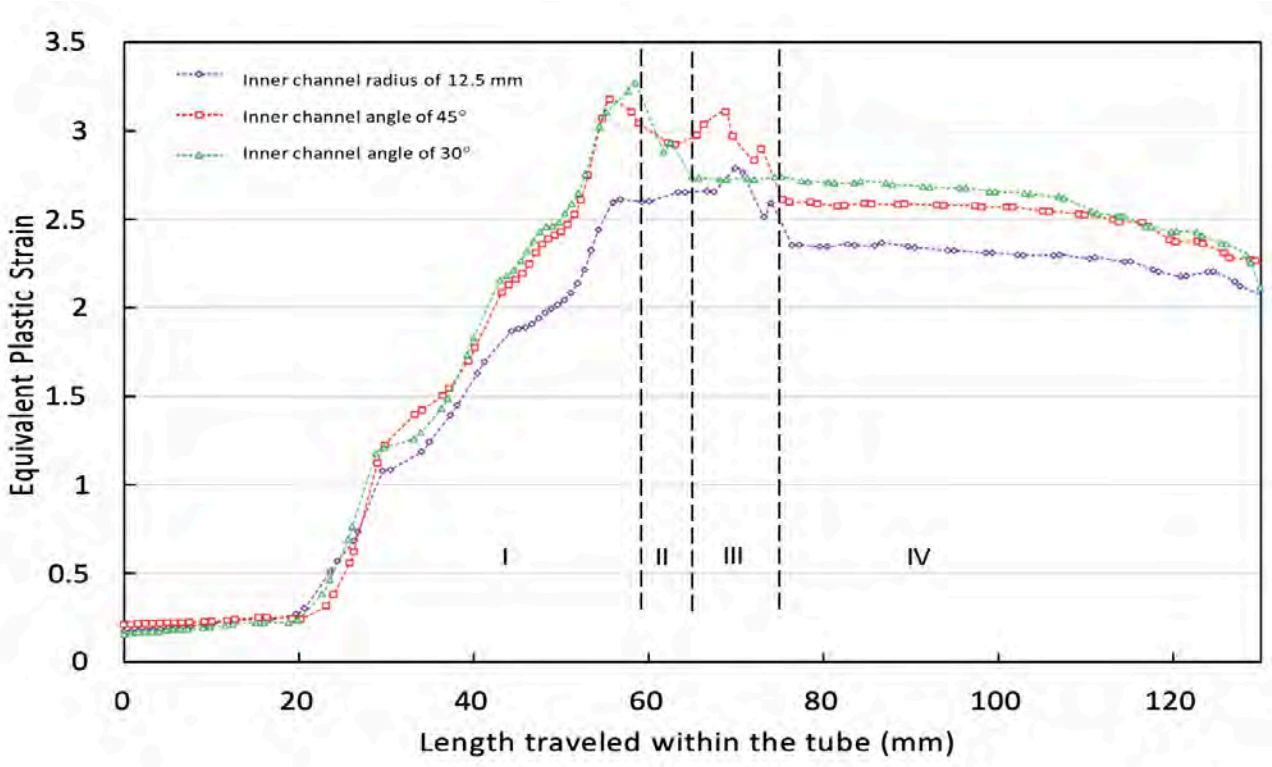

Figure 8. PEEQ distribution along the length of the tube (path AD) for three fix-punch geometries.

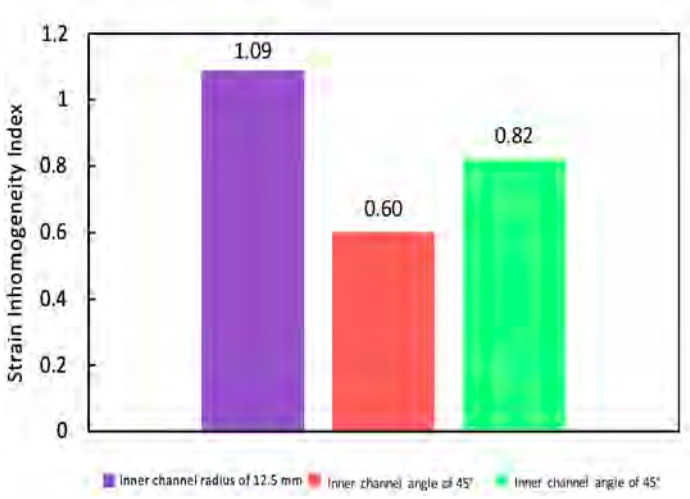

Figure 9. Radial distribution of the strain inhomogeneity index throughout the tube thickness for inner channel angles of 45°, 30°, and an inner channel radius of 12.5 mm.

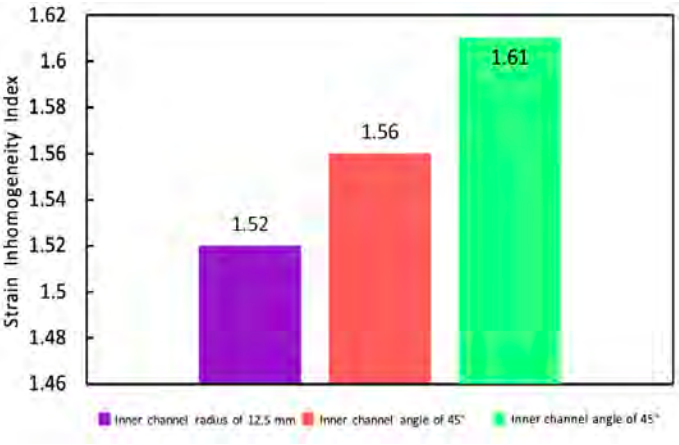

Figure 10. Evolution of the strain inhomogeneity index along the tube length for inner channel angles of 45°, 30°, and an inner channel radius of 12.5 mm

4. Conclusions

This FEM analysis showed that precise die geometry optimization in NBE provides a powerful means to control plastic strain distribution, reduce process forces, and improve the quality of the final product. The quantitative relationships established between the die geometric parameters and final product properties provide a rational framework for die designs. The conclusions are as follows:

- FEM findings indicated that plastic strain exceeding 3.5 was observed in all three cases examined.
- The inner channel angle of 45° resulted in an 18% decrease in required force compared to the inner channel angle of 30°. Hence, reducing the pressure can potentially lead to reduced press capacity and increased die life.
- The die geometry optimization addresses movable punch buckling issues that arise during processing. Additionally, it facilitates extrusion of small-diameter billets that are difficult to form with conventional geometries.
- The uniformity of plastic deformation across the tube width after processing was significantly better than in other instances using a channel with the inner channel radius of 12.5 mm.
- Once the material fills the final channel in the NBE process, it leads to a uniform distribution of plastic deformation and a significant reduction in strain variations along the tube, playing a key role in achieving stable material flow, promoting strain homogeneity, and improving the quality of the final product.

In future research, it is necessary to focus on experimental validation of FEM results to confirm the predicted parameters, particularly the force and strain distributions. Also, developing analyses and establishing relationships between strain homogeneity and microstructural features can provide a more comprehensive understanding of the impact of die geometry on final product performance.

References

Abu-Farha, F. (2012). A preliminary study on the feasibility of friction stir back extrusion. *Scripta Materialia, 66*(9), 615-618.

Ahmadi, S., Faraji, G., Alimirzaloo, V., & Donyavi, A. (2021). Microstructure and mechanical properties of AM60 magnesium alloy processed by a new severe plastic deformation technique. *Metals and Materials International, 27*(8), 2957-2967.

Awasthi, A., Rao, U. S., Saxena, K. K., & Dwivedi, R. K. (2022). Impact of equal channel angular pressing on aluminium alloys: An overview. *Materials Today: Proceedings, 57*, 908-912.

Bakhshi-Jooybari, M., Saboori, M., Hosseinipour, S., Shakeri, M., & Gorji, A. (2006). Experimental and numerical study of optimum die profile in backward rod extrusion. *Journal of Materials Processing Technology, 177*(1-3), 596-599.

Basavaraj, V. P., Chakkingal, U., & Kumar, T. P. (2009). Study of channel angle influence on material flow and strain inhomogeneity in equal channel angular pressing using 3D finite element simulation. *Journal of Materials Processing Technology, 209*(1), 89-95.

Dixit, P. M., & Dixit, U. S. (2008). *Modeling of metal forming and machining processes: by finite element and soft computing methods*: Springer.

El Mehtedi, M., Forcellese, A., Mancia, T., Simoncini, M., & Spigarelli, S. (2019). A new sustainable direct solid state recycling of AA1090 aluminum alloy chips by means of friction stir back extrusion process. *Procedia CIRP, 79*, 638-643.

Faraji, G., Kim, H. S., & Kashi, H. T. (2018). *Severe plastic deformation: methods, processing and properties*: Elsevier.

Faraji, G., Taherkhani, E., & Sabour, M. R. (2024). Cyclic severe plastic deformation processes.

Jafarlou, D., Zalnezhad, E., Hassan, M., Ezazi, M., Mardi, N., Hamouda, A., Yoon, G. H. (2016). Severe plastic deformation of tubular AA 6061 via equal channel angular pressing. *Materials & Design*, 90, 1124-1135.

Lee, D. J., & Kim, H. S. (2014). Finite element analysis for the geometry effect on strain inhomogeneity during high-pressure torsion. *Journal of Materials Science*, 49(19), 6620-6628.

Li, Y., Ng, H. P., Jung, H.-D., Kim, H.-E., & Estrin, Y. (2014). Enhancement of mechanical properties of grade 4 titanium by equal channel angular pressing with billet encapsulation. *Materials Letters,* 114, 144-147.

Lowe, T. C., & Valiev, R. Z. (2000). Investigations and applications of severe plastic deformation (Vol. 80): Springer Science & Business Media.

Majidabad, M. A., Eftekhari, M., & Faraji, G. (2023). Characterization of Mg–9Al–1Zn-0.2 Mn alloy tubes processed by a new modified tube cyclic expansion extrusion (M-TCEE) process. *Journal of Materials Research and Technology*, 24, 7989-8001.

Manafi, B., Shatermashhadi, V., Abrinia, K., Faraji, G., & Sanei, M. (2016). Development of a novel bulk plastic deformation method: hydrostatic backward extrusion. *The International Journal of Advanced Manufacturing Technology*, 82(9), 1823-1830.

Mao, Q., Zhang, Y., Guo, Y., & Zhao, Y. (2021). Enhanced electrical conductivity and mechanical properties in thermally stable fine-grained copper wire. *Communications Materials*, 2(1), 46.

Motallebi Savarabadi, M., Faraji, G., & Eftekhari, M. (2021). Microstructure and mechanical properties of the commercially pure copper tube after processing by hydrostatic tube cyclic expansion extrusion (HTCEE). *Metals and Materials International*, 27(6), 1686-1700.

Rahimi, F., Eivani, A., & Kiani, M. (2015). Effect of die design parameters on the deformation behavior in pure shear extrusion. *Materials & Design,* 83, 144-153.

Rahimi, H., Taherkhani, E., Sabour, M., & Faraji, G. (2025). Fabrication of Cu–Al MMC with randomly-oriented continuous intermetallic layers via entangled twisting fiber plasma sintering. *Journal of Materials Research and Technology.*

Shatermashhadi, V., Manafi, B., Abrinia, K., Faraji, G., & Sanei, M. (2014). Development of a novel method for the backward extrusion. *Materials & Design (1980-2015)*, 62, 361-366. doi:https://doi.org/10.1016/j.matdes.2014.05.022

Taherkhani, E., Sabour, M., Esmaeilnia, A., Aghchai, A. J., Straumal, B., & Faraji, G. (2025). Refinement of ultrahigh aspect ratio pure aluminum through novel hydrostatic twist extrusion: microstructural and mechanical insights. *Journal of Materials Research and Technology*.

Taherkhani, E., Sabour, M., & Faraji, G. (2024). Sustainable magnesium recycling: Insights into grain refinement through plastic deformation-assisted solid-state recycling (SSR). *Journal of Magnesium and Alloys, 12*(10), 3947-3966.

Taherkhani, E., Sabour, M., Khajepour, M., Safahi, H., Aghchai, A. J., Baniasadi, M., & Faraji, G. (2025). Hydrostatic twist extrusion: the effects of hydrostatic fluid pressure on deformation characteristics. *International Journal on Interactive Design and Manufacturing (IJIDeM)*, 1-12.

Toth, L. S., Chen, C., Pougis, A., Arzaghi, M., Fundenberger, J.-J., Massion, R., & Suwas, S. (2019). High pressure tube twisting for producing ultra fine grained materials: a review. *Materials Transactions, 60*(7), 1177-1191.

Uyyuru, R. K., & Valberg, H. (2006). Physical and numerical analysis of the metal flow over the punch head in backward cup extrusion of aluminium. *Journal of Materials Processing Technology, 172*(2), 312-318.

Valiev, R. Z., Estrin, Y., Horita, Z., Langdon, T. G., Zehetbauer, M. J., & Zhu, Y. (2016). Producing bulk ultrafine-grained materials by severe plastic deformation: ten years later. *JOM, 68*(4), 1216-1226.

Wang, J. T., Li, Z., Wang, J., & Langdon, T. G. (2012). Principles of severe plastic deformation using tube high-pressure shearing. *Scripta Materialia, 67*(10), 810-813.

Zeng, J., Li, J., Dong, S., Wang, F., Wang, F., Jin, L., & Dong, J. (2024). Optimization of hot backward extrusion process parameters for seamless tube of Mg-8Gd-3Y alloy by finite element simulation. *Journal of Materials Engineering and Performance, 33*(5), 2453-2461.

Zohrevand, M., Rezaei, A. R., Sabour, M. R., Taherkhani, E., & Faraji, G. (2023). Recent progress on SPD processes empowered by hydrostatic pressure. *Materials Transactions, 64*(8), 1663-1672.

IJAMMP

Taguchi Optimisation of Friction Stir Welding Parameters for Pure Aluminium under Different Backing Conditions

Sufian Raja [1,2], Aleksey Yushin [1,b *], Chunlei He [2,c *], Pavlo Goncharov [1], Fomichev Evgenii [1], Vadim Verkhorubov [1], Huan Miao [3]

RESEARCH ARTICLE

ARTICLE INFO

Keywords:

Backing condition; Friction stir welding; Joint efficiency; Pure aluminium; Taguchi method

Article History

*Received:*24 October 2025
*Revised:*19 February 2026
*Accepted:*28 February 2026
Published:

ABSTRACT

Friction stir welding (FSW) of pure aluminium is highly sensitive to the backing condition because the backing plate not only supports the workpiece against downward forging but also governs heat extraction from the weld zone. This study optimized the FSW parameters for 6-mm pure aluminium under three backing conditions: aluminium, mild steel, and an insulating fly-ash bed, and evaluated their effects on tensile strength, joint efficiency, hardness, fracture morphology, and phase stability. Butt joints were produced on a vertical milling machine using a low-cost dedicated fixture. A Taguchi L9 orthogonal array was employed to examine tool rotational speed, welding speed, and tool geometry (straight cylindrical, triangular, and straight square), followed by ANOVA and regression-based optimisation. The base metal showed 180.793 MPa ultimate tensile strength, 34.3% elongation, and 75.2 HRB hardness. The aluminium backing condition yielded 93.20-113.41 MPa and 51.55-62.72% joint efficiency, while mild steel gave 72.43-139.10 MPa and 40.06-76.93%. The fly-ash bed produced the best performance, achieving 107.10-165.78 MPa and 59.23-91.69% joint efficiency, with a maximum tensile strength of 165.78 MPa. Hardness was highest under aluminium backing and remained closer to the base metal under fly ash. Fractography showed tunnel defects, voids, and coarse dimples in the aluminium condition, fewer severe features in mild steel, and abundant fine dimples indicative of ductile fracture in the fly-ash condition. XRD showed no additional peaks, confirming the absence of foreign material transfer into the nugget. These findings show that backing condition is a key optimisation variable and that fly ash is an effective low-cost insulating backing medium for improving weld performance in pure aluminium FSW.

1. Introduction

Aluminium and its alloys continue to be among the most important structural materials for lightweight engineering because they provide a useful combination of low density, good corrosion resistance, and adequate specific strength. These properties make them well-suited to transportation, marine, aerospace, and general fabrication applications (Bharti et al., 2023; Feddal et al., 2025). In these sectors, however, the structural usefulness of aluminium depends not only on the base material itself but also on the soundness of the joints used to connect plates, extrusions, and formed parts. For this reason, friction stir welding (FSW) continues to attract strong academic and industrial attention as a solid-state joining technique that avoids bulk melting and can therefore reduce many of the problems associated with conventional fusion welding, such assolidification-related defects, high distortion, and inconsistent weld quality (Heidarzadeh et al., 2021; Isa et al., 2021; Lunetto et al., 2025; Raja et al., 2016).

1 Daou (Shaoxing) Technology Co., Ltd, Room 6048, Building 6, East Zone, Keqiao International Park, No.199 Chuangyi Road, Keqiao District, Shaoxing City, Zhejiang Province, China
2 Tianjin Key Laboratory of Equipment Design and Manufacturing Technology, Tianjin University, Tianjin 30054, China
3 College of Materials Engineering, North China Institute of Aerospace Engineering, Langfang, 065000, China.
Corresponding authors:

Recent review papers confirm that FSW remains one of the most intensively studied solid-state joining processes for aluminium systems, not only for standard butt and lap joints but also for more complex industrial geometries and dissimilar material combinations. At the same time, post-weld property tailoring and process modelling are receiving increasing research interest (Amini et al., 2022; Choi et al., 2025; Habba & Ahmed, 2025; Raja et al., 2020).

Despite these advantages, FSW remains highly sensitive to process control because joint formation depends on a complex interaction between frictional heat generation, plastic deformation, material flow, and final consolidation beneath the shoulder and around the pin (Heidarzadeh et al., 2021; Raja et al., 2024; Yamani et al., 2022). As a result, weld quality is strongly affected by the main process parameters, especially tool rotational speed, welding speed, and tool geometry. Many recent studies have therefore focused on the statistical and computational optimisation of FSW conditions for aluminium alloys, using approaches such as Taguchi design, grey relational analysis, response surface methodology, artificial intelligence, and hybrid predictive models to identify parameter combinations that maximise tensile strength, hardness, or overall joint efficiency (Abdelhady et al., 2024; Ahmed et al., 2022; Asmare et al., 2020; Clark & Ragai, 2025; Kubit et al., 2022; Manjunatha et al., 2025; Myśliwiec et al., 2024; Soto-

Diaz et al., 2025). These studies consistently show that unsuitable parameter combinations can lead either to insufficient heat input and incomplete consolidation or to excessive heat input and mechanical softening, both of which reduce weld performance (Abdelhady et al., 2024; Ahmed et al., 2022; Kubit et al., 2022; Mohd Jamil et al., 2024; Raja et al., 2022).

A substantial part of the recent literature has concentrated on aluminium alloys such as AA6061, AA2024, AA5052, AA5083, and AA5754, because these alloys are widely used in engineering and because their responses to friction stir welding are strongly shaped by thermal history (Feddal et al., 2025; Lunetto et al., 2025). In AA6061 and related systems, the combined effects of tool profile, rotational speed, feed rate, and thermal cycle have been linked to tensile performance, hardness variation, fracture morphology, and defect formation (Abdollahzadeh et al., 2021; Wahjudi et al., 2024). Studies on conventional, bobbin-tool, friction stir spot, and modified-joint configurations have shown that tensile strength and fracture mode are highly sensitive to the degree of consolidation and local thermal exposure, while hardness distributions are likewise affected by weld geometry and process condition (Tinguery et al., 2023; Tiwan et al., 2023; Yacout et al., 2025). Recent work has also continued to use fractography as an essential validation tool for distinguishing defect-assisted fracture from more ductile failure modes in aluminium FSW joints (Abdollahzadeh et al., 2021; Wahjudi et al., 2024).

Beyond the commonly discussed tool and travel parameters, an equally important but often underemphasised factor is the thermal boundary condition imposed by the backing system. In the present study, the term backing condition refers to the material or medium placed beneath the workpiece to provide mechanical support during welding while simultaneously governing heat extraction from the lower side of the joint. Accordingly, the backing system acts both as a structural support and as a thermal pathway, and can therefore alter peak temperature, cooling rate, through-thickness temperature gradient, and the stability of plasticised material flow. The significance of this issue has become more visible in recent years. Studies on aluminium alloys have shown that changes in backing plate material or thermal boundary condition can modify microstructure, hardness, strength, and defect susceptibility (Das et al., 2024; Mondal et al., 2024; Raja et al., 2021). High-conductivity support conditions may intensify heat loss and thereby increase the risk of insufficient consolidation, whereas thermally resistant or differently configured support conditions can retain heat and alter weld behaviour. Recent work on backing-plate effects, dual-backing concepts, and large-thickness thermal boundary control confirms that backing is not merely a passive fixture detail but a variable with direct metallurgical and mechanical consequences (Acharya et al., 2024; Al-Allaq et al., 2024; Ambrosio et al., 2024; Das et al., 2024; Verma et al., 2025).

For heat-treatable alloys such as AA6061, this thermal-boundary issue is especially important because the weld thermal cycle influences precipitate evolution, local softening, hardness minima, and ultimately failure location (Zhou et al., 2024). Recent studies have shown that mechanical performance in friction stir-welded AA6061 joints is closely linked to hardness evolution and local fracture behaviour, and that the interpretation of tensile data becomes stronger when supported by hardness mapping and fractographic analysis (Abdelhady et al., 2024; Wahjudi et al., 2024; Yacout et al., 2025).

However, although recent optimisation and property studies on aluminium alloys are extensive, several limitations remain when viewed from the perspective of a practical, mechanically focused manuscript. First, most recent studies deal with alloy-specific systems such as AA6061, AA2024, AA5754, AA5052, or composite-containing aluminium systems, while comparatively fewer works isolate the effect of backing condition in a simpler pure-aluminium system where precipitation-related complexity is absent.

Second, many optimisation studies treat the backing arrangement as fixed and concentrate primarily on tool geometry and speed variables (Abdelhady et al., 2024; Ahmed et al., 2022; Kubit et al., 2022). Third, while advanced modelling and machine-learning methods are increasingly reported, there remains clear value in experimentally grounded, low-cost, shop-floor-compatible studies that combine parameter optimisation with direct mechanical verification, particularly for conditions such as conventional vertical milling machines (Manjunatha et al., 2025; Myśliwiec et al., 2024; Soto-Diaz et al., 2025). In this context, a controlled comparison among conductive and insulating backing conditions remains both scientifically relevant and industrially useful (Feddal et al., 2025; Yacout et al., 2025).

The present study was therefore designed to investigate friction stir welding of 6-mm pure aluminium under different backing conditions and to optimise the process parameters for maximum tensile strength using a Taguchi L9 orthogonal array. Unlike studies centred on extensive metallurgical characterisation, the present work is positioned as a process-optimisation and weld-performance study in which three backing conditions are compared under the same experimental framework. The effects of rotational speed, welding speed, and tool geometry are evaluated in relation to tensile strength and joint efficiency, while hardness mapping and SEM fractography are used to support the interpretation of thermal and failure responses.

X-ray diffraction is additionally employed as a conservative verification step to confirm that the backing condition does not introduce detectable foreign material into the weld zone. In this way, the study seeks to clarify whether backing condition can be treated as a practical optimisation variable in pure-aluminium FSW and whether an insulating backing medium can provide a low-cost route for improving weld performance.

2. Materials and Methods

Commercially available pure rolled aluminium was used as the base material in the present investigation because it allows the friction stir welding response to be examined without the added complexity of alloying-element effects. The rolled plates were cut into 100 × 70 × 6 mm coupons and welded in a butt-joint configuration. EDX analysis of the parent plate confirmed that the workpiece was aluminium, and the base metal exhibited an ultimate tensile strength of 180.793 MPa, elongation of 34.3%, and hardness of 75.2 HRB, as shown in Tables 1 and 2. Table 1 reports the experimentally measured EDX composition of the parent plate, while Table 2 reports the experimentally measured base-metal tensile and Rockwell hardness values obtained in this study. Tensile testing was conducted according to ASTM E8/E8M, and hardness measurement was performed using the Rockwell method in accordance with ASTM E18.

Table 1. Chemical composition of the base material

Element	Weight (%)	Atomic (%)
Al	100.00	100.00

Table 2. Mechanical properties of the base material

Properties	Value
Ultimate tensile strength (MPa)	180.793
Elongation (%)	34.3
Hardness (HRB)	75.2

Since the welding trials were carried out on a vertical milling machine, the development of a reliable fixture was a necessary part of the experimental design. A dedicated fixture was therefore designed and fabricated in-house from mild steel to provide proper alignment, rigid support, and resistance against the unbalanced forces generated during welding, as shown in Figure 1. The schematic of the fixture is shown in Figure 1 (a) and Figure 1 (b). The fabricated fixture assembly is shown in Figure 1 (c). The FSW experiments were performed on a vertical milling machine with 8 spindle-speed steps (250-4500 rpm), manual table feed, and 1 hp motor power. The tool was mounted using a suitable collet, and because the machine did not provide independent tilt-angle adjustment, the process variables were selected within the available machine and setup limitations.

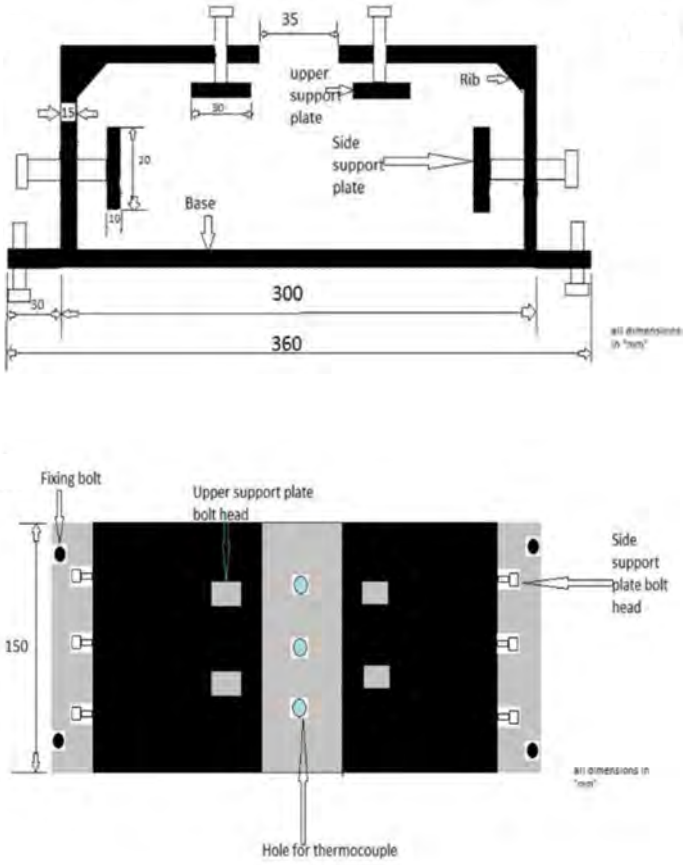

Figure 1. (a) Front view of developed fixture, (b) top view of developed fixture, and (c) complete fixture assembly

The welding tools were fabricated from stainless steel (Grade 310) because of its high-temperature capability and adequate ductility under the combined torque and vertical pressure of the FSW process. Grade 310 stainless steel was selected not only for strength and hot-hardness retention during FSW, but also because its thermal conductivity is much lower than that of pure aluminium. As a result, the tool itself did not behave as a major heat sink relative to the aluminium backing; instead, it helped retain frictional heat locally around the shoulder–pin region, whereas the backing condition primarily governed the through-thickness heat extraction from the weld (Das et al., 2024; Park et al., 2020). Three tool-pin geometries were prepared: straight cylindrical (SC), triangular (TL), and straight square (SS). The tools were machined initially from a 22 mm diameter stainless-steel bar. The straight cylindrical tool was produced directly by lathe machining, whereas the square and triangular profiles were prepared by first machining a cylindrical pin and then forming the required profile on a milling machine. The fixed tool dimensions used in the study were a 5 mm probe length, 6 mm probe diameter/side length, and 18 mm shoulder diameter, as shown in Figure 2 and tabulated in Table 3.

Table 3. Tool geometry used in FSW of Al

Parameter	Value
Tool material	Stainless steel (Grade 310)
Tool profiles	Straight cylindrical (SC) Triangular (TL) Straight square (SS)
Probe length	5 mm
Probe diameter/ side length	6 mm
Shoulder diameter	18 mm

To examine the effect of thermal boundary conditions on weld performance, three distinct backing conditions were used. In the aluminium condition, the bottom back plate, top support, and side support were made of pure aluminium, as shown in Figure 3 (a). In the mild-steel condition, the supporting enclosure was made of mild steel, as shown in Figure 3(b). In the fly-ash backing condition, a rigid mild-steel box was filled with dry fly ash, and the lower surface of the aluminium plate rested directly on the top surface of the fly-ash bed during welding. Thus, the specimen was mechanically supported by the steel enclosure while the immediate lower interface beneath the plate was a particulate insulating layer rather than a solid metallic back plate, as shown in Figures 3 (c) and (d).

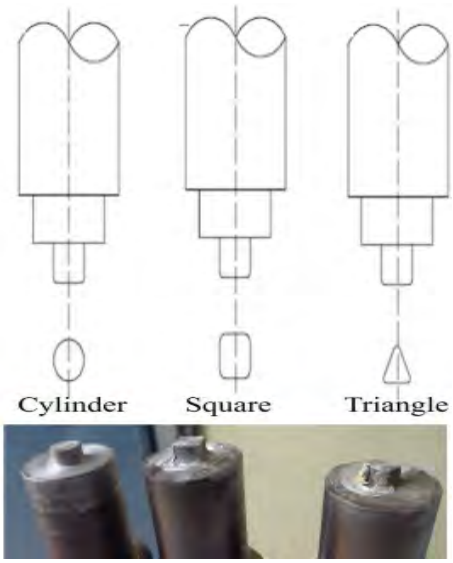

Figure 2. Tool geometry employed in the friction stir welding experiments

In each case, the welded plate was kept in the same condition until cooling to room temperature. The three conditions were selected because they provide a wide variation in thermal conductivity, namely 205–250 W/m·K for pure aluminium, 40–50 W/m·K for mild steel, and 0.15–1.3 W/m·K for fly ash.

Fly ash was selected as the insulating filler because it is a particulate oxide-rich residue with much lower thermal conductivity than the metallic backing materials. Dry fly ashes are reported to exhibit low thermal conductivity, and fly-ash-based materials are widely used in thermal-insulation applications. In the present work, EDX of the fly ash detected C, O, Al, Si, and K as the major elements, confirming that the filler was an oxide-rich particulate medium suitable for use as a thermally resistive backing condition rather than a metallic heat sink, as shown in Figure 4.

The experimental design was based on a Taguchi L9 orthogonal array, selected to evaluate the effects of three major process variables under the constraints of the machine and setup. These variables were tool rotational speed, welding speed, and tool geometry, each examined at three levels. Prior trial welds were carried out to confirm the feasible parameter range, and the L9 array was selected because it allowed the effects of the three factors to be studied with an economically manageable number of runs while satisfying the required degrees of freedom for the design. The three levels considered were 544, 1100, and 1850 rpm for rotational speed; 60, 90, and 120 mm/min for welding speed; and SC, TL, and SS for tool geometry, as shown in Table 4 and Table 5.

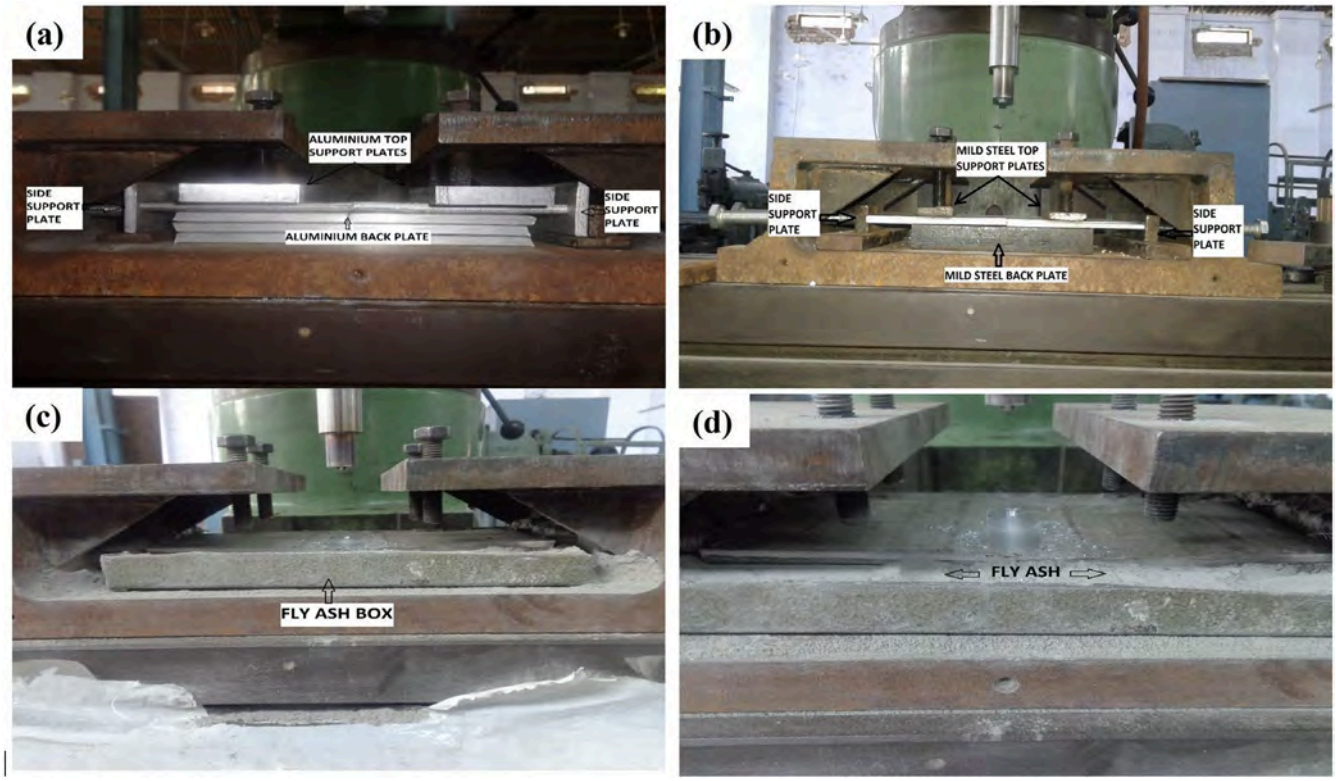

Figure 3. Backing conditions used in the present work: (a) aluminium backing condition setup, (b) mild-steel backing condition setup, (c) fly-ash backing condition showing the plate positioned over the fly-ash-filled steel box during welding,

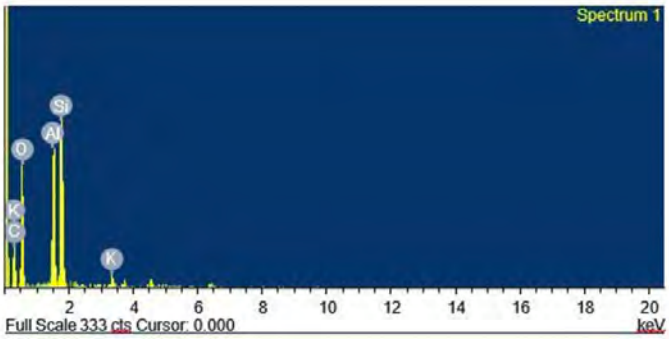

Figure 4. SEM-EDX of fly ash showing different elements

Table 4. Process parameters and levels used in the Taguchi design

Parameter	Level 1	Level 2	Level 3
Tool rotational speed (rpm)	544	1100	1850
Welding speed (mm/min)	60	90	120
Tool geometry	Straight cylinder (SC)	Triangular (TL)	Straight square (SS)

Table 5. L9 orthogonal array used for the welding experiments

Run	Tool rotational speed (rpm)	Welding speed (mm/min)	Tool geometry
1	544	60	SC
2	544	90	TL
3	544	120	SS
4	1100	60	TL
5	1100	90	SS
6	1100	120	SC
7	1850	60	SS
8	1850	90	SC
9	1850	120	TL

After welding, the joints were sectioned and machined into tensile specimens according to ASTM E8 geometry, as depicted in Figure 5 (a). Tensile testing was carried out on a digitally controlled servo-hydraulic dynamic testing machine using a displacement-controlled crosshead speed of 2 mm/min. Weld performance was evaluated primarily through tensile strength and joint efficiency. Joint efficiency was determined with respect to the base-metal tensile strength.

Hardness measurements were performed using a digital Rockwell hardness tester. The hardness values were recorded from the weld centre at 5 mm increments on both the advancing and retreating sides. Measurements were taken at three thickness levels, namely 2 mm, 4 mm, and the bottom/root region, measured from the top surface of the weld shown in Figure 5 (b). This layout allowed the crown-to-root hardness variation to be assessed in addition to the transverse hardness profile across the joint.

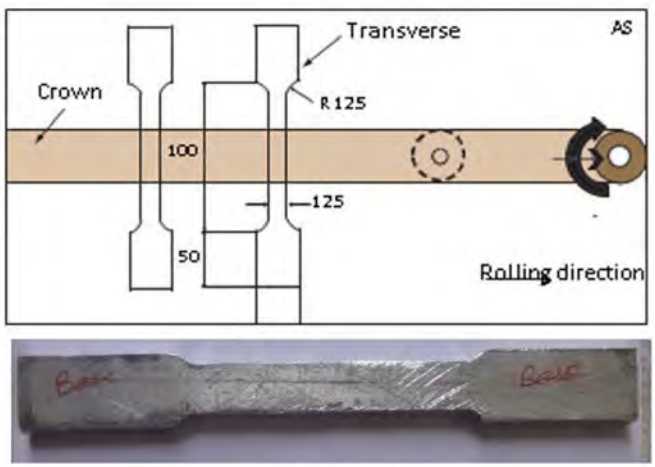

(a)

DISTANCE FROM TOP SURFACE (mm)		AS			weld center	RS		
	0 2 4 6	-15	-10	-5	0	5	10	15

(b)

Figure 5. (a) Standard tensile test specimen (b) hardness-mapping layout

After tensile testing, the fracture surfaces of selected specimens were examined using scanning electron microscopy (SEM) in order to analyse fracture morphology and relate failure mode to weld quality. In addition, X-ray diffraction (XRD) was performed on the base metal and selected welds to examine whether any temperature-related phase changes or unwanted foreign particles were present in the nugget region, particularly in the case of the fly-ash backing condition. For the Taguchi analysis, the tensile-strength data were converted to signal-to-noise ratios using the larger-the-better criterion, and ANOVA was performed to determine the significance of each process parameter.

3. Results

3.1 Weld appearance and macroscopic integrity

A clear difference in weld surface quality was observed among the three backing conditions, as depicted in Fig. 6. Under the aluminium backing condition, the welded specimens showed visible defects, including flash formation and tunnel-type defects, indicating that the weld bead was not fully stable under the high-conductivity backing condition (Figure 6 (a),(b)). In contrast, the mild-steel backing condition produced a smoother weld bead, and records that the major visible defects observed in the aluminium condition were eliminated, as shown in Fig 6(c). The most satisfactory macroscopic appearance was obtained in the fly-ash backing condition, where the welded zone was reported to have a smooth, defect-free, mirror-like surface compared with both metallic backing conditions, Figure 6 (d). These observations provide the first indication that the backing condition strongly influenced heat retention and weld-bead stability during the process.

3.2 Tensile strength and joint efficiency

The base metal used in this work exhibited an ultimate tensile strength of 180.793 MPa, which was taken as the reference for joint-efficiency calculations. Across all experiments, the tensile response was strongly affected by backing condition, and the overall trend showed that joint performance improved as the backing condition became less conductive and more thermally resistive, as depicted in Table 6.

The aluminium backing condition gave the lowest tensile response among the three backing conditions. The measured tensile strengths ranged from 93.20 to 113.41 MPa, corresponding to joint efficiencies of 51.55% to 62.72%. The best result in this condition was 113.41 MPa with 62.72% joint efficiency. This comparatively low performance is consistent with the defective weld appearance seen in the same condition.

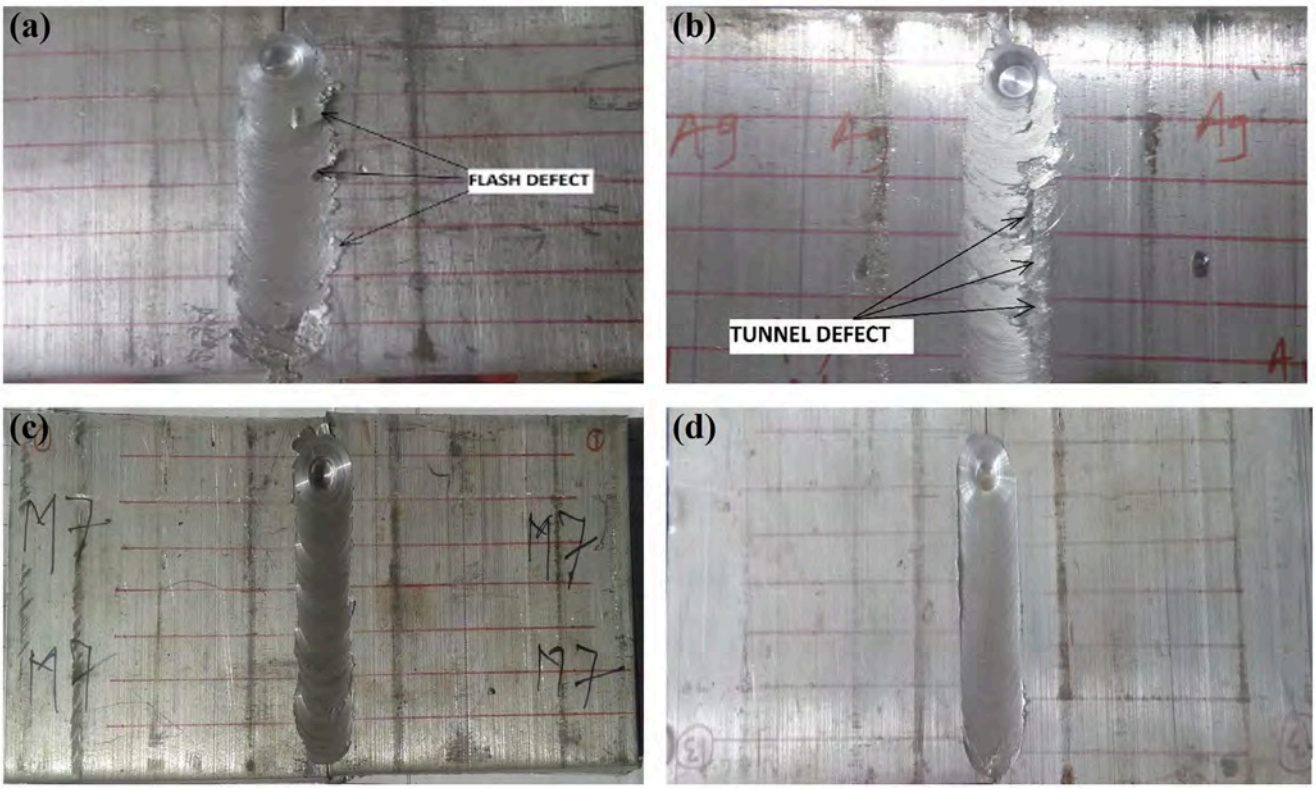

Figure 6: Weld appearance obtained under different backing conditions: (a,b) aluminium backing condition, (c) mild-steel backing condition, and (d) fly-ash-bed backing condition

Table 6. Tensile strength and joint efficiency under different backing conditions

Backing condition	Tensile strength range (MPa)	Maximum tensile strength (MPa)	Joint-efficiency range (%)	Maximum joint efficiency (%)
Aluminium	93.20–113.41	113.41	51.55–62.72	62.72
Mild steel	72.43–139.10	139.10	40.06–76.93	76.93
Fly ash	107.10–165.78	165.78	59.23–91.69	91.69

The mild-steel backing condition improved the tensile response substantially. The measured strength values ranged from 72.43 to 139.10 MPa, and joint efficiency varied from 40.06% to 76.93%. The best weld under these conditions reached 139.10 MPa, corresponding to 76.93% joint efficiency. The mild-steel condition, therefore, produced a clear improvement over the aluminium condition, which agrees with the smoother weld-bead morphology and lower defect severity.

The fly-ash backing condition produced the best overall mechanical performance. The measured tensile strength ranged from 107.10 to 165.78 MPa, while joint efficiency ranged from 59.23% to 91.69%. The highest value obtained in the entire study was 165.78 MPa, corresponding to 91.69% joint efficiency. The results further note that, in this condition, joint efficiency sometimes approached 90% of the base-metal strength, and the weld nugget surface was particularly fine. This confirms that the thermally insulating fly-ash bed provided the most favourable welding condition among the three cases examined.

3.3 Taguchi response analysis and ANOVA

The Taguchi single-response analysis in Table 7 showed that the relative importance of the process parameters changed with backing condition. For the aluminium condition, the ANOVA results revealed that welding speed was the most influential factor for tensile strength, contributing 60.31%, followed by tool rotational speed (17.86%) and tool geometry (16.5%). The corresponding prediction plot showed reasonable agreement between experimental and predicted tensile strength, with R^2 = 0.9469.

For the mild-steel condition, the dominant factor shifted from welding speed to tool rotational speed, which contributed 58.62% to the tensile-strength response. Welding speed contributed 32.26%, while tool geometry contributed 7.7%. The model showed strong adequacy, with R^2 = 0.9864, indicating close agreement between measured and predicted values.

Table 6. Tensile strength and joint efficiency under different backing conditions

Backing condition	Dominant parameter	Contribution (%)	Other contributions (%)	Predictive adequacy
Aluminium	Welding speed	60.31	Rotational speed: 17.86; Tool geometry: 16.5	$R^2 = 0.9469$
Mild steel	Rotational speed	58.62	Welding speed: 32.26; Tool geometry: 7.7	$R^2 = 0.9864$
Fly ash	Rotational speed	54.68	Welding speed: 22.0; Tool geometry: 23.0	$R^2 = 0.9979$

For the fly-ash condition, tool rotational speed again remained the dominant factor, with a contribution of 54.68%, while welding speed and tool geometry contributed 22.0% and 23.0%, respectively. The predictive relation for this condition gave the highest goodness of fit, with $R^2 = 0.9979$, indicating excellent agreement between experimental and predicted tensile strengths. This condition also yielded the highest joint efficiency and the most favourable weld appearance.

3.4 Hardness response under different backing conditions

The hardness results showed a trend opposite to the tensile-strength trend, as shown in Figure 7. In the aluminium condition, the hardness of the welded specimen was reported to be higher than that of the base metal at the measured locations. The results attribute this to a quenching effect caused by rapid heat extraction through the aluminium back plate, top plate, and side plates. It was also observed that hardness increased in the nugget zone and then decreased toward the advancing and retreating sides.

In the mild-steel condition, the hardness of the welded specimen also remained generally above the base metal, but the trend was more moderate. It was observed that the hardness at 4 mm thickness was nearly similar to that of the base metal and that, unlike the aluminium condition, no strong quenching effect existed because heat transfer through mild steel was only moderate. In this condition, the top and bottom regions tended to show relatively higher hardness than the interior levels.

In the fly-ash condition, the hardness profile was reported to remain close to the base-metal hardness. A clear gradient was observed from crown to root, with hardness being highest near the crown and decreasing downward; the root region sometimes showed hardness values even below the base metal. The results directly relate this behaviour to the thermal insulation of the fly-ash bed, which restricted heat loss from the bottom side and eliminated the quenching-like effect seen in the metallic backing conditions. Thus, although the fly-ash condition gave the highest tensile strength and joint efficiency, it did not give the highest hardness.

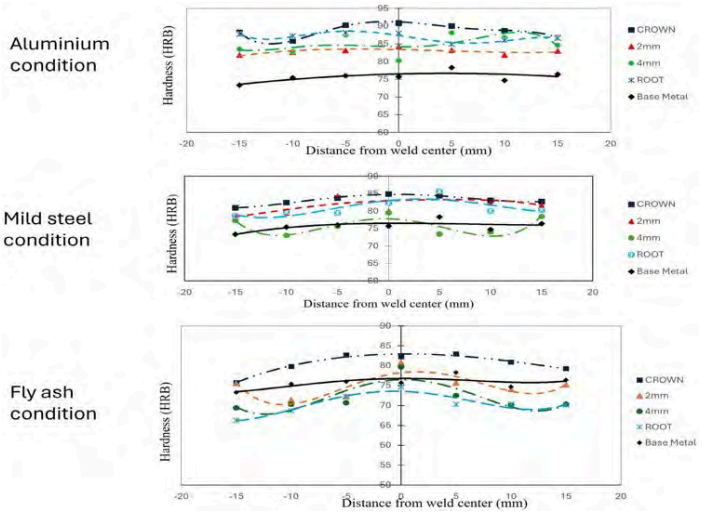

Figure 7. Hardness distributions under the three backing conditions: aluminium condition, mild-steel condition, and fly-ash condition

3.5 Fractography of tensile specimens

SEM fractography provided direct evidence of the failure mode under the different backing conditions, as shown in Figure 8. The base metal showed fine dimples with micro-void coalescence, which is characteristic of ductile fracture (Figure 8(a)). This base-metal morphology was used as the reference condition for comparison with the welded joints.

In the aluminium condition, the fracture surface showed tunnel defects, voids, featureless regions, and coarse dimples (Figure 8(b)). It was noted that a trans-granular fracture mode was present near the defect region, indicating a rough fracture surface with high crack-deflection angles. These features are fully consistent with the lower tensile performance measured in this condition.

In the mild-steel condition, the fractured tensile specimens showed fewer voids, fewer featureless regions, and fewer coarse dimples than those observed for the aluminium condition, as shown in Figure 8(c). Although the morphology was improved, it still did not reach the ductile appearance of the base metal or the fly-ash condition. The mild-steel condition, therefore, represents an intermediate fracture response between the highly conductive aluminium condition and the insulating fly-ash condition.

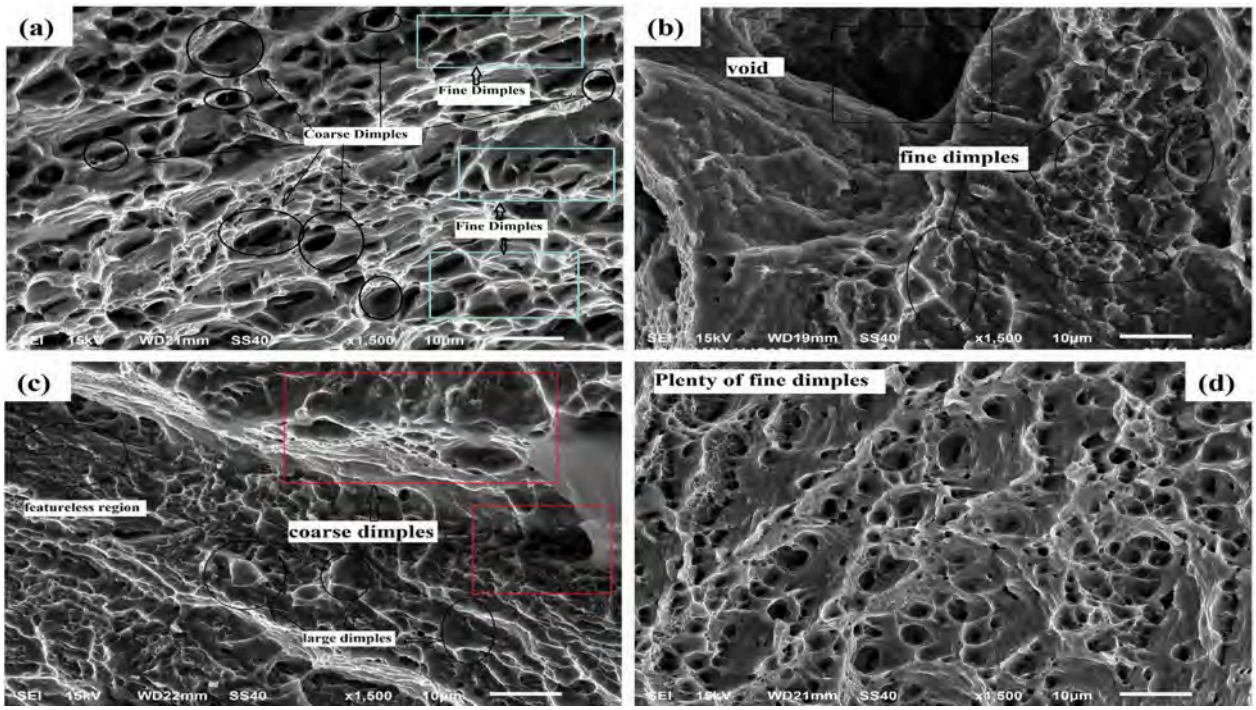

Figure 8. SEM fractography of tensile-tested specimens, (a) base metal, (b) aluminium backing condition, (c) mild-steel backing condition, and (d) fly-ash-bed backing condition

The most favourable fracture morphology was obtained in the fly-ash condition. The fractured surfaces were described as containing plenty of dimples with uniform sizes and depths, indicating typical ductile fracture, as depicted in Figure 8 (d). The dimples in the fly-ash condition were far more numerous than those in the aluminium and mild-steel conditions, and the fracture morphology was nearly similar to that of the base metal.

3.6 XRD analysis

XRD analysis was carried out on the base metal and on selected specimens from the three process conditions, as shown in Figure 9. The recorded patterns showed that there were no precipitates in the aluminium base material, which agrees with the EDS result indicating 100% aluminium.

More importantly, the XRD results showed that no foreign material was introduced during welding. This was particularly relevant for the fly-ash condition, because there was a possibility of fly-ash induction into the welded region. The XRD patterns of representative fly-ash specimens, such as F2 (Fly ash condition) and F5 (Fly ash condition), showed the same peaks as the other conditions, thereby confirming that fly ash was not introduced into the nugget zone.

4. Discussion

The present results show that the backing condition was not merely a supporting arrangement, but a governing thermal boundary condition that substantially altered weld formation, tensile response, hardness behaviour, and

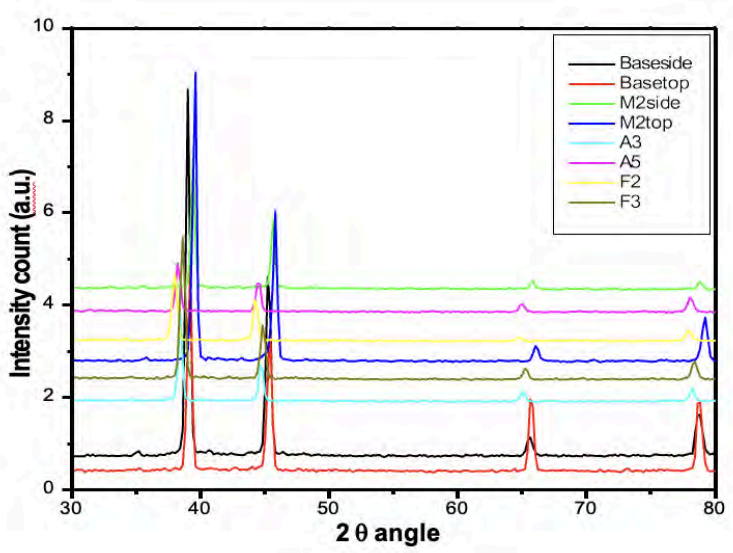

Figure 9: XRD patterns of the base metal and selected welded specimens from the aluminium, mild-steel, and fly-ash conditions

fracture morphology. In the present work, the change from aluminium backing to mild-steel backing and finally to the fly-ash bed progressively improved weld appearance and joint efficiency, with the fly-ash condition producing the highest tensile strength (165.78 MPa) and maximum joint efficiency (91.69%), whereas the aluminium condition gave the lowest efficiency and exhibited flash and tunnel-type defects. This trend indicates that the local heat extraction pathway beneath the weld played a decisive role in determining whether the material remained sufficiently plasticised for proper consolidation. Because the same Grade 310 tool was used in all experiments, the differences among the three cases are attributed mainly to backing-controlled heat extraction rather than to changes in tool thermal response; however, the relatively low thermal conductivity of the stainless-steel tool likely contributed to local heat retention in all runs (Das et al., 2024). Similar conclusions have been reported in recent backing-plate studies, where backing selection modified local heat transfer, weld temperature, cooling rate, and final mechanical performance; low-conductivity or thermally favourable backing conditions tended to improve heat utilisation, while highly conductive support conditions increased the risk of under-heated weld roots or reduced flow stability (Mondal et al., 2024; Park et al., 2020; Verma et al., 2025).

The comparatively poor performance of the aluminium backing condition can be explained by excessive heat extraction from the weld zone. Because aluminium possesses the highest thermal conductivity among the three selected conditions, the heat generated by friction and deformation was more rapidly dissipated into the bottom, top, and side supports, narrowing the available process window for stable plasticisation. The findings' interpretation is fully consistent with this mechanism: under the aluminium condition, insufficient heat remained available for proper mixing, and the fracture surfaces showed tunnel defects, voids, featureless regions, and coarse dimples near the defect region.

Such behaviour corresponds closely to the literature on backing-plate effects, where rapid heat loss through highly conductive backing materials has been associated with insufficient root-side softening, unstable flow, and defect formation. Park et al. (2020), for example, reported that higher heat-loss backing conditions in micro-FSW promoted inferior joint formation compared with more thermally resistant conditions, while Verma et al. (2025) further showed that backing diffusivity directly affects thermal symmetry and flow behaviour in dissimilar aluminium μFSW.

The superiority of the fly-ash condition can be interpreted as the opposite thermal case. The fly-ash bed acted as a thermal insulator, restricting heat loss from the lower surface and thereby allowing a larger volume of softened material to remain available around the pin and beneath the shoulder. This would favour material transport from the advancing side to the retreating side and, more importantly, along the thickness direction, thereby improving void closure and weld continuity. The results explicitly link the higher fly-ash joint efficiency to sufficient heat being retained in the weld zone, very fine plasticisation, proper mixing, and a smooth, mirror-like, defect-free weld surface. Recent studies support this general interpretation. Mondal et al. (2024) showed that the backing plate condition altered the thermal cycle and thereby changed the resulting strength and microstructure in the friction stir-welded Al-Li alloy. Das et al. (2024) likewise demonstrated that thermal boundary conditions and cooling strategy in thick aluminium FSW influence joint strength and grain-size distribution across the weld thickness. Verma et al. (2025) further confirmed that strategic control of backing diffusivity can improve heat utilisation and velocity-field symmetry, leading to better mechanical response. Within this framework, the fly-ash bed in the present study can be understood as an effective insulating thermal boundary that reduced heat drainage and enhanced consolidation quality.

The Taguchi and ANOVA results also become more meaningful when viewed through this thermal-boundary perspective. Under the aluminium backing condition, welding speed was the dominant factor, whereas under mild steel and fly ash, rotational speed became dominant. This shift suggests that when heat loss is severe, residence time becomes the most critical issue because the tool must remain long enough at a given location to develop the plasticised volume needed for sound bonding. Once heat dissipation is moderated, as in mild steel and especially in fly ash, the process becomes more sensitive to the rate of heat generation and stirring action, which are more directly governed by rotational speed. Recent optimisation studies on AA6061 and related aluminium systems support this interpretation. Yacout et al. (2025) found that rotational speed and tool profile were among the most influential parameters for ultimate tensile strength in AA6061-T6 FSW, while Wahjudi et al. (2024) showed that a Taguchi-based framework could effectively link tool configuration to mechanical response and fracture characteristics in AA6061-T651 joints. These reports reinforce the conclusion that parameter significance in FSW is not fixed, but depends on the surrounding thermal and mechanical boundary conditions.

An important outcome of the present work is that hardness did not follow the same ranking as tensile strength. The aluminium condition produced the highest hardness, whereas the fly-ash condition produced hardness values close to the base metal, despite giving the best tensile performance. This difference is significant because it shows that the tensile response in the present joints was governed more strongly by consolidation quality and defect suppression than by hardness increase alone. This attributes the higher hardness in the aluminium condition to a quenching-like effect caused by rapid heat removal through the metallic support system, whereas in the fly-ash condition, the absence of strong heat extraction eliminated this quenching effect and produced a crown-to-root decrease in hardness. Recent literature supports the broader principle that thermal boundary conditions can substantially reshape hardness distributions by altering the cooling rate and local metallurgical response. Mondal et al. (2024) showed that backing condition changes the thermal cycle and therefore the resulting property balance in FSWed aluminium, while Das et al. (2024) reported that quenching and cooling rate strongly affect local mechanical response across the weld thickness.

In AA6061 specifically, Zhou et al. (2024) further demonstrated that thermal history influences precipitate evolution and joint efficiency after welding, confirming that hardness variation in 6xxx alloys is highly sensitive to heat-treatment-like effects. Even though the present material was pure aluminium, the same principle applies: hardness reflects local thermal history, whereas tensile strength in defective welds may be dominated by macroscopic integrity rather than local hardness alone.

The fractographic evidence strongly supports this distinction between hardness-controlled and defect-controlled behaviour. The base metal exhibited fine dimples with micro-void coalescence, consistent with ductile fracture. In the aluminium condition, however, the fracture surfaces contained tunnel defects, voids, featureless regions, and coarse dimples, indicating mixed-mode failure initiated or accelerated by poor consolidation. The mild-steel condition showed an intermediate response with fewer severe defect features, whereas the fly-ash condition displayed abundant, fine, and deep dimples and a fracture appearance close to that of the base metal. This progression from mixed-mode, defect-assisted fracture to a more uniformly ductile dimple rupture directly mirrors the progression in joint efficiency. Recent AA6061 studies similarly use fractography to interpret weld quality and failure mode. Wahjudi et al. (2024) linked fracture characteristics to tool-design-induced changes in mechanical response, while Yacout et al. (2025) showed that systematically optimised FSW conditions can produce defect-free joints with predictable hardness and strength behaviour. Accordingly, the fractography in the present work is not merely descriptive; it provides direct evidence that the fly-ash condition improved the actual integrity of the welded region rather than only modifying its hardness response.

The XRD observations provide an additional level of confidence in interpreting the fly-ash condition. Because fly ash was used as an unconventional insulating medium, a reasonable concern was whether particles from the bed might be mechanically introduced into the weld nugget. The XRD results showed no additional peaks, and the fly-ash welds exhibited the same peak positions as the other conditions, indicating that no detectable foreign material was introduced into the nugget zone.

This finding is important because it confirms that the beneficial effect of the fly-ash backing condition arose from thermal boundary control, not from chemical contamination or reinforcement. It also supports the practical attractiveness of the approach: the fly-ash bed functioned as a low-cost insulating process condition capable of improving joint efficiency without causing detectable phase contamination. Taken together, the present results indicate that backing condition should be treated as an active design variable in FSW parameter optimisation, particularly when the work is performed on conventional milling-based systems where process stability is more sensitive to fixture and heat-loss conditions than on dedicated industrial FSW platforms.

5. Conclusion

This study examined the friction stir welding of 6-mm pure aluminium under three different backing conditions, namely aluminium, mild steel, and fly ash, using a Taguchi L9 design to optimise the principal welding parameters. On the basis of the experimental results, the following conclusions can be drawn.

The developed fixture was effective for carrying out friction stir welding on a conventional vertical milling machine. It provided stable clamping, reduced setup difficulty, and allowed the welding trials to be performed under controlled and repeatable conditions. The backing condition had a pronounced influence on weld appearance, tensile behaviour, joint efficiency, hardness response, and fracture morphology. Among the three conditions studied, the fly-ash backing condition provided the most favourable overall weld performance.

The aluminium backing condition produced the lowest tensile performance, with tensile strength in the range of 93.20-113.41 MPa and joint efficiency in the range of 51.55-62.72%. The mild-steel backing condition improved joint performance compared with aluminium backing, producing tensile strength in the range of

72.43-139.10 MPa and joint efficiency in the range of 40.06-76.93%. The fly-ash backing condition gave the best overall performance, producing tensile strength in the range of 107.10-165.78 MPa and joint efficiency in the range of 59.23-91.69%.

The hardness profile did not follow the same ranking as tensile strength. The maximum hardness was observed in the aluminium condition, where hardness remained above the base-metal value, while the fly-ash condition produced hardness values closer to the base metal. The mild-steel condition showed intermediate hardness behaviour.

The fracture morphology strongly supported the tensile results. Welds produced in the fly-ash condition exhibited fracture surfaces similar to the base metal, with typical ductile fracture characterised by plenty of fine and deep dimples, whereas welds produced in the aluminium and mild-steel conditions showed mixed-mode fracture.

The XRD analysis showed that no foreign material was introduced during welding, including under the fly-ash backing condition. This confirms that the beneficial effect of the fly-ash condition arose from its thermal-insulation role rather than from any foreign-material incorporation into the weld zone.

Overall, the results show that backing condition is an important optimisation variable in friction stir welding of pure aluminium and that fly ash can serve as an effective low-cost insulating backing medium. Future work may extend this concept to aluminium alloys, different plate thicknesses, and closed-section products such as pipes and hollow profiles.

Data Availability

Data sets generated during the current study are available from the corresponding authors on reasonable request.

Declaration of Competing Interest

The authors declare that they have no known competing financial interests or personal relationships that could have appeared to influence the work reported in this paper.

Acknowledgements

The authors would like to acknowledge the Daou (Shaoxing) Technology Co., Ltd, Shaoxing City, Zhejiang Province, China, for providing the necessary facilities and resources for this research.

References

Abdelhady, S. S., Elbadawi, R. E., & Zoalfakar, S. H. (2024). Multi-objective optimization of FSW variables on joint properties of AA5754 aluminum alloy using Taguchi approach and grey relational analysis. *The International Journal of Advanced Manufacturing Technology*, *130*(9), 4235–4250.

Abdollahzadeh, A., Bagheri, B., Abassi, M., Kokabi, A. H., & Moghaddam, A. O. (2021). Comparison of the weldability of AA6061-T6 joint under different friction stir welding conditions. *Journal of Materials Engineering and Performance*, *30*(2), 1110–1127.

Acharya, U., Choudhury, S., Sethi, D., Akinlabi, E., & Roy, B. S. (2024). Enhancing joint performance in friction stir welding through tailored double-butt-lap geometry. *Welding in the World*, *68*(5), 1089–1101.

Ahmed, S., Rahman, R. A. ur, Awan, A., Ahmad, S., Akram, W., Amjad, M., Yahya, M. Y., & Rahimian Koloor, S. S. (2022).

Optimization of process parameters in friction stir welding of aluminum 5451 in marine applications. *Journal of Marine Science and Engineering*, *10*(10), 1539. https://doi.org/10.3390/jmse10101539

Al-Allaq, A. H., Maniscalco, J., Bhukya, S. N., Wu, Z., & Elmustafa, A. (2024). Parametric optimization of friction stir welding of AA6061-T6 samples using the copper donor stir-assisted material method. *Metals*, *14*(5), 536.

Ambrosio, D., Morisada, Y., Ushioda, K., & Fujii, H. (2024). Extremely thin intermetallic layer in dissimilar AA6061-T6 and mild steel friction stir lap welding using a hemispherical tool. *Scientific Reports*, *14*(1), 1718.

Amini, C., Jerez-Mesa, R., Travieso-Rodriguez, J. A., Mousavi, H., Lluma-Fuentes, J., Zandi, M. D., & Hassanifard, S. (2022). Ball burnishing of friction stir welded aluminum alloy 2024-T3: experimental and numerical studies. *Metals*, *12*(9), 1422.

Asmare, A., Al-Sabur, R., & Messele, E. (2020). Experimental investigation of friction stir welding on 6061-t6 aluminum alloy using taguchi-based gra. *Metals*, *10*(11), 1480.

Bharti, S., Kumar, S., Singh, I., Kumar, D., Bhurat, S. S., Abdullah, M. R., & Rahimian Koloor, S. S. (2023). A review of recent developments in friction stir welding for various industrial applications. *Journal of Marine Science and Engineering*, *12*(1), 71.

Choi, J.-W., Hino, R., Ushioda, K., Fujii, H., & Lee, S.-J. (2025). Critical Review of Solid-State Welding for Al Alloys with High Joint Efficiency: Friction Stir Welding (FSW) vs. Linear Friction Welding (LFW). *Metals and Materials International*, 1–25.

Clark, A., & Ragai, I. (2025). Adaptive Torque Control for Process Optimization in Friction Stir Welding of Aluminum 6061-T6 Using a Horizontal 5-Axis CNC Machine. *Journal Of Manufacturing And Materials Processing*, *9*(7), 232.

Das, H., Reza-E-Rabby, M., Whalen, S. A., Upadhyay, P., & Grant, G. J. (2024). Impact of backing plate and thermal boundary conditions for high-speed friction stir welding of 25-mm thick aluminum alloy 7175-T79. *International Journal of Precision Engineering and Manufacturing-Green Technology*, *11*(6), 1757–1767.

Feddal, I., Chairi, M., & Di Bella, G. (2025). Analysis of friction stir welding of aluminum alloys. *Metals*, *15*(5), 532.

Habba, M. I. A., & Ahmed, M. M. Z. (2025). Friction stir welding of dissimilar aluminum and copper alloys: A review of strategies for enhancing joint quality. *Journal of Advanced Joining Processes*, *11*, 100293.

Heidarzadeh, A., Mironov, S., Kaibyshev, R., Çam, G., Simar, A., Gerlich, A., Khodabakhshi, F., Mostafaei, A., Field, D. P., Robson, J. D., Deschamps, A., & Withers, P. J. (2021). Friction stir welding/processing of metals and alloys: A comprehensive review on microstructural evolution. *Progress in Materials Science*, *117*, 100752. https://doi.org/https://doi.org/10.1016/j.pmatsci.2020.100752

Isa, M. S. M., Moghadasi, K., Ariffin, M. A., Raja, S., bin Muhamad, M. R., Yusof, F., Jamaludin, M. F., bin Yusoff, N., & bin Ab Karim, M. S. (2021). Recent research progress in friction stir welding of aluminium and copper dissimilar joint: a review. *Journal of Materials Research and Technology*, *15*, 2735–2780.

Kubit, A., Trzepieciński, T., Kluz, R., Ochałek, K., & Slota, J. (2022). Multi-criteria optimisation of friction stir welding parameters for EN AW-2024-T3 aluminium alloy joints. *Materials*, *15*(15), 5428.

Lunetto, V., De Maddis, M., Lombardi, F., & Russo Spena, P. (2025). A review of friction stir welding of industrial alloys: tool design and process parameters. *Journal of Manufacturing and Materials Processing*, *9*(2), 36.

Manjunatha, C., N, S. T., V, M. S., Shivanayak, L., Panditharadhya, B. J., Prasad, C. D., Masum, H., Kumar, C. H., & Aden, A. A. (2025). Experimental investigation and optimization of friction stir welding parameters to manufacture AA6061-B4C composite material using design of experiments. *Journal of Materials Science: Materials in Engineering*, *20*(1), 117.

Mohd Jamil, M. Z., Mohd Isa, M. S., Raja, S., bin Muhamad, M. R., Yusof, F., Hasnan, H. K., Jamaludin, M. F., Brytan, Z., Liu, H., Suga, T., Morisada, Y., & Fujii, H. (2024). Friction Stir Alloying AZ61 Magnesium Alloy and Mild Steel with Zn-CNT Additive. *Transactions of the Indian Institute of Metals*, *77*(2), 435–443. https://doi.org/10.1007/s12666-023-03124-8

Mondal, B., Sinha, S., Reed, J., Lee, H.-S., Doherty, K. J., & Mishra, R. S. (2024). Effect of backing plate on microstructure and properties of friction stir welded 2195-O alloy. *Scripta Materialia*, *241*, 115899.

Myśliwiec, P., Kubit, A., & Szawara, P. (2024). Optimization of 2024-T3 aluminum alloy friction stir welding using random forest, XGBoost, and MLP machine learning techniques.
Materials, *17*(7), 1452.

Park, S., Joo, Y., & Kang, M. (2020). Effect of backing plate materials in micro-friction stir butt welding of dissimilar AA6061-T6 and AA5052-H32 aluminum alloys. *Metals*, *10*(7), 933.

Raja, S., Hasan, F., Ansari, A. H., & Ansari, H. (2016). *Effect of Friction Stir Welding on the Hardness of Al-6061 T6 aluminium alloy*.

Raja, S., Manikumar, R., Benruben, R., & Ragunathan, S. (2021). Effect of backing plate on strength and microstructural characteristics of friction stir welded AA2014-T6 aluminium alloy joints. *Materials Today: Proceedings*, *45*, 895–899.

Raja, S., Muhamad, M. R., Jamaludin, M. F., & Yusof, F. (2020). A review on nanomaterials reinforcement in friction stir welding. *Journal of Materials Research and Technology*, *9*(6), 16459–16487. https://doi.org/https://doi.org/10.1016/j.jmrt.2020.11.072

Raja, S., Muhamad, M. R., Yusof, F., Jamaludin, M. F., Suga, T., Liu, H., Morisada, Y., & Fujii, H. (2022). Friction stir alloying of AZ61 and mild steel with Al-CNT additive. *Science and Technology of Welding and Joining*, *27*(7), 533–540. https://doi.org/10.1080/13621718.2022.2080449

Raja, S., Yusof, F., Muhamad, M. R., Mohd Mansor, M. S., Juri, A., Wu, B., Jamaludin, M. F., Ansari, N., & Ren, J. (2024). Formation and influencing mechanism of the intermetallic compound in the friction stir welding of immiscible AZ31 and SPHC steel using aluminium powder as an additive. *Journal of Materials Research and Technology*, *30*, 9102–9114. https://doi.org/https://doi.org/10.1016/j.jmrt.2024.05.249

Soto-Diaz, R., Vasquez-Carbonell, M., & Escorcia-Gutierrez, J. (2025). A review of artificial intelligence techniques for optimizing friction stir welding processes and predicting mechanical properties. *Engineering Science and Technology, an International Journal*, *62*, 101949.

Tinguery, K. M. S., Rahem, A., Nadeau, F., & Fafard, M. (2023). Friction stir welding parameters development of AA6061-T6 extruded alloy using a bobbin tool. *Engineering Proceedings*, *43*(1), 50.

Tiwan, Ilman, M. N., Kusmono, & Sehono. (2023). Microstructure and mechanical performance of dissimilar friction stir spot welded AA2024-O/AA6061-T6 sheets: Effects of tool rotation speed and pin geometry. *International Journal of Lightweight Materials and Manufacture*, *6*(1), 1–14. https://doi.org/https://doi.org/10.1016/j.ijlmm.2022.07.004

Verma, M., Saha, P., & Singh, P. K. (2025). Optimizing heat utilization in dissimilar micro-friction stir welding of AA 2024-T3/AA 6061-T6 using dual backing plate: Impact on local microstructure, mechanical, and corrosion performance. *Journal of Manufacturing Processes*, *149*, 98–115.

Wahjudi, A., Pramono, A. S., & Batan, I. M. L. (2024). A study of concave shoulder angle on the mechanical properties and fractography of friction stir welded AA6061-T651 joints. *Journal of Materials Research and Technology*, *28*, 78–86.

Yacout, G. G., Shash, A. Y., Hegazi, H. A., & El-Sherbiny, M. G. (2025). Comparative experimental and statistical study of conventional and bobbin tool friction stir welding of AA6061-T6 aluminum alloy. *Journal of Engineering and Applied Scienc*e, 72(1), 255.

Yamani, S. M., Raja, S., bin Ariffin, M. A., Mohd Isa, M. S., Muhamad, M. R., Jamaludin, M. F., Yusof, F., & bin Ahmad Hairuddin, M. K. F. (2022). Effects of Preheating on Microstructural and Mechanical Properties of Friction Stir Welded Thin Low Carbon Steel Joints. *Journal of Engineering Materials and Technology,* 145(2). https://doi.org/10.1115/1.4055909

Zhou, D., Xia, Y., Gao, Z., Bai, L., & Hu, W. (2024). Effect of precipitate evolution on galvanic corrosion behavior of friction stir welded AA6061-T6 joint after post-weld aging. *Materials Today Communications,* 41, 110764.

IJAMMP

Cooperative Multi-Agent Scheduling to Improve Resource Utilisation in Large-Scale Manufacturing

Cheng Qian* and Yuchun Xu†

RESEARCH ARTICLE

ARTICLE INFO

Keywords:

Cooperative Game Theory;
Discrete Manufacturing;
Online Scheduling;
Resource Optimisation;
Sustainable Manufacturing

Article History

*Received:*24 October 2025
*Revised:*19 February 2026
*Accepted:*28 February 2026
Published:

ABSTRACT

Scheduling production in large-scale manufacturing is a complex challenge that requires dynamically allocating tasks to machines while balancing throughput and resource utilization. Game-theoretic approaches have been widely applied, with traditional models treating either all machines as players competing for tasks or all tasks competing for access to machines. Such formulations overlook the joint perspective of machines and tasks, often leading to schedule fragmentation, i.e. small, unusable gaps that severely reduce machine utilisation. This paper introduces a novel cooperative framework in which both machines and tasks act as players, negotiating directly to determine feasible start times when tasks are assigned to machines. Manufacturing systems are modelled as multi-agent networks, with a classifier selecting scheduling strategies based on the relative importance of machines and tasks. Machine importance is dynamically assessed using PageRank centrality, while task importance is determined by urgency and complexity. The negotiation process is formulated as a cooperative game that maximizes a collective utility function incorporating processing costs, penalties for early or late completion, importance of machines and tasks, and a new measure of opportunity loss caused by fragmented schedules. This cooperative game model can result a schedule with minimised gaps, thereby improving machine utilisation without compromising production speed. A discrete-event simulation was conducted to evaluate performance against a traditional multi-objective optimization approach. The findings indicated that 76% of machines identified as bottleneck resources demonstrated an average enhancement in utilisation of 1.5%, thus providing an effective solution for efficient and sustainable production management.

1. Introduction

Large-scale discrete manufacturing systems, which produce distinct items such as automobiles, aircraft or electronics through assembly and individualised processing steps, are characterised by complex product routings, diverse resources, and dynamic job arrivals. These systems present a substantial challenge for production scheduling. The core objective is the efficient real-time allocation of tasks to manufacturing machines, a problem central to operational efficiency. In this domain, two paramount yet often conflicting performance metrics are of particular significance: the maximisation of throughput (i.e. the minimisation of make-span) and the maximisation of machine utilisation (Veeramachaneni et al., 2025). The former is crucial for meeting delivery deadlines and reducing work in progress, while the latter is vital for spreading high capital costs over time and improving return on investment.

Smart and Sustainable Manufacturing Research Centre, Aston University, Birmingham, B4 7ET, United Kingdom

Corresponding authors: * c.qian4@aston.ac.uk, † y.xu16@aston.ac.uk

Conventionally, the most widely adopted approach to resolving these competing objectives is through the utilisation of centralised multi-objective optimisation techniques, including genetic algorithms and particle swarm optimisation (Wong & Ngan, 2013). These methods model the entire shop floor as a single entity, seeking a Pareto-optimal set of schedules that represent the best possible trade-offs. However, in dynamic and large-scale environments, this paradigm exhibits significant limitations. The computational complexity of these algorithms often renders them prohibitive for real-time, online scheduling (Megow et al., 2006), where online scheduling is the process of making immediate and dynamic decisions to assign tasks to resources as they arrive, without prior knowledge of future tasks. Moreover, their inherent reliance on a global, often static, snapshot of the system makes them vulnerable in the face of frequent disruptions, such as machine breakdowns or rush orders, necessitating computationally expensive rescheduling (Uhlmann & Frazzon, 2018).

An alternative approach is represented by decentralised, agent-based paradigms, which have gained traction for their flexibility and responsiveness (Barenji et al., 2017). The distribution of decision-making authority to individual

machine or task agents enables these systems to react swiftly to local changes (Zhang et al., 2016). Nevertheless, this very strength is a source of a critical weakness: a focus on local optima. When agents act in their own self-interest, for instance, a machine selecting the most immediately profitable task without considering global schedule health, the emergent global schedule can be highly inefficient. A particularly negative consequence of this inefficiency is schedule fragmentation, where the creation of small, non-utilisable time gaps between tasks on machine timelines leads to a significant degradation in overall utilisation. It is therefore evident that a significant research gap exists in this domain: i.e., the necessity for a decentralised scheduling methodology that retains the flexibility of multi-agent systems but is explicitly adapted to counteract local selfishness and the ensuing schedule fragmentation, thereby achieving a system-level balance between throughput and utilisation. The specific research questions are as follows:

(1) How can a cooperative game be formally modelled between machine and process of the task in a discrete manufacturing network to simultaneously address throughput and machine utilisation?

(2) How can metrics of network structural (e.g., PageRank centrality) be integrated into the utility functions to guide the negotiation process towards system-level efficiency?

The present paper addresses this gap by introducing a cooperative game-theoretic model for online resource allocation in manufacturing systems. Unlike conventional competitive game models, which typically frame scheduling as a contest among machines, the proposed approach enables direct negotiation between machines and tasks to determine processing start times.

By structuring these interactions as cooperative efforts aimed at maximising a joint utility function, which includes explicit costs for schedule fragmentation, the system moves towards globally efficient and robust schedules. To capture the dynamic importance of machines, a graph-theoretic importance metric based on PageRank centrality is used to inform the influence and the bargaining power of machines. Task importance, in turn, is derived from urgency and complexity, ensuring balanced prioritization. The practical effectiveness of this approach is demonstrated through a multi-agent discrete-event simulation, benchmarking it against a traditional multi-objective optimisation heuristic.

The remainder of this paper is structured as follows. Section 2 reviews relevant literature on manufacturing networks and the application of multi-objective optimisation in manufacturing systems. Section 3 introduces the methodology for online scheduling in large-scale discrete manufacturing systems with a strategy classifier. Section 4 details the problem formulation and the proposed cooperative game-theoretic model. Section 5 outlines the experimental setup and discusses the comparative results. Finally, Section 6 concludes with findings and prospective future research directions.

2. Literature Review

This section reviews the typical scheduling methods and analytical tools for discrete manufacturing systems.

2.1 Scheduling in Discrete Manufacturing Systems: Modelling, Solving, and the Game-Theoretic Methods

Scheduling in discrete manufacturing is a complex, typically NP-hard, problem that is central to operational efficiency (Allahverdi et al., 2018). The primary challenge is to optimise the allocation of resources and the sequencing of operations over time, with the objective of fulfilling a set of criteria, typically including the minimisation of make-span and the maximisation of machine utilisation. Traditional approaches have largely relied on centralised optimisation techniques. Metaheuristics, such as Simulate Annealing (Gaafar & Masoud, 2005), Genetic Algorithms (Zan et al., 2020) and Particle Swarm Optimisation (Sha & Lin, 2010), have been widely applied to find near-optimal solutions for these multi-objective problems (Zhang et al., 2025). Nevertheless, the computational demands of these approaches tend to restrict their practicality in online scheduling contexts, where the occurrence of dynamic events, such as the arrival of new tasks and machine breakdowns, requires frequent and efficient rescheduling (Marzia & Azab, 2023).

The limitations of centralised planning in dynamic contexts have stimulated interest in decentralised paradigms. Minguillon & Lanza (2019) studied the coupling of centralised and decentralised scheduling for the robustness in agile manufacturing systems. A number of agent-based mechanisms were also developed for production planning and scheduling (Jules & Saadat, 2016; Poudel et al., 2023). Among these, game theory has emerged as a promising framework for modelling the strategic interactions among distributed entities in a manufacturing system (Sanogo et al., 2025). Early applications often modelled scheduling as a competitive process. E.g., auction-based mechanisms have been explored where tasks bid for machines or machines bid for tasks, effectively treating the shop floor as a market. (Kang et al., 2020). Other non-cooperative models have analysed competition among tasks or among manufacturers (Liu et al., 2021; Hu et al., 2025). While these approaches offer enhanced flexibility, they can lead to system-wide inefficiencies, such as the creation of schedule fragmentation, as self-interested agents prioritise local gains over global performance. The potential of cooperative game theory to align local decisions with global objectives in manufacturing scheduling remains a less explored avenue compared to its competitive counterparts,

particularly for direct machine-process negotiation over the starting time of the process.

2.2 Multi-Agent Systems and Importance Measures in Discrete Manufacturing Systems

Multi-Agent Systems (MAS) provide a natural architectural blueprint for implementing decentralised manufacturing control (Lee & Kim, 2008). In MAS, autonomous agents interactively collaborate to solve a variety of problems, which exceed their individual capabilities. These agents can be viewed as representations of physical resources, including machines, and logical entities, such as orders (Zhang et al., 2016). This paradigm facilitates collaborative and self-organising behaviour, moving beyond a rigid, centralised control structure (Zheng et al., 2021). Agents can react locally to disruptions (Bi et al., 2024), and negotiate to find feasible schedules (Poudel et al., 2023), leading to increased robustness and adaptability (Leitão, 2009).

The structure of interactions in such a discrete manufacturing system inherently forms a network. In light of this realisation, researchers have commenced an analysis of manufacturing systems through the theoretical framework of network science (Li et al., 2017; Yang et al., 2021). This perspective facilitates the quantification of structural properties and the identification of critical nodes that influence overall system performance. By employing various network centrality metrics, such as betweenness centrality (Xin et al., 2019) and eigenvector centrality (Zeng et al., 2024), the importance of machine nodes within different operational scenarios of manufacturing systems can be quantitatively assessed. Metrics like PageRank, originally developed for web search, can also be adapted to rank machines (Zhang et al., 2017) or processes (Zhu et al., 2023) based on their connectivity and importance within the production network. This provides a data-driven, dynamic measurement of a machine's systemic influence, representing a significant advancement over static, pre-defined priorities.

Although MAS and game theory offer frameworks for decentralised scheduling, current game-theoretic models are essentially competitive, which may result in schedule fragmentation and reduced overall efficiency. Furthermore, while network science provides tools to analyse manufacturing systems structurally, its integration into the operational decision-making of production scheduling is limited. Consequently, a novel approach is required that integrates a cooperative game-theoretic model for direct task-machine negotiation with a network-science-informed perspective, using metrics such as PageRank to explicitly guide agents towards decisions that mitigate fragmentation and balance throughput with utilisation.

3. A Flexible Strategy Classifier for Online Scheduling

This section designs a flexible classifier for machine-process matching strategies, engineered to meet the demand for efficient, high-utilisation resource allocation solutions across diverse production scenarios.

3.1 The Conventional Online Scheduling Methods

Since the processes of tasks may arrive at the manufacturing network at any arbitrary future moment, the resource allocation process for each new task constitutes an online scheduling problem. A "capability-availability-efficiency" filtering principle is typically employed in this regard (Qian et al., 2019). Specifically, a process, based on its processing requirements, first filters a set of candidate machines possessing the specified processing capabilities. Subsequently, the process initiates query requests to these machines to gather their available time slots. Finally, a multi-objective optimisation algorithm is employed to identify the machine and time slot that best satisfy the processing objectives, thereby completing the matching process. In this procedure, the newly arrived task process should explicitly select a specific processing time slot from a range of available slots on the candidate machines. The selection of algorithm has a direct impact on the generated schedule, yielding various solutions with distinct levels of machine utilisation and task completion times. The flexible classifier proposed in Section 3.3 is capable of adapting a machine-process matching strategy based on the specific context, thereby achieving an effective balance between the utilisation of machines and the efficiency of production in the manufacturing network.

3.2 Defining the Importance of Machines and Processes

The selection of a matching strategy is fundamentally influenced by two parameters: the importance of the machine and the task. These are formally defined as the Machine Importance ($\boldsymbol{I}_{\mathrm{m}}$) and the Process Importance ($\boldsymbol{I}_{\mathrm{p}}$), respectively.

Equation (1) defines the importance of a machine i within the manufacturing network. This is calculated as the PageRank centrality value $\boldsymbol{PR}_{\mathrm{i}}$ of the node $\boldsymbol{i}$ within a directed machine cooperation network $\boldsymbol{CopNet}_N$, which is constructed from the most recent $\boldsymbol{N}$ upstream-to-downstream process relationships.

$$I_{\mathrm{m}}(i) = PR_i(CopNet_N) \tag{1}$$

The PageRank value of a node is a metric of node importance computed via a random walk algorithm. Conceptually, it defines the importance of a node as the probability of it being visited during a random traversal of the directed network. During this random walk, the probability of transitioning from one node to another, along a directed edge, is distributed proportionally to the weights of the outgoing edges. This random walk process can be modelled as a first-order Markov chain, and the components of its stationary distribution, PR_i, yield the PageRank values for the network nodes.

The importance of a process j belonging to task i is defined in (2), where *Priority* corresponds to the process priority defined subsequently in (3).

$$I_p(i_j) = Priority(i_j)$$

$$Priority = w_1 P_u^{norm} + w_2 P_s^{norm} + w_3 P_r^{norm}$$

The process priority is typically a composite measure, integrating factors such as the process's urgency (P_u), its static priority (P_s), and its process planning priority (P_r). This ensures that urgent tasks are commenced preferentially over routine ones (Qian et al., 2020). In contexts involving multiple processes, the urgency of the process P_u is determined by the proximity of the delivery deadline. Meanwhile, the static priority P_s is inherent to the process route itself. The process is assigned a higher P_s to those with more subsequent processes, calculated as the total processing time of all its descendant processes in the production route. This metric reflects the potential scale of disruption the current process could cause to subsequent stages. The planning priority stems from typical process planning knowledge. E.g., a common principle is "Shortest Job First", where processes with shorter processing times are assigned higher priority. This approach reduces the average waiting time, thereby preventing a backlog of short-duration processes from accumulating behind longer ones.

Synthesising these influencing factors, the process priority is given by (3), where P_u^{norm}, P_s^{norm}, and P_r^{norm} represent the normalised urgency, static priority, and planning priority, respectively. The coefficients w_i are weighting factors that sum to unity, i.e. $\sum w_i = 1$.

As a general guideline, w_1 should be appropriately increased in scenarios with strict delivery deadlines or tight schedules. For production systems with inherently long average process routes, a larger w_2 can help mitigate the cumulative effect of anomalies or delays. In situations where most process times are similar except for a few outliers with significantly longer durations, increasing can reduce the average process waiting time.

3.3. A Flexible Classifier for Machine-Process Matching Strategies

From the definitions above, the Machine Importance I_m reflects the current degree to which a machine is "needed" within the manufacturing network. A higher I_m indicates that the machine receives a relatively larger number of processing requests and holds greater importance for completing the recent tasks. Besides, the Process Importance I_p embodies the current "desire level" for machine capacity possessed by the process. A higher I_p signifies greater importance and urgency of the process, implying a larger impact on fulfilling customer demands. Based on the respective values of Machine Importance I_m and Process Importance I_p , this section establishes a flexible classifier for machine-process matching strategies, as listed below.

When a high-importance process selects a low-importance machine, the classifier adopts a "Process Dominated Strategy". This strategy prioritises maximising the fulfilment of the process's production requirements. The process can claim any available time slot on the machine, ensuring its demands are met as a primary objective.

Conversely, when a low-importance process selects a high-importance machine, the classifier implements a "Machine Dominated Strategy". This strategy focuses on optimising the resource utilisation of the critical machine. The process's production plan is scheduled to maximise the machine's usage rate, deliberately avoiding the creation of small, unusable time fragments between tasks that could degrade overall efficiency and waste the processing capacity of a high-value asset.

The aforementioned strategies can be realised by implementing different objective functions emphasising the machine utilisation or the completion time of process when scheduling. In all other cases, the classifier facilitates a "Cooperative Game Strategy" between the machine and the process. Based on their relative importance values, this strategy determines a suitable start time aimed at maximising the combined utility for both the process and the machine. The specific mechanics of this cooperative game process are detailed in Section 4.

4. The Cooperative Game Model for Machine-Process Scheduling

This section formalises the matching problem within a manufacturing network as a cooperative game between two primary players: a process and a machine. The core of their interaction is a negotiation concerning the process's start time on the machine.

4.1. Modelling the Time Slots of Machines

For a given machine m, its current available time slots are represented by a set of open intervals, as denoted in (4). Each interval is bounded by the completion time (TL) of the preceding process and the planned start time (TN) of the subsequent process on the machine. When a task ($Order$) searches the network for an available machine for its process p, a machine is included in the candidate set if any of its available slots meets the duration requirement $T_{order(p)}$ specified in (5).

$$AvailSlot_m = \{(TL_1, TN_1), (TL_2, TN_2), \dots, (TL_n, TN_n)\} \quad (4)$$

$$TN_i - TL_i \geq T_{Order(p)},\ i = 1,2,\dots,n \quad (5)$$

The practical feasibility of a time slot also depends on the lead time required for preparatory work, such as logistics and setup of tools. Depending on whether the time between the current moment t and the slot's start TL_i is sufficient (denoted by state ξ_S) or insufficient (ξ_I) for these preparations, the actual, usable time slot $ActSlot_m$ available to the process is determined by (6). This calculation incorporates the process's latest start time $T_{LS(p)}$, the completion time of its predecessor $T_{Finish(p-1)}$, and the required logistical lead time $T_{log(p-1,p)}$.

$$ActSlot_m = \begin{cases} ((T_{\text{Finish}(p-1)} + T_{\log(p-1,p)}), \min(TN_i - T_{Order(p)}, T_{\text{LS}(p)})), & \xi_I \\ (TL_i, \min(TN_i - T_{Order(p)}, T_{\text{LS}(p)})) & , \xi_S \end{cases} \quad (6)$$

4.2. The Utility Functions for Machines and Processes

Based on the process's assigned weights for production time, cost, and quality, it determines its ideal start time $T_{Start(p)}$ within $ActSlot_m$ to meet its punctuality requirements and minimise inventory costs. On the other hand, the ideal start time for an incoming process, from the machine's perspective, is either at the very beginning of the available slot (TL_i) or at a point sufficiently close to its end (TN_i) to avoid partitioning the available time into short, unusable fragments that cannot accommodate other process. To achieve this objective, a floating pricing strategy is employed by machines as defined in (7) - (9). Here, $StdCost$ is the standard price per unit time for the machine, t_p is the start time determined through the game, and the average processing time $avgProcLen$ is estimated from the machine's recent processing history.

$$Cost_{Order(p)} = \begin{cases} StdCost \cdot T_{Order(p)}, & \Delta t \geq ProcLen \\ StdCost \cdot (T_{Order(p)} + \Delta t), & \text{Otherwise} \end{cases} \quad (7)$$

$$\Delta t = t_p - TL_i \quad (8)$$

$$ProcLen = \min(T_{Order(p)}, avgProcLen) \quad (9)$$

The process's utility function $P_{Order(p)}$ in the game is defined by (10) and (11). It represents the product's value minus processing costs and any additional costs arising from early or late production, such as inventory holding costs or penalties for late delivery. t_p denotes the process start time following the game, $T_{LS(p)}$ represents the latest start time for process p (i.e., the endpoint of interval $ActSlot_m$), W_p signifies the storage cost per unit time for this process, and Pen_p indicates the delay penalty rate for this process.

$$P_{Order(p)} = Value_{Order(p)} - Cost_{Order(p)} - Aux_{Order(p)} \quad (10)$$

$$Aux_{Order(p)} = \begin{cases} W_p(T_{\text{Start}(p)} - t_p) & , t_p < T_{\text{Start}(p)} \\ 0 & , T_{\text{Start}(p)} \leq t_p \leq T_{\text{LS}(p)} \\ Pen_p(t_p - T_{\text{LS}(p)}) & , t_p > T_{\text{LS}(p)} \end{cases} \quad (11)$$

The machine's utility function P_m is defined by (12), which represents the revenue from the processing cost, minus an opportunity loss $Opploss_{Order(p)}$ incurred if the scheduled process creates a small, unusable time fragment. This loss quantifies the potential revenue foregone from other tasks that could have used that fragment. It reflects a system-wide perspective. The quantifiable opportunity loss is defined by (13) and (14). It models the scenario where a new process arrives during the newly created fragment $\Delta Slot$, and that new process selects this specific machine as a candidate. The probability of this event is a function of the probability of at least one new process arriving during $\Delta Slot$ (denoted as $Prob_{arr}$) and the probability that a random walk visits machine m at least once during that period (denoted as $Prob_{RW}$). This is scaled by the ratio of the expected importance of a newly arrived process to the importance of the current process.

$$P_m = Cost_{Order(p)} - Opploss_{Order(p)} \quad (12)$$

$$Opploss_{Order(p)} = Prob_{\text{arr}} Prob_{\text{RW}} \frac{E(I_p')}{I_p(Order(p))} Cost_{Order(p)} \quad (13)$$

$$\Delta Slot = TN_i - TL_i - T_{Order(p)} \quad (14)$$

The arrival of new processes at a machine is modelled as a Poisson process, characterised by a constant average arrival rate. Consequently, the number of processes arriving before time t follows a Poisson distribution with parameter , as shown in (15). The probability is then derived from the Poisson probability mass function, given by (16) and (17).

$$N(t) \sim Poiss(\lambda_a t) \quad (15)$$

$$Poiss(X = 0) = e^{-\lambda_a \Delta Slot} \quad (16)$$

$$Prob_{\text{arr}} = Poiss(X \geq 1) = 1 - e^{-\lambda_a \Delta Slot} \quad (17)$$

The probability $Prob_{RW}$ is determined by the structure of the directed cooperation network $CopNet_N$. As defined by the PageRank algorithms, the one-step transition probability from node *i* to node *j* is given by (18), where A_{ij} denotes the element of the adjacency matrix containing the edge weight, and *K* represents the out-degree of node *i*. The probability of the random walk visiting node *m* at least once during the *times* number of steps within Δ*Slot* is calculated by (19) to (21). Here, *times* is the number of processing slots that can theoretically fit into the fragment. *{m}* represents all machine nodes in the network. $I_m(a)$ denotes the importance, or the PageRank value of machine *a*. The function ceil() performs rounding upwards.

$$Prob_m(X=1) = I_{\mathrm{m}}(m) + \sum_{a\in\{\mathrm{m}\}} I_{\mathrm{m}}(a)\, P_{\mathrm{Trans}}(a,m) \tag{19}$$

$$times = \mathrm{ceil}\left(\frac{\Delta Slot}{avgProcLen}\right) \tag{20}$$

$$\begin{aligned} Prob_{\mathrm{RW}} &= 1 - [1 - Prob_m(X=1)]^{times} \\ &= 1 - [1 - I_{\mathrm{m}}(m) - \textstyle\sum_{a\in\{\mathrm{m}\}} I_{\mathrm{m}}(a)\, P_{\mathrm{Trans}}(a,m)]^{\mathrm{ceil}\left(\frac{\Delta Slot}{avgProcLen}\right)} \end{aligned} \tag{21}$$

With all components of the machine's utility function in (12) defined, the overall payoff for the cooperative game can be obtained in 4.3.

4.3. The Cooperative Game Model between Machines and Processes

The players in this game are the machine and the process of the task. The process start time t_p constitutes the various strategies employed, thereby rendering it a continuous variable game. The overall payoff for the cooperative game is formulated as the sum of the utilities of the machine and the process, resulting in (22). Note that the production value $Value_{Order(p)}$ is a constant for a given process-machine pair and thus does not affect the optimisation. When a dominant strategy exists within the decision space (i.e., a strategy optimal for all participants), this solution is selected as the outcome of the game. Otherwise, the Nash equilibrium point of the game is sought: a state where all participants' current strategies are optimal, and no single participant can unilaterally alter their strategy to increase the payoff. The Nash equilibrium solution for this game can be found by solving the constrained optimisation problem specified by (23) and (24), which seeks to maximise the overall payoff within the feasible time slot $ActSlot_m$.

$$Payoff = -Aux_{Order(p)} - Prob_{\mathrm{arr}} Prob_{\mathrm{RW}} \frac{E(I_p^t)}{I_{\mathrm{p}}(Order(p))} Cost_{Order(p)} \tag{22}$$

$$\text{minimise} \quad y = -Payoff(t_p) \tag{23}$$

$$\text{subject to} \quad t_p \in ActSlot_m \tag{24}$$

The single-variable optimisation problem itself is not complex, and numerous algorithms can be employed to solve it. The BFGS algorithm with the time complexity of $O(n^2)$ is adopted, which applies a Newton-like method approximating the Hessian matrix of the objective function (Dai, 2013). The solved t_p represents the start time of processing determined following the cooperative game between the machine and the process. When multiple Nash equilibrium points exist in the game problem, selecting a smaller start time may allow for greater tolerance in subsequent processing stages.

5. NUMERICAL EXPERIMENT

To validate the efficacy of the proposed machine-process cooperative game model, this section conducts a comparative analysis of resource allocation within a manufacturing network. We compared two approaches: a conventional method as described in Section 3.1, and a new method where machines and processes negotiate start times through our cooperative game model.

5.1. Experiment Setup

A numerical simulation was constructed using a scenario comprising 50 virtual machines and 500 virtual manufacturing tasks. The machine fleet consists of 10 lathes, 6 milling machines, 5 planing machines, 4 grinding machines, 10 drilling machines, 7 polishing machines, and 8 3D printers. Each machine is defined by a set of specific parameters, including its operable dimensional range, processing accuracy, spatial coordinates, and distinct processing speed, which correlates with a corresponding usage cost per unit time. The detailed parameters for the machine fleet are provided in Table 1.

To ensure a realistic testbed for resource matching, the numerical experiment utilises a set of common process routes and process combinations, denoted as *routeSet* in (25). The formulation of this set is consistent with established international and national standards, including ISO 14649, the Chinese standard GB/T 4863-2008, the German standard series DIN 8580 ff, alongside exemplary industrial processes. The digits 0 to 6 in *routeSet* represent lathes, milling, planing, grinding, polishing, drilling machines, and 3D printers, respectively.

$$\begin{aligned} routeSet = \{&(0,1,3,4),(2,1,3,4),(2,3,4),(2,0,3,4),(0,1,2,3),(3,4,6),\\ &(0,1,3,4,6),(6,0,1,3,4),(0,2,1,3,4),(1,4),(2,0,1,3),(5,6),(5,4),(6,0,1),(2,6,0),\\ &(0,1,4),(0,1),(0,0),(1,1),(2,1),(0,6),(3,4),(0,3),(3,6),(0,1),(5,6),(0,0),\\ &(0,1,3,4),(6,0,1),(0,0),(2,3),(0,6),(0,1,3),(0,1),(5,6),(5,6)\} \end{aligned} \tag{25}$$

Table 1: Parameters for the machine fleet in the experiments.

ID	Type	Machinable dimensions		Machining precision	Machine position		Unit cost	Processing speed
		Axial / X	Radial / Y		X	Y		
1	Lathe	1200	350	10	118.4	29.6	22	1
2	Lathe	1200	350	12	122.2	32.1	12	0.9
3	Lathe	2000	400	7	121	32.4	18	1.1
4	Lathe	2000	400	12	119.4	30.7	12	0.9
5	Lathe	2000	400	7	121.2	29.8	18	1.1
6	Lathe	2000	400	10	121.1	30.9	22	1
7	Lathe	2000	400	7	122.2	30.6	18	1.1
8	Lathe	2000	400	10	119.3	31.9	22	1
9	Lathe	2000	400	12	120.7	31.5	12	0.9
10	Lathe	2000	400	7	119.3	30.3	18	1.1
11	Milling	250	650	8	121	29.2	25	1
12	Milling	200	700	8	120.4	29.7	25	1
13	Milling	360	900	7	121.4	29.8	32	1.06
14	Milling	400	1200	8	120.7	30.5	25	1
15	Milling	360	900	11	122	32.3	18	0.9
16	Milling	360	900	11	121.8	30.4	18	0.9
17	Planing	640	320	8	120.3	32.6	18	1.05
18	Planing	640	320	8	118.6	30.3	18	1.05
19	Planing	800	450	11	120.8	30.4	15	1
20	Planing	1000	500	10	121.6	29.2	23	1
21	Planing	800	450	10	121.1	30.3	23	1
22	Grinding	320	152	8	122.5	30.4	16	1
23	Grinding	320	152	8	120.7	32	16	1
24	Grinding	500	260	8	121.9	28.6	25	1
25	Grinding	1000	320	6	122.5	29.8	29	1.08
26	Polishing	200	80	4	120.9	31.8	15	1
27	Polishing	200	80	4	118.9	28.5	15	1
28	Polishing	200	80	1	121.9	31.7	30	1.1
29	Polishing	450	250	4	119.8	32.3	18	1
30	Polishing	610	180	4	122.1	32.1	15	1
31	Polishing	610	180	4	121.9	32.6	15	1
32	Polishing	610	180	1	119.9	29.5	30	1.1
33	3D Printing	320	320	10	120.2	29.9	16	1
34	3D Printing	320	320	10	119.7	32.2	22	0.95
35	3D Printing	165	380	8	118	29.6	42	1.08
36	3D Printing	165	380	10	119.2	30.7	22	0.95
37	3D Printing	350	350	10	119.4	32.6	22	0.95
38	3D Printing	165	380	10	120.5	28.8	16	1
39	3D Printing	320	320	8	119.3	30.5	42	1.08
40	3D Printing	650	600	10	120.2	29.6	16	1
41	Drilling	440	6	13	118.5	31.9	20	1
42	Drilling	68	3	13	119.7	29.4	20	1
43	Drilling	440	6	10	118.8	29.9	45	1.2
44	Drilling	440	6	10	120.3	31	45	1.2
45	Drilling	440	6	13	118.8	31.4	20	1
46	Drilling	293	6	10	122	31.8	45	1.2
47	Drilling	68	3	13	122	29	20	1
48	Drilling	68	3	13	120.3	31.7	26	0.9
49	Drilling	293	6	10	119.2	32.1	45	1.2
50	Drilling	293	6	10	122.1	30.6	45	1.2

To ensure a realistic testbed for resource matching, the numerical experiment utilises a set of common process routes and process combinations, denoted as *routeSet* in (25). The formulation of this set is consistent with established international and national standards, including ISO 14649, the Chinese standard GB/T 4863-2008, the German standard series DIN 8580 ff, alongside exemplary industrial processes. The digits 0 to 6 in *routeSet* represent lathes, milling, planing, grinding, polishing, drilling machines, and 3D printers, respectively.

$$routeSet = \{(0,1,3,4), (2,1,3,4), (2,3,4), (2,0,3,4), (0,1,2,3), (3,4,6), (0,1,3,4,6), (6,0,1,3,4), (0,2,1,3,4), (1,4), (2,0,1,3), (5,6), (5,4), (6,0,1), (2,6,0), (0,1,4), (0,1), (0,0), (1,1), (2,1), (0,6), (3,4), (0,3), (3,6), (0,1), (5,6), (0,0), (0,1,3,4), (6,0,1), (0,0), (2,3), (0,6), (0,1,3), (0,1), (5,6), (5,6)\} \quad (25)$$

The 500 virtual manufacturing tasks were generated by randomly selecting a process route from the *routeSet* for each task. For each process within a route, specific requirements for parameters such as processing dimensions and accuracy were randomly generated, thereby defining the virtual production tasks. A key logical constraint was enforced during generation, i.e., for any process sequence, the workpiece dimensions required by a subsequent process must not exceed those of its predecessor (with exceptions made for 3D printing), and the specified accuracy must not degrade throughout the process.

Each manufacturing task is also characterised by additional attributes, including the time they are received by manufacturing systems, locations for raw material and delivery, delivery due time, standard processing time, and its specific weights for production time, cost, and quality. Weightings were assigned randomly. The time weighting was used to determine the allowable slack time for each process, which was then combined with estimated logistics duration to calculate the final delivery due date for the task. The 500 independent tasks generated for the experiment comprise a total of 1,326 individual processes. A selection of the generated process parameters is detailed in Table 2, where the six-tuple series in the “Processes” column denotes the sequence of processes, machining methods, machining dimensions (x, y), precision requirements, and the standard process durations.

5.2. The Comparative Experiment on Machine-Process Pairing with Different Strategies

The first process of each task arrives at the manufacturing network at its pre-defined release time. Subsequent processes initiate their resource requests upon the completion of their immediate predecessors. A comparative experiment is designed as follows.The control group employs the "capability-availability-efficiency" filtering mechanism described in Section 3.1,

Table 2: Details of tasks and processes in the experiments (Excerpt)

Task ID	Task arrival time	Raw material location (x, y)	Delivery location (x, y)	Delivery due time	Processes
0	18	(118.9, 30.3)	(119.1, 29.8)	412	(0, ‘Lathe’, 623, 281, 14, 171) (1, ‘Milling’, 604, 137, 11, 126)
1	26	(122.0, 29.5)	(120.2, 31.5)	296	(0, ‘Lathe’, 873, 114, 13, 139) (1, ‘Lathe’, 450, 87, 13, 86)
2	175	(122.0, 29.5)	(121.9, 31.2)	986	(0, ‘Planing’, 191, 212, 15, 159) (1, ‘Lathe’, 116, 189, 12, 94) (2, ‘Milling’, 56, 183, 12, 63) (3, ‘Polishing’, 55, 110, 5, 313)
3	112	(120.2, 29.3)	(118.0, 29.4)	387	(0, ‘Drilling’, 168, 4, 14, 32) (1, ‘Lathe’, 725, 299, 11, 79) (2, ‘Milling’, 666, 111, 11, 116)
4	11	(121.1, 30.5)	(122.0, 29.0)	1072	(0, ‘Lathe’, 823, 326, 13, 93) (1, ‘Planing’, 547, 78, 13, 167) (2, ‘Milling’, 252, 59, 12, 173) (3, ‘Milling’, 74, 52, 11, 113) (4, ‘Polishing’, 60, 51, 5, 193)
5	2	(122.0, 29.5)	(119.3, 30.5)	850	(0, ‘Milling’, 400, 327, 14, 123) (1, ‘Polishing’, 366, 122, 3, 356) (2, ‘Drilling’, 44, 3, 12, 26)
…	…	…	…	…	…
499	1752	(121.1, 30.5)	(120.7, 29.8)	916	(0, '3D Printing', 135, 268, 9, 714) (1, ‘Drilling’, 13, 4, 10, 26)

where the process autonomously selects its start time without considering the possible fragments caused at the machine timeline. In contrast, the experimental group implements the proposed game theoretic model, i.e., after filtering for machines of the available type, the process engages in a cooperative game process with each candidate machine over its available time slots to determine a mutually suitable start time. The importance of machine and the priority of processes are calculated dynamically based on $CopNet_{500}$, which denotes the collaborative network formed by up to 500 processes that have commenced recently. the storage cost per unit time W_p is defined as 1, while delay penalty rate Pen_p=15.

The experimental validation was conducted through a discrete-event simulation tool developed in Python. As the simulation time advanced from 0 to 10,000 time units, the 500 predefined manufacturing tasks were released into the system at their specified initiation times. The multi-agent system facilitated online scheduling, wherein the Technique for Order Preference by Similarity to Ideal Solution was employed by the agents to evaluate and rank candidate machines during the initial filtering phase based on the "capability-availability-efficiency" principle (Qian et al., 2019). During the simulation run, the *networkx* library in Python was utilised to dynamically compute the PageRank values for all machines within the evolving cooperation network $CopNet_{500}$. Key parameters for the game model (e.g., the Machine Importance I_m, the average operation duration per machine *avgProcLen*, and the process arrival rate λ_a) were updated in real-time, ensuring the model's responsiveness to the current network conditions. The simulation for both the control and experimental groups was conducted under identical task loads, parameters and machine properties, with different scheduling mechanisms incorporating either the game theory model or not. For the experimental group, once a set of candidate machines and their available slots were identified for a process, the cooperative game model was invoked. The negotiation to determine the optimal start time t_p was formulated as an optimisation problem, which was solved using the *scipy.optimize* module for Python to find the Nash equilibrium solution that maximised the joint payoff function. The weights to calculate the priority of process were defined as (w_1,w_2,w_3)=(0.3,0.45,0.25) in this experiment.

Fig. 1(a) illustrates the utilisation rate of each machine observed in both experimental runs. The machines are sorted along the horizontal axis in descending order of their utilisation rate in Fig. 1(b). The vertical axis represents the corresponding utilisation rate of each machine.

The average utilisation rate of all machines has barely changed for both the control and experimental groups, at 37.3% and 37.5%, respectively.

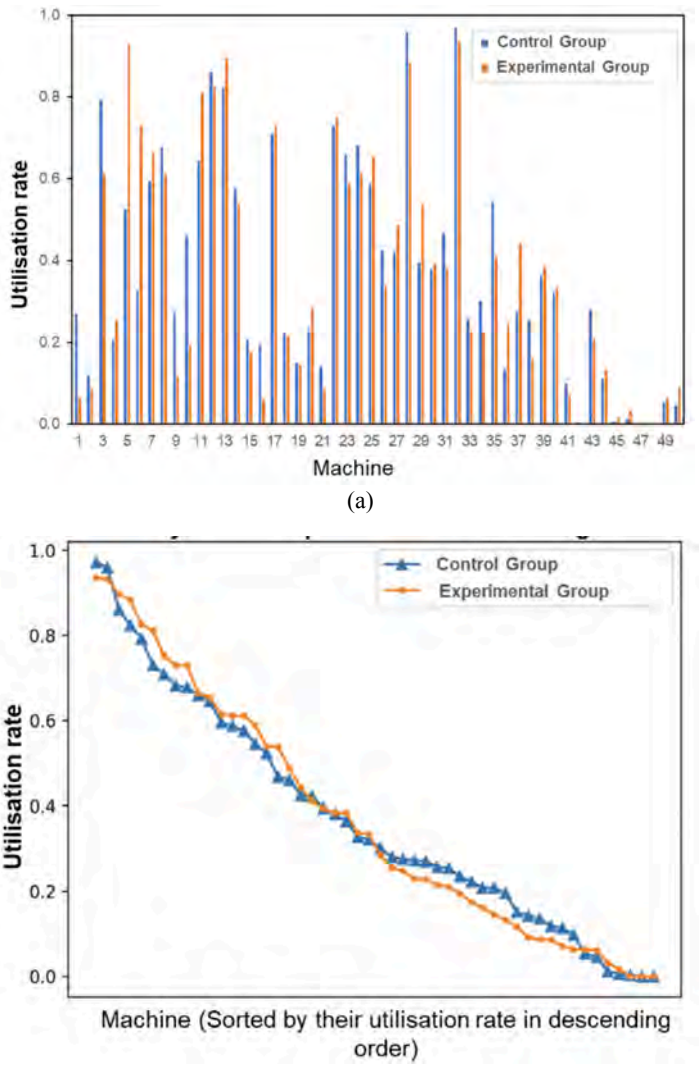

Figure. 1: The utilisation rate of machines in the comparative experiments showing a) Utilisation rate of machines in the comparative experiments, and b) Utilisation rate of machines sorted by their occupied times

However, Fig. 1(b) shows that, for machines with initially high utilisation rate (indicating bottleneck resources), applying the cooperative game model generally led to an increase in utilisation. Among the 25 machines with initial utilisation rates above the average, 19 showed improved utilisation, with an average increase of 1.5%. This localised improvement occurred while the overall average utilisation rate across the entire manufacturing network remained virtually unchanged. Fig. 1 demonstrated that the new method specifically boosts the utilisation of bottleneck resources, while maintaining the overall production pace and stability of the system. It indicated a redistribution of workload that enhances the throughput of critical machines without negatively overloading the system. Furthermore, all 1,326 processes were scheduled and processed successfully within the observed time horizon, confirming that the integration of the game model did not introduce detrimental delays or disrupt the overall production flow, thereby ensuring the stability of production management.

To assess the robustness of the experimental findings, a sensitivity analysis was conducted. Three additional sets of experiments were performed, each modifying a key parameter from the base case:

- Sensitivity test (a): The random seed was altered to generate a new set of 500 distinct manufacturing tasks.
- Sensitivity test (b): The inventory holding cost rate, i.e. in (11), was substantially increased to a new value of 10.
- Sensitivity test (c): The weighting parameters within the process priority calculation in (3) were modified as (w_1,w_2,w_3)=(0.6,0.25,0.15), to reflect a different decision-making bias.

As shown in Fig.2, the results from all three sensitivity tests consistently demonstrated the same characteristic outcome observed in the initial experimental group. Specifically, the cooperative game model continued to facilitate a further increase in the duty cycle of identified bottleneck resources compared to the baseline scheduling mechanism. This recurring pattern, observed under varying conditions of task load, cost structure, and priority calibration, strengthens the assertion that the proposed model possesses a robust capability to enhance the utilisation of critical system resources without compromising overall scheduling feasibility.

6. CONCLUSIONS

This paper addressed the complex challenge of allocating resources online in large-scale discrete manufacturing systems, where high throughput and high machine utilisation are conflicting objectives that require balancing. The study successfully addressed its core research questions. Firstly, it demonstrated how a cooperative game can be formally modelled between machine and process agents. The model establishes a framework for direct negotiation over processes' start times by defining specific utility functions that incorporate processing costs, earliness/tardiness penalties, and a novel opportunity loss cost for time fragmentation. Resolving this game to its Nash equilibrium yields schedules that balance the interests of both parties while addressing throughput and utilisation simultaneously. Secondly, this paper detailed how network science metrics, specifically PageRank centrality, can be integrated into the negotiation process among manufacturing resources. The dynamic importance of machines is a key parameter in quantifying the opportunity loss associated with schedule fragmentation. This integration provides a data-driven, systemic perspective that guides locally negotiating agents towards decisions that enhance global efficiency. Comparative experimental results have validated the model's practical efficacy in achieving a superior balance between throughput and

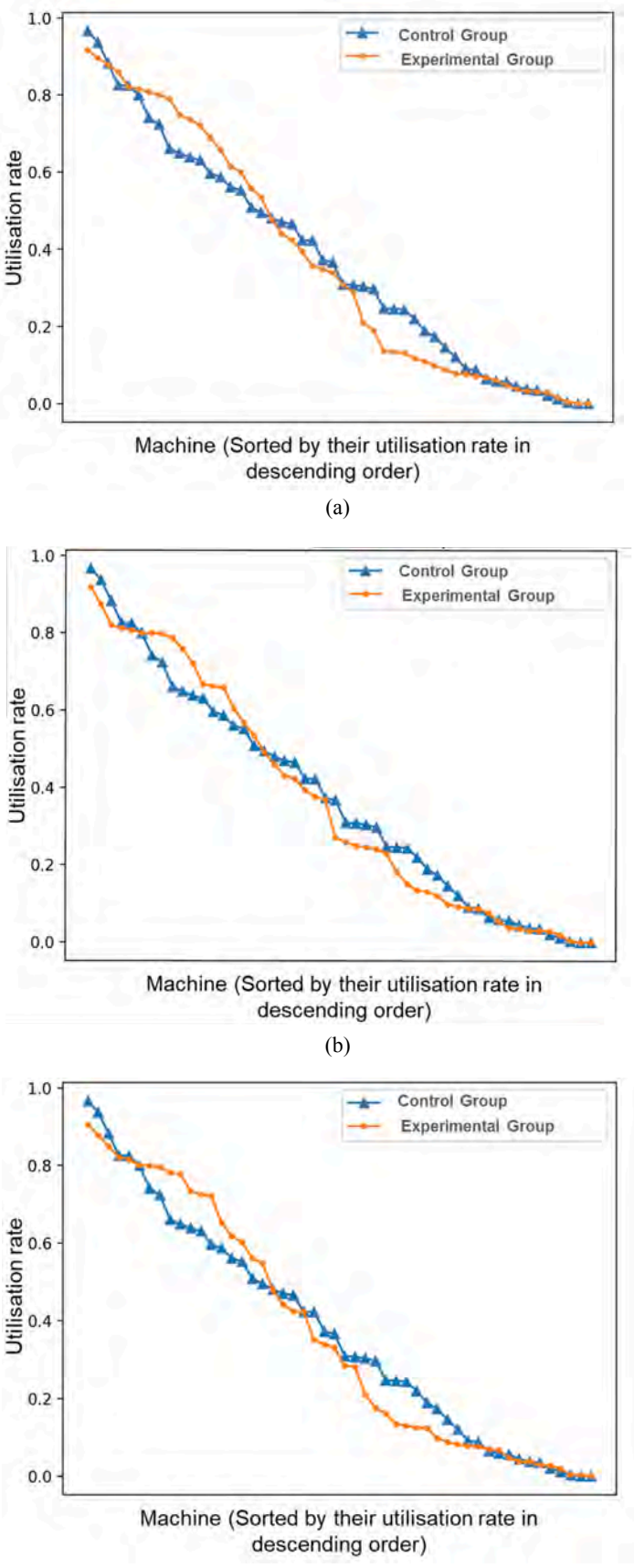

Figure. 2: The utilisation rate of machines in three sensitivity tests, showing a) utilisation rate of machines with a different set of tasks, b) utilisation rate of machines with a different cost parameter W_p, and c) utilisation rate of machines with a differenct weights for priority calculation

utilisation compared to conventional online scheduling methods.

Several promising directions for future research can be identified. For example, the current bilateral negotiation model could be extended to a multilateral cooperative game, in which groups of machines and complex tasks negotiate simultaneously to optimise the entire process route. Furthermore, investigating collaboration patterns within and across functional clusters in the manufacturing network (e.g. milling cells and final assembly lines) could lead to greater efficiency. Finally, it would be beneficial to explore the integration of machine learning to adaptively tune the parameters of the utility functions in response to changing production dynamics.

References

Allahverdi, A., Pesch, E., Pinedo, M., & Werner, F. (2018). Scheduling in manufacturing systems: new trends and perspectives. *International Journal of Production Research*, *56*(19), 6333-6335.

Barenji, A. V., Barenji, R. V., Roudi, D., & Hashemipour, M. (2017). A dynamic multi-agent-based scheduling approach for SMEs. *The International Journal of Advanced Manufacturing Technology*, *89*(9), 3123-3137.

Bi, M., Kovalenko, I., Tilbury, D. M., & Barton, K. (2024). Dynamic distributed decision-making for resilient resource reallocation in disrupted manufacturing systems. *International Journal of Production Research*, *62*(5), 1737-1757.

Dai, Y. H. (2013). A perfect example for the BFGS method. *Mathematical Programming*, *138*(1), 501-530.

Gaafar, L. K., & Masoud, S. A. (2005). Genetic algorithms and simulated annealing for scheduling in agile manufacturing. *International journal of production research*, *43*(14), 3069-3085.

Hu, M., Qin, S., Wang, S., Zhang, J., & Ding, G. (2025). An energy-saving real-time scheduling method based on bi-level multi-agent architecture with bargaining game for flexible job shops. *Expert Systems with Applications*, *269*, 126527.

Jules, G., & Saadat, M. (2016). Agent cooperation mechanism for decentralized manufacturing scheduling. *IEEE Transactions on Systems, Man, and Cybernetics: Systems*, *47*(12), 3351-3362.

Kang, K., Xu, S. X., Zhong, R. Y., Tan, B. Q., & Huang, G. Q. (2020). Double auction-based manufacturing cloud service allocation in an industrial park. *IEEE Transactions on Automation Science and Engineering*, *19*(1), 295-307.

Lee, J. H., & Kim, C. O. (2008). Multi-agent systems applications in manufacturing systems and supply chain management: a review paper. *International Journal of Production Research*, *46*(1), 233-265.

Leitão, P. (2009). Agent-based distributed manufacturing control: A state-of-the-art survey. *Engineering applications of artificial intelligence*, *22*(7), 979-991.

Li, Y., Tao, F., Cheng, Y., Zhang, X., & Nee, A. Y. C. (2017). Complex networks in advanced manufacturing systems. *Journal of Manufacturing Systems*, *43*, 409-421.

Liu, S., Zhang, L., Zhang, W., & Shen, W. (2021). Game theory based multi-task scheduling of decentralized 3D printing services in cloud manufacturing. *Neurocomputing*, *446*, 74-85.

Marzia, S., & Azab, A. (2023). Automated process planning and dynamic scheduling for smart manufacturing: A systematic literature review. *Manufacturing Letters*, *35*, 861-872.

Megow, N., Uetz, M., & Vredeveld, T. (2006). Models and algorithms for stochastic online scheduling. *Mathematics of Operations Research*, *31*(3), 513-525.

Minguillon, F. E., & Lanza, G. (2019). Coupling of centralized and decentralized scheduling for robust production in agile production systems. *Procedia CIRP*, *79*, 385-390.

Poudel, L., Elagandula, S., Zhou, W., & Sha, Z. (2023). Decentralized and centralized planning for multi-robot additive manufacturing. *Journal of Mechanical Design*, *145*(1), 012003.

Qian, C., Zhang, Y., Liu, Y., & Wang, Z. (2019). A cloud service platform integrating additive and subtractive manufacturing with high resource efficiency. *Journal of Cleaner Production*, *241*, 118379.

Qian, C., Zhang, Y., Jiang, C., Pan, S., & Rong, Y. (2020). A real-time data-driven collaborative mechanism in fixed-position assembly systems for smart manufacturing. *Robotics and Computer-Integrated Manufacturing*, *61*, 101841.

Sanogo, K., Benhafssa, A. M., & Sahnoun, M. H. (2025). A game theory approach for optimizing job shop scheduling problems with transportation in common shared human-robot environments. *Computers & Industrial Engineering*, 111366.

Sha, D. Y., & Lin, H. H. (2010). A multi-objective PSO for job-shop scheduling problems. *Expert Systems with Applications*, *37*(2), 1065-1070.

Uhlmann, I. R., & Frazzon, E. M. (2018). Production rescheduling review: Opportunities for industrial integration and practical applications. *Journal of manufacturing systems*, *49*, 186-193.

Veeramachaneni, V., Mallick, P. K., Rout, S., & Pareek, P. K. (2025). Efficient task scheduling for cloud environments with MSA: Enhancing makespan and resource utilization. In 2025 *International Conference on Emerging Systems and Intelligent Computing* (*ESIC*) (pp. 740-747). IEEE.

Wong, T. C., & Ngan, S. C. (2013). A comparison of hybrid genetic algorithm and hybrid particle swarm optimization to minimize makespan for assembly job shop. *Applied Soft Computing*, *13*(3), 1391-1399.

Xing, L., Dong, X., Guan, J., & Qiao, X. (2019). Betweenness centrality for similarity-weight network and its application to measuring industrial sectors' pivotability on the global value chain. *Physica A: Statistical mechanics and its applications*, *516*, 19-36.

Yang, M., Abubakar, A. H., & Jiang, P. (2021). Deep learning and complex network theory based analysis on socialized manufacturing resources utilisations and an application case study. *Concurrent Engineering*, *29*(3), 236-248.

Zan, X., Wu, Z., Guo, C., & Yu, Z. (2020). A Pareto-based genetic algorithm for multi-objective scheduling of automated manufacturing systems. *Advances in Mechanical Engineering*, *12*(1), 1687814019885294.

Zeng, L., Chen, H., Chen, M., & Zhao, X. (2024). Resilience assessment of the aircraft manufacturing core products supply chain: the international trade network perspective. *Annals of Operations Research*, 1-39.

Zhang, W., Bao, X., Hao, X., & Gen, M. (2025). Metaheuristics for multi-objective scheduling problems in industry 4.0 and 5.0: a state-of-the-arts survey. *Frontiers in Industrial Engineering*, *3*, 1540022.

Zhang, W. Y., Zhang, S., & Guo, S. S. (2017). A PageRank-based reputation model for personalised manufacturing service recommendation. *Enterprise Information Systems*, *11*(5), 672-693.

Zhang, Y., Qian, C., Lv, J., & Liu, Y. (2016). Agent and cyber-physical system based self-organizing and self-adaptive intelligent shopfloor. *IEEE Transactions on Industrial Informatics*, *13*(2), 737-747.

Zheng, P., Xia, L., Li, C., Li, X., & Liu, B. (2021). Towards Self-X cognitive manufacturing network: An industrial knowledge graph-based multi-agent reinforcement learning approach. *Journal of Manufacturing Systems*, *61*, 16-26.

Zhu, J. Y., Qin, W., Hu, J. H., Sun, Y. N., & Chen, Y. (2023). Influential process nodes identification strategy for aircraft assembly system based on complex network and improved PageRank. *Advanced Engineering Informatics*, *58*, 102187

IJAMMP

Development of a Mini CNC Milzling Machine for Educational Purposes at JMTI

Noor Azam Jaafar*, Ahmad Suffian Ismail, Mazni Tajudin and Risharwin Bala

RESEARCH ARTICLE

ARTICLE INFO

Keywords:

Arduino-based control; CNC milling machine; Educational machining; GRBL firmware; Mini CNC system

Article History

*Received:*24 October 2025
*Revised:*19 February 2026
*Accepted:*28 February 2026
Published:

The continuous advancement of modern manufacturing requires highly skilled personnel proficient in Computer Numerical Control (CNC) technology, making it an essential component of Technical and Vocational Education and Training (TVET). However, hands-on training is often limited by the high capital cost, large footprint, and maintenance complexity of industrial CNC machines. This study reports the design, fabrication, and performance evaluation of a Mini CNC Milling Machine developed as a compact and affordable training tool for the Japan-Malaysia Technical Institute (JMTI). The machine was designed using Autodesk Inventor and fabricated from aluminium 6061 through in-house processes including CNC milling and Wire Electrical Discharge Machining (WEDM), followed by anodizing for durability. The control system utilised an Arduino platform running the Grbl open-source G-code interpreter firmware to enable simplified G-code execution. Performance validation included motion accuracy testing, Manual Data Input (MDI) functionality assessment, and cutting accuracy evaluation. Motion testing using a 0.01 mm resolution dial gauge showed a maximum deviation of ±0.05 mm. The MDI test confirmed stable and immediate system response without errors. Cutting trials on acrylic (15 mm × 20 mm geometry) achieved an average dimensional deviation of ±0.01 mm. The results demonstrate that the developed system provides adequate precision for CNC programming education, prototyping, and light-duty machining applications.

1.Introduction

The modern manufacturing industry places a strong emphasis on proficiency in Computer Numerical Control (CNC) technology, making it a critical component of Technical and Vocational Education and Training (TVET) curricula (Tung et al., 2021). Institutions such as the Japan-Malaysia Technical Institute (JMTI) are tasked with producing technically competent graduates capable of operating CNC systems in industrial environments. CNC machines, controlled automatically by a computer, allow the creation of products with specified shapes and sizes. The integration of CAD/CAM systems with CNC machining enables high precision, repeatability, and automation in modern manufacturing processes. However, commercial CNC machines are typically large, complex, and expensive, making it difficult for educational institutions to acquire sufficient units for hands-on learning. A major challenge in CNC education is the high cost of ownership and maintenance of full-sized industrial CNC machines, which also require large operating spaces and significant energy consumption (Ali & Mohsin, 2021). These constraints limit practical exposure and reduce opportunities for students to develop operational competency.

Several studies have reported the development of low-cost mini CNC systems using open-source controllers and compact mechanical designs (Barik et al., 2023). While these systems demonstrate technical feasibility, many studies focus primarily on fabrication processes or controller implementation rather than comprehensive system validation. In particular, limited research provides integrated benchmarking of motion accuracy, manual control stability, and dimensional cutting precision within an educational training context. Furthermore, quantitative justification of acceptable tolerance ranges for CNC learning applications remains insufficiently discussed in existing literature. Therefore, this study aims to design, fabricate, and systematically validate a Mini CNC Milling Machine tailored for educational deployment at JMTI. Unlike previous studies that emphasize construction aspects, this research incorporates structured performance evaluation—including motion accuracy testing, Manual Data Input (MDI) validation, and cutting dimensional analysis—to determine the machine's suitability for CNC programming instruction and light machining applications. The findings contribute practical performance benchmarks for low-cost CNC systems within TVET environments.

Department of Mechanical & Production Engineering Technology, Manufacturing Division, Japan-Malaysia Technical Institute (JMTI), Penang, Malaysia

Corresponding author*: noorazamjaafar@jtm.gov.my

2. Literature Review

2.1 The Evolution and Role of CNC Technology

The history of Computer Numerical Control (CNC) machines traces back to the mid-20th century with the development of Numerical Control (NC) systems, pioneered in the 1940s to improve the precision of complex component manufacturing, particularly in aerospace applications. The early implementation of NC machines marked a significant transition from manual machining toward automated precision manufacturing. The subsequent integration of microprocessors further transformed NC systems into modern CNC machines capable of executing programmed instructions with high repeatability and accuracy.

Today, CNC technology forms the backbone of modern manufacturing systems, enabling high efficiency, precision, and automation. The integration of Computer-Aided Design (CAD) and Computer-Aided Manufacturing (CAM) with CNC machining allows the production of complex geometries with tight tolerances. In the context of Industry 4.0, CNC systems continue to evolve with features such as IoT-based monitoring, predictive maintenance capabilities, and intelligent process optimisation (Katduang et al., 2024).

Despite these advancements, industrial-grade CNC machines remain capital-intensive and operationally complex, limiting their accessibility for educational institutions. This limitation has encouraged the exploration of scaled-down CNC systems suitable for training environments.

2.2 The Role of Mini CNC Machines in Technical Education

Modern technical education requires hands-on exposure to CNC programming and machining operations. However, traditional industrial CNC machines present challenges due to high acquisition costs, space requirements, and maintenance demands (Ali & Mohsin, 2021). These constraints reduce machine availability and restrict practical student engagement.

In response, several studies have reported the development of Mini CNC Machines using cost-effective components such as stepper motors, ball screws, and open-source control platforms (Barik et al., 2023). These systems successfully demonstrate mechanical feasibility and controller implementation using Arduino-based Grbl firmware.

However, many reported studies primarily emphasize fabrication methodology and system assembly rather than comprehensive performance validation. In particular, systematic benchmarking of motion accuracy, manual control stability, and dimensional cutting precision is often limited or insufficiently quantified. Furthermore, acceptable tolerance ranges for educational machining applications are rarely justified with comparative analysis against published performance data.

Reported motion accuracy for low-cost 3-axis mini CNC systems generally falls within ±0.05 mm to ±0.10 mm under controlled conditions (Salam et al., 2020). While these values indicate feasibility for light machining applications, variations in structural rigidity, backlash control, and calibration procedures can significantly influence performance consistency. Therefore, simply demonstrating functionality does not necessarily confirm suitability for structured CNC training unless validated through repeatable and measurable performance testing.

Accordingly, a structured validation framework that integrates motion accuracy assessment, Manual Data Input (MDI) verification, and cutting dimensional analysis is required to determine the practical suitability of mini CNC systems for TVET-based instructional deployment. The following section outlines the systematic methodology adopted in this study to address this need.

3. Methodology

The project methodology applies a structured and sequential development approach based on the Waterfall Design Model to ensure systematic execution and performance validation of the Mini CNC Milling Machine. The Waterfall model remains relevant for engineering systems where requirements are clearly defined and design modifications after fabrication are costly and difficult to implement (Sommerville, 2016).

In hardware-based developments such as CNC machine fabrication, dimensional tolerances, mechanical alignment, and structural integration must be finalized prior to assembly to prevent cumulative geometric errors and performance degradation. Structured phase verification and requirement traceability are widely recommended in systems engineering practices for physical system integration and reliability assurance (Kossiakoff et al., 2019)

Furthermore, systematic and stage-based product development is strongly emphasized in classical engineering design methodology, where conceptual design, embodiment design, and detail design must be validated sequentially to ensure functional integrity (Pahl & Beitz, 2013).

Therefore, a sequential phase-based framework was adopted to maintain design consistency throughout mechanical fabrication and control system integration. As illustrated in Figure 1, the development process is

organized into distinct stages, beginning with planning and requirement analysis, followed by mechanical and electrical design, fabrication and assembly, and finally testing and performance evaluation. Each stage was completed and validated before proceeding to the subsequent phase to ensure alignment between structural rigidity, motion transmission accuracy, and control stability.

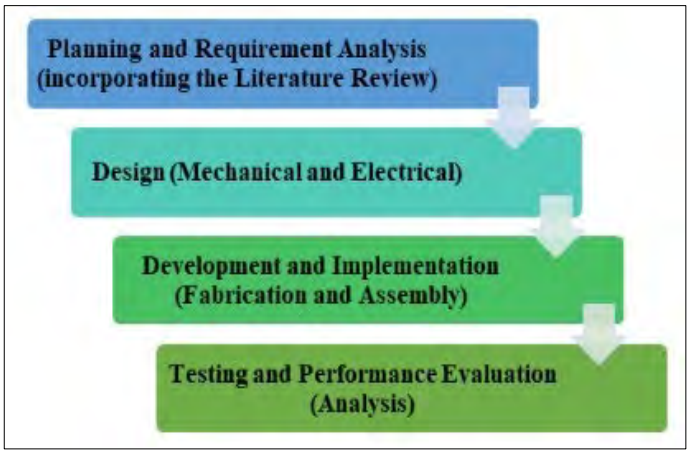

Figure 1. Waterfall Design Model

3.1 Design and Fabrication

The mechanical design phase was carried out using Autodesk Inventor for three-dimensional modelling, assembly visualization, and Bill of Materials (BOM) preparation. The use of CAD software enabled precise dimensional specification, tolerance control, and alignment verification prior to fabrication.

Accurate digital modelling is essential in small-scale CNC systems, as minor geometric deviations may significantly influence motion accuracy and repeatability. The complete assembly configuration and corresponding Bill of Materials (BOM) generated from the CAD model are presented in Figure 2, illustrating the structural framework, motion transmission components, and major mechanical elements of the Mini CNC Milling Machine.

Aluminium 6061 was selected as the primary structural material due to its favorable strength-to-weight ratio, good machinability, and adequate vibration resistance. In compact CNC platforms, structural rigidity plays a critical role in minimizing deflection and maintaining positional accuracy during cutting operations. Therefore, material selection and frame configuration were carefully considered to balance stiffness, weight, and manufacturability.

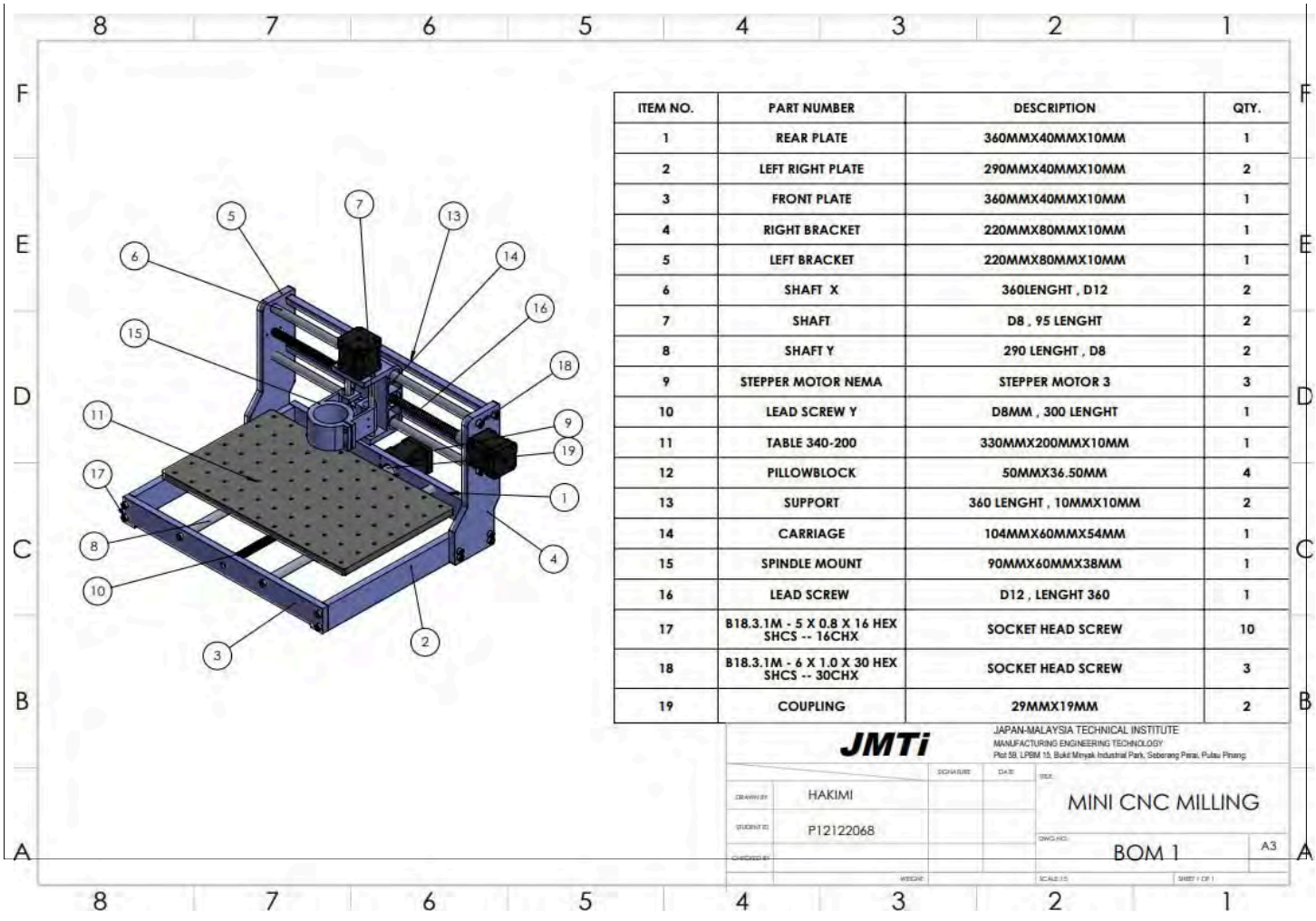

ITEM NO.	PART NUMBER	DESCRIPTION	QTY.
1	REAR PLATE	360MMX40MMX10MM	1
2	LEFT RIGHT PLATE	290MMX40MMX10MM	2
3	FRONT PLATE	360MMX40MMX10MM	1
4	RIGHT BRACKET	220MMX80MMX10MM	1
5	LEFT BRACKET	220MMX80MMX10MM	1
6	SHAFT X	360LENGHT , D12	2
7	SHAFT	D8 , 95 LENGHT	2
8	SHAFT Y	290 LENGHT , D8	2
9	STEPPER MOTOR NEMA	STEPPER MOTOR 3	3
10	LEAD SCREW Y	D8MM , 300 LENGHT	1
11	TABLE 340-200	330MMX200MMX10MM	1
12	PILLOWBLOCK	50MMX36.50MM	4
13	SUPPORT	360 LENGHT , 10MMX10MM	2
14	CARRIAGE	104MMX60MMX54MM	1
15	SPINDLE MOUNT	90MMX60MMX38MM	1
16	LEAD SCREW	D12 , LENGHT 360	1
17	B18.3.1M - 5 X 0.8 X 16 HEX SHCS -- 16CHX	SOCKET HEAD SCREW	10
18	B18.3.1M - 6 X 1.0 X 30 HEX SHCS -- 30CHX	SOCKET HEAD SCREW	3
19	COUPLING	29MMX19MM	2

Figure 2. Assembly view and Bill of Materials (BOM) of the Mini CNC Milling Machine

The motion transmission system incorporated stepper motors, ball screws, and linear guide rails to ensure controlled and repeatable axis movement. Ball screws were selected to reduce backlash compared to conventional lead screws, thereby improving positioning precision. Linear guide rails were used to provide smooth translational motion and maintain axis alignment under operational loading conditions.

The electrical control system was designed using an Arduino microcontroller integrated with Grbl open-source firmware. This architecture was selected due to its cost-effectiveness, compatibility with standard G-code commands, and suitability for educational applications. The overall electrical integration, including the Arduino controller, A4988 stepper motor drivers, regulated power supplies, and limit switches, is illustrated in Figure 3, which presents the complete circuit schematic of the system. The system also incorporated a regulated power supply and limit switches to enhance operational safety and motion boundary control.

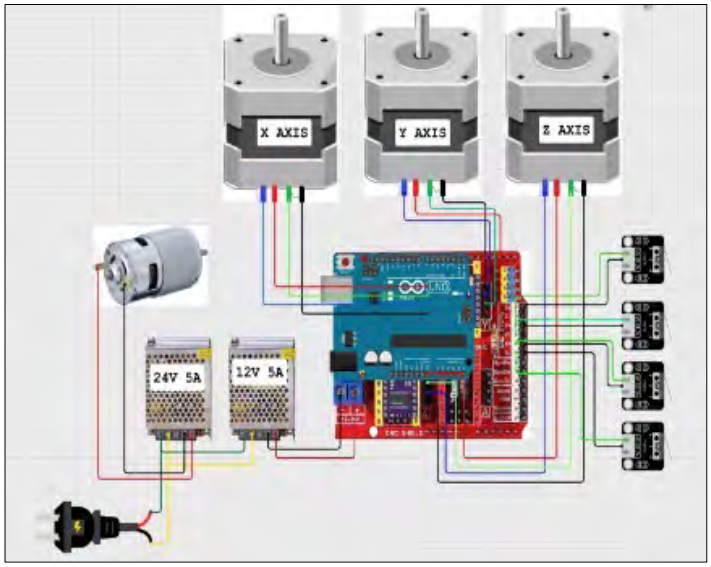

Figure 3. Electrical control schematic of the Mini CNC Milling Machine

Fabrication was conducted using in-house machining facilities, including CNC milling, CNC turning, and Wire Electrical Discharge Machining (WEDM). A final anodizing process was applied to aluminium components to improve surface durability and corrosion resistance. During assembly, careful alignment of ball screws and linear rails was performed to minimize geometric errors and cumulative tolerance deviations, which are critical factors affecting motion accuracy in small-scale CNC systems.

3.2 Testing and Performance Evaluation

Performance validation of the developed Mini CNC Milling Machine was conducted through three structured assessments: motion accuracy testing, Manual Data Input (MDI) functionality evaluation, and cutting accuracy verification. This multi-stage validation framework was implemented to ensure that both mechanical precision and control stability were systematically evaluated prior to confirming machining capability. The structured testing approach directly addresses the research gap identified in previous studies, where integrated benchmarking of mini CNC systems is often limited or insufficiently quantified.

3.2.1 Motion Accuracy Test

Motion accuracy testing was performed to evaluate the positional precision of the X, Y, and Z axes. Controlled displacement commands of 5 mm, 10 mm, and 15 mm were executed through the MDI interface. Actual displacement was measured using a 0.01 mm resolution dial gauge to ensure precise verification. The measurement setup for each axis is illustrated in Figure 4, where the dial gauge was securely mounted to provide direct linear displacement readings along the X, Y, and Z directions.

The dial gauge was positioned in direct contact with the moving carriage of each axis to minimize measurement error and eliminate lateral misalignment effects. Care was taken to ensure stable mounting and to reduce external vibration during measurement. Multiple readings were recorded for each displacement command to verify repeatability and consistency of the motion system. The resolution of the dial gauge (0.01 mm) ensures that the measurement uncertainty remains significantly lower than the observed deviation range, thereby enhancing the reliability of the recorded data.

The maximum deviation recorded did not exceed ±0.05 mm, with the Z-axis exhibiting the highest observed variation. This deviation range is consistent with reported performance levels of low-cost mini CNC systems, typically between ±0.05 mm and ±0.10 mm under controlled laboratory conditions (Salam et al., 2020). Therefore, the achieved motion accuracy is considered acceptable for CNC programming instruction, light machining, and educational prototyping applications. Minor deviations may be attributed to ball screw backlash, microstepping resolution of the stepper motors, and structural compliance of the compact frame design.

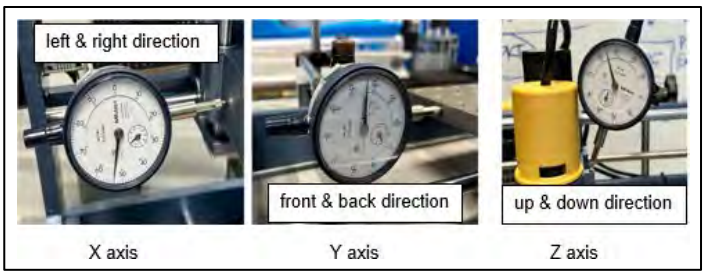

Figure 4. Motion accuracy measurement setup using a 0.01 mm dial gauge for X, Y, and Z axes

3.2.2 Manual Data Input (MDI) Functionality Test Tables and Figures

The MDI functionality test was conducted to evaluate the responsiveness and stability of the control system. Standard G-code commands including rapid positioning (G00), linear interpolation (G01), spindle activation (M03), and spindle stop (M05) were executed. Each command was tested across all axes to confirm synchronized motion behavior and reliable spindle response.

All commands were processed without observable delay, skipped steps, or execution errors. Immediate axis response and stable spindle activation confirmed effective communication between the Arduino controller, Grbl firmware, and A4988 motor drivers. Verification of manual command stability is particularly important in educational CNC systems, as students frequently rely on MDI inputs for initial setup, calibration, and program testing before executing full machining cycles.

3.2.3 Cutting Accuracy Test

To evaluate actual machining performance, a 15 mm × 20 mm rectangular profile was milled on acrylic material using controlled machining parameters (feed rate: 400 mm/min; spindle speed: 2000 rpm; depth of cut: 0.5 mm per pass). The target cutting geometry is illustrated in Figure 5, which presents the designed rectangular profile used for dimensional verification.

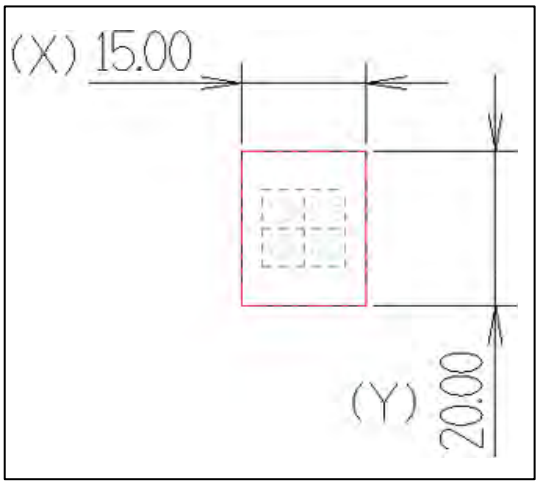

Fig. 5: Target rectangular geometry (15 mm × 20 mm) used for cutting accuracy evaluation

The geometry was selected due to its simple orthogonal configuration, allowing precise assessment of linear interpolation accuracy along both X and Y axes. The rectangular form enables direct comparison between programmed dimensions and the actual machined output, thereby providing a clear evaluation of geometric fidelity and motion synchronization during cutting operations.

Following machining, dimensional measurements were performed to determine deviation from the intended geometry. The machined workpiece was first captured using a calibrated digital imaging setup. Dimensional analysis was subsequently conducted using ImageJ software, an open-source image processing tool widely applied for scientific image measurement and geometric analysis (Schneider et al., 2012). Prior to measurement, pixel-to-length calibration was performed using a reference scale to ensure accurate dimensional conversion. The use of digital image-based measurement minimizes human reading error commonly associated with manual calipers and enhances repeatability and consistency in dimensional verification. The measured average dimensional deviation was approximately ±0.01 mm. The relatively lower cutting deviation compared to the maximum motion deviation suggests stable feed execution and consistent motion control during material removal.These results indicate that the developed Mini CNC Milling Machine is capable of maintaining acceptable geometric accuracy for CNC programming education, prototyping activities, and light-duty machining applications.

4. Result and Discussion

This section presents the experimental results obtained from motion accuracy testing, Manual Data Input (MDI) validation, and cutting performance evaluation. The findings are analysed and compared with previously reported mini CNC system performance to determine the suitability of the developed machine for educational deployment.

4.1 Motion Accuracy Test Result

The motion accuracy test results for the X, Y, and Z axes are summarized in Table 1, while the variation of positional error with respect to displacement distance is illustrated in Figure 6.

Table 1: Measured positional displacement and average motion error for X, Y, and Z axes

Commanded Displacement (mm)	X-axis Measured (mm)	Y-axis Measured (mm)	Z-axis Measured (mm)
5	4.98	5.02	4.97
10	9.95	10.03	9.92
15	15.02	14.96	15.01
Average Error (mm)	**±0.03**	**±0.04**	**±0.05**

Based on Table 1, minor deviations were observed across all axes for commanded displacements of 5 mm, 10 mm, and 15 mm. The average motion error recorded was ±0.03 mm for the X-axis, ±0.04 mm for the Y-axis, and ±0.05 mm for the Z-axis. Among the three axes, the Z-axis exhibited slightly higher variation, which may be attributed to gravitational loading effects and vertical structural compliance due to spindle mass and carriage weight distribution. The maximum deviation of ±0.05 mm at a commanded displacement of 15 mm corresponds to approximately 0.33% relative positioning error, indicating stable motion transmission and consistent mechanical alignment. This low percentage deviation demonstrates that cumulative geometric errors remain well-controlled within the compact structural configuration of the machine.

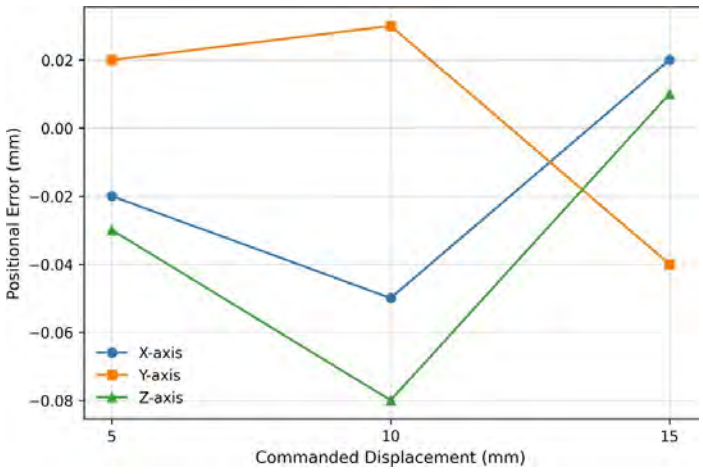

Figure 6. Motion error variation with respect to commanded displacement distance

As illustrated in Figure 6, the positional error does not increase proportionally with displacement distance. Instead, slight fluctuations are observed, particularly at 15 mm displacement for the Z-axis. This behavior suggests that error magnitude is influenced primarily by mechanical backlash, microstepping resolution of the stepper motors, and minor structural compliance rather than travel distance alone. The maximum deviation recorded did not exceed ±0.05 mm, which aligns with previously reported motion accuracy levels of mini CNC systems developed for educational applications (Tung et al., 2021; Salam et al., 2020). Compared to these reported values, the developed system performs within acceptable educational tolerance limits.

Repeated measurements confirmed consistent positioning behavior across multiple trials, indicating stable mechanical integration and reliable motion control. For CNC programming instruction and light-duty machining applications, a tolerance range within ±0.05 mm is considered acceptable, as micron-level industrial precision is not the primary requirement in educational environments.

4.2 Manual Data Input (MDI) System Stability

The Manual Data Input (MDI) functionality test was conducted to evaluate the responsiveness and operational stability of the control system. Standard G-code commands, including rapid positioning (G00), linear interpolation (G01), spindle activation (M03), and spindle stop (M05), were executed through the control interface.

The summarized test results are presented in Table 2. All axis movement commands for the X, Y, and Z directions were executed successfully without observable delay. Spindle activation and deactivation commands were also performed consistently. No motion execution errors or communication interruptions were detected during testing

Table 2: Results of Manual Data Input (MDI) functionality test

Function	Result
Axis Movement (X, Y, Z)	Successful without delay
Spindle Control	Successfully started and stopped
Movement Errors	None

The stable execution of MDI commands indicates effective communication between the Arduino controller, Grbl firmware, and A4988 stepper motor drivers. Reliable manual command processing is particularly important in educational CNC environments, where students frequently utilize MDI inputs during machine setup, zero referencing, and preliminary program verification.

Overall, the findings confirm that the developed Mini CNC Milling Machine exhibits stable and reliable control performance suitable for CNC programming instruction and laboratory-based machining activities.

4.3 Cutting Accuracy Evaluation

The cutting accuracy test was conducted to evaluate the machining performance of the developed Mini CNC Milling Machine. A rectangular geometry of 15 mm × 20 mm was milled on acrylic material under controlled machining parameters. The target cutting geometry used for dimensional verification is shown in Figure 5. The dimensional measurements obtained from five cutting samples are summarized in Table 3, while the dimensional consistency across samples is illustrated in Figure 7. Based on Table 3, the measured X-dimension values ranged between 14.96 mm and 15.02 mm, while the Y-dimension values ranged between 19.98 mm and 20.05 mm. The average measured dimensions were 14.99 mm (X-direction) and 20.01 mm (Y-direction), with corresponding average errors of approximately ±0.01 mm.

Table 3: Measured dimensional results of cutting accuracy test

Sample	Target Dimension (mm)	Measured X (mm)	Measured Y (mm)	X Error (mm)	Y Error (mm)
1	15 × 20	14.96	20.02	0.04	-0.02
2	15 × 20	15.01	19.98	-0.01	0.02
3	15 × 20	14.97	19.99	0.03	0.01
4	15 × 20	15.02	20.02	-0.02	-0.02
5	15 × 20	14.98	20.05	0.02	-0.05
Average	—	14.99	20.01	±0.01	±0.01

As illustrated in Figure 7, the dimensional variation across all five samples remains minimal and consistent. The fluctuation pattern does not indicate progressive dimensional drift, suggesting stable motion control and consistent feed execution during material removal.

The recorded average cutting deviation of ±0.01 mm is lower than the maximum motion deviation observed in Section 4.1 (±0.05 mm). This indicates that the machine maintains stable geometric fidelity during actual machining conditions. The achieved cutting precision falls within acceptable tolerance limits for educational CNC programming, prototyping tasks, and light-duty machining applications.

Overall, the results confirm that the developed Mini CNC Milling Machine demonstrates consistent and reliable cutting performance suitable for instructional deployment in TVET environments.

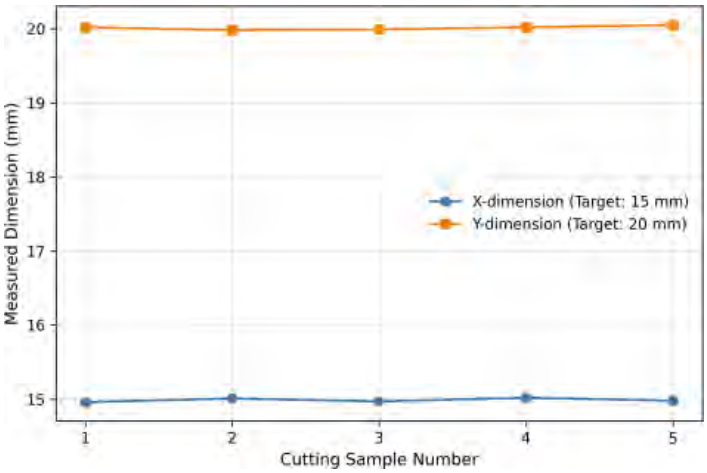

Figure 7. Measured dimensional variation across five cutting samples

5. Conclusion

This study presented the design, fabrication, and systematic performance evaluation of a Mini CNC Milling Machine developed for educational application at the Japan-Malaysia Technical Institute (JMTI). The development process followed a structured Waterfall Design Model to ensure systematic integration between mechanical design, electrical control architecture, and performance validation.

The motion accuracy test demonstrated that the maximum positional deviation did not exceed ±0.05 mm, corresponding to a relative positioning error of approximately 0.33% at maximum displacement. This performance is consistent with reported accuracy ranges of low-cost mini CNC systems in existing literature (Salam et al., 2020). The Manual Data Input (MDI) evaluation confirmed stable and error-free execution of essential G-code commands, indicating reliable communication between the Arduino controller, Grbl firmware, and stepper motor drivers.

Cutting accuracy assessment on a 15 mm × 20 mm rectangular geometry yielded an average dimensional deviation of approximately ±0.01 mm. The consistency of cutting results across multiple samples suggests stable motion control and effective structural alignment during machining operations.

Unlike many previously reported mini CNC developments that primarily emphasize fabrication feasibility, this study incorporated structured benchmarking across motion accuracy, manual control validation, and cutting precision. The results confirm that the developed system achieves acceptable tolerance levels for CNC programming education, basic prototyping, and light-duty machining applications.

Although the developed machine is not intended to replace industrial-grade CNC systems, it provides a compact, cost-effective, and functionally reliable alternative suitable for TVET laboratory deployment. Future work may include long-term durability testing, dynamic load analysis, and expanded machining trials on different materials to further enhance system validation.

6. Implications and Recommendations

6.1 Implications for Education and Industry

The findings of this study provide meaningful practical implications for both technical education institutions and small-scale industrial applications. The developed Mini CNC Milling Machine offers a cost-effective training platform that enables a larger number of students to gain

hands-on experience in CNC programming, machine setup, and basic machining operations. In TVET environments, accessibility to practical equipment plays a critical role in skill development; therefore, the compact and affordable configuration of the system supports broader instructional deployment. Beyond educational use, the developed system may also serve Small and Medium-sized Enterprises (SMEs) that require low-cost solutions for light machining tasks, prototyping, and small-batch production where high industrial precision is not essential.

6.2 Recommendations for Enhancement

Although the developed machine achieved acceptable performance levels, several improvements may further enhance its accuracy and structural robustness. To improve motion accuracy, the use of higher-grade ball screws with reduced backlash is recommended. Additionally, the integration of a position encoding system (encoder) could enhance real-time axis position feedback and improve movement verification capability. To enhance structural stability, future designs should consider upgrading frame material rigidity and improving linear rail alignment precision during assembly. Structural reinforcement and optimized mounting techniques may further reduce vibration during machining operations.

6.3 Future Development

Future research should focus on expanding system capability through the development of advanced control strategies, including closed-loop motion control and improved motion calibration techniques. Integration with Industry 4.0 technologies, such as remote monitoring and performance data logging, may further enhance system functionality and educational relevance.

ACKNOWLEDGEMENT

The authors would like to express their sincere appreciation to the Japan-Malaysia Technical Institute (JMTI) for the financial support provided through the Dana Inovasi JMTI, which made the development and performance evaluation of the Mini CNC Milling Machine possible.

REFERENCES

Ali, S. M., & Mohsin, H. (2021). Design and fabrication of 3-axes mini CNC milling machine. IOP Conference Series: Materials Science and Engineering, 1094(1), 012005. https://doi.org/10.1088/1757-899x/1094/1/012005

Barik, S., Thakur, A., & Sharma, P. (2023). Design and fabrication of a compact CNC milling system using open-source control architecture. Materials Today: Proceedings, 72, 1450–1456.

Katduang, S., Panyathip, P., & Wongchai, A. (2024). Integration of Industry 4.0 technologies in CNC machining systems: A review. Journal of Manufacturing Systems, 72, 310–325.

Kossiakoff, A., Sweet, W., Seymour, S., & Biemer, S. (2019). Systems engineering principles and practice (3rd ed.). Wiley.

Pahl, G., & Beitz, W. (2013). Engineering design: A systematic approach (3rd ed.). Springer.

Salam, M. A., Rahman, M. M., & Hossain, M. S. (2020). Performance analysis of a desktop CNC milling machine for educational training. Procedia Manufacturing, 46, 564–571.

Schneider, C. A., Rasband, W. S., & Eliceiri, K. W. (2012). NIH Image to ImageJ: 25 years of image analysis. Nature Methods, 9(7), 671–675. https://doi.org/10.1038/nmeth.2089

Sommerville, I. (2016). Software engineering (10th ed.). Pearson.

Tung, H. Y., Lim, S. C., & Rahman, A. A. (2021). CNC education in TVET institutions: Current challenges and opportunities. Journal of Technical Education and Training, 13(2), 45–58.

IJAMMP

Predictive Maintenance of a Centrifugal Pump Using Vibration Analysis

Zambri bin Abdul Halim *, Mohamad Fauzi Bin Abu Bakar , Fakhrul Azman Bin Mohamed and Azizi Bin Mat Shariff

RESEARCH ARTICLE

ARTICLE INFO

Keywords:

Predictive maintenance;
Centrifugal pump;
Vibration analysis;
Bearing fault diagnosis;
Order analysis

Article History

*Received:*24 October 2025
*Revised:*19 February 2026
*Accepted:*28 February 2026
Published:

Centrifugal pumps are critical components in industrial systems where bearing failures may result in significant downtime and economic losses. This study investigates the vibration condition of a 450 kW centrifugal pump using condition-based predictive maintenance techniques. Vibration data were acquired from Pump Bearing #4 (Free End, 6321) under steady-state operation and analyzed using Time Waveform (TWF) and Fast Fourier Transform (FFT) spectrum analysis. The calculated bearing characteristic frequencies—Fundamental Train Frequency (FTF), Ball Pass Frequency Outer Race (BPFO), Ball Pass Frequency Inner Race (BPFI), and Ball Spin Frequency (BSF)—were compared with spectral peaks expressed in order analysis. Results indicate dominant harmonics between 21× and 25× orders corresponding to BPFI, confirming advanced inner race spalling. Sideband modulation and repetitive impact patterns further support the diagnosis. Physical inspection after disassembly validated the presence of localized inner and outer race damage. The findings demonstrate that vibration-based condition monitoring is effective for early fault detection and fault progression assessment in high-power centrifugal pump systems.

1.Introduction

Centrifugal pumps play a critical role in industrial sectors including power generation, petrochemical processing, and water treatment, where their reliability directly affects plant availability and operational continuity. As highlighted by Singh and Saini (2023), the performance stability of centrifugal pumps is closely linked to effective fault detection strategies. In practice, unexpected pump failures often lead to production downtime, increased energy consumption, and elevated maintenance costs, with bearing degradation identified as a major contributor to rotating machinery breakdown (Zhao et al., 2020). Traditional preventive and corrective maintenance strategies are frequently insufficient for detecting incipient bearing defects before severe damage develops.

Consequently, predictive maintenance approaches—particularly vibration-based condition monitoring—have gained widespread acceptance in industrial diagnostics (Lei et al., 2021). Randall and Antoni (2020) emphasized that frequency-domain analysis enables the identification of characteristic defect frequencies associated with specific bearing fault mechanisms.

Department of Mechanical & Production Engineering Technology, Mechatronic Division, Japan-Malaysia Technical Institute (JMTI), 14100, Simpang Ampat, Penang, Malaysia

Corresponding author*: zambri@jtm.gov.my

More recent advancements in signal processing further enhance diagnostic sensitivity. Techniques such as envelope spectrum analysis, spectral kurtosis, and order tracking have been shown to improve early-stage defect detectability, especially under noisy or variable-speed operating conditions (Kumar & Sharma, 2024; Zhang et al., 2022). These developments reinforce the importance of combining classical frequency analysis with advanced processing methods.

In this context, the present study investigates the vibration behaviour of Pump Bearing #4 (Free End, 6321) in a 450-kW centrifugal pump system. The analysis focuses on frequency-domain characteristics and comparative assessment within the drive train. Particular attention is given to the identification of key bearing fault frequencies—including Ball Pass Frequency Inner race (BPFI), Ball Pass Frequency Outer race (BPFO), Ball Spin Frequency (BSF), and Fundamental Train Frequency (FTF)—to evaluate fault severity and progression.

2. Literature Review

The characteristic fault frequencies of a rolling element bearing are governed by its geometric parameters, including the number of rolling elements, pitch diameter, rolling element diameter, contact angle, and shaft rotational speed. These parameters determine the location of defect-related spectral components and constitute the theoretical

foundation of vibration-based bearing diagnostics. As discussed by Randall and Antoni (2020), the analytical formulation of bearing characteristic frequencies enables precise identification of defect mechanisms in the frequency domain.

Recent studies further confirm that characteristic defect frequencies—such as Ball Pass Frequency of the Inner Race (BPFI), Ball Pass Frequency of the Outer Race (BPFO), Ball Spin Frequency (BSF), and Fundamental Train Frequency (FTF) are remain widely applied in modern industrial condition monitoring systems for fault localization and severity assessment (Zhang et al., 2022).

$$\mathrm{BPFI} = \frac{Z}{2} S \left[1 + \left(\frac{B_d}{P_d}\right) \cos\theta\right] \quad (1)$$

$$\mathrm{BPFO} = \frac{Z}{2} S \left[1 - \left(\frac{B_d}{P_d}\right) \cos\theta\right] \quad (2)$$

$$\mathrm{BSF} = \frac{P_d}{2B_d} S \left[1 - \left(\frac{B_d}{P_d}\right)^2 \cos^2\theta\right] \quad (3)$$

$$\mathrm{FTF} = \frac{1}{2} S \left[1 - \left(\frac{B_d}{P_d}\right) \cos\theta\right] \quad (4)$$

Where:

- S = rotational speed in revolutions per second.
- Z = number of rolling elements.
- B_d = ball or roller diameter, mm.
- P_d = bearing pitch diameter, mm.
- θ = contact angle.

Characteristic fault frequencies provide a reliable basis for diagnosing rolling element bearing defects. Outer race faults typically produce dominant BPFO components and harmonics, while inner race defects are characterized by strong BPFI responses accompanied by sideband modulation spaced at the shaft rotational frequency (Lei et al., 2021; Singh & Saini, 2023). Rolling element and cage defects are generally associated with BSF and FTF components, respectively, reflecting their distinct kinematic behavior (Randall & Antoni, 2020).

Recent advancements highlight that integrating these theoretical fault frequencies with envelope analysis, spectral kurtosis, and order tracking significantly improves fault localization accuracy, particularly under variable-speed and noisy operating conditions (Kumar & Sharma, 2024; Zhang et al., 2022; Zhao et al., 2020).

3. Measurement Setup and Methodology

The vibration measurement configuration for the centrifugal pump system is summarized in Table 1. The test was performed on a 450 kW centrifugal pump operating at 989 RPM (≈ 16.48 Hz), equipped with a closed six-blade impeller and a direct motor–pump coupling. The bearing under investigation was the pump free-end bearing (Location #4), identified as a 6321 deep-groove ball bearing designed to support both radial and axial loads. Vibration-based diagnostics of centrifugal pump bearings under steady-state conditions remain a widely accepted approach for reliable spectral fault identification (Lei et al., 2021; Singh & Saini, 2023). As emphasized by Zhao et al. (2020) and Kumar and Sharma (2024), appropriate sensor placement and multi-directional measurements are critical to improving diagnostic sensitivity. In this study, a tri-axial accelerometer was mounted vertically on the pump housing to capture vibration responses transmitted through the bearing structure, consistent with modern condition monitoring frameworks. All measurements were acquired under stable operating conditions to ensure consistency in frequency-domain analysis and accurate identification of characteristic defect frequencies. The reliability of steady-state spectral interpretation has been extensively discussed in the literature, particularly in relation to harmonic identification and fault localization (Randall & Antoni, 2020; Zhang et al., 2022).

Table 1. Measurement setup for centrifugal pump system.

Parameter	Specification
Motor power	450 KW
Operating Speed	989 RPM (~16.48 Hz)
Pump Type	Centrifugal (closed impeller, six blades)
Coupling	Motor–pump direct coupling
Bearing Inspected	6321 deep groove ball bearing
Location	pump free end (Location #4)

Vibration measurements were collected in axial, tangential, and radial directions using the Fluke 810 diagnostic analyzer. The calculated fault frequencies for the 6321 bearing are summarized in Table 2, with order values of FTF = 0.38, BPFO = 3.08, BPFI = 4.92, and BSF = 2.05.

Table 2 summarizes the key fault frequency formulas used in this study. The Fundamental Train Frequency (FTF) represents the cage rotational frequency and is primarily used to detect cage-related faults. The Ball Pass Frequency Outer Race (BPFO) and Ball Pass Frequency Inner Race (BPFI) correspond to defects occurring on the outer and inner raceways, respectively, while the Ball Spin Frequency (BSF) represents the rotation of the individual rolling elements, which is associated with ball surface damage. The calculated theoretical order values for the 6321 bearing were 0.38× for FTF, 3.08× for BPFO, 4.92× for BPFI, and 2.05× for BSF, where "×" indicates multiples of the shaft rotational speed. These order values serve as reference points in the vibration spectrum for identifying characteristic defect peaks.

Table 2 Bearing 6321 fault frequencies.

Fault frequency	Formula	Description	Order value
FTF (Fundamental Train Frequency)	$FTF = \frac{1}{2} f_r \left[1 - \left(\frac{d}{D_p}\right)\cos\theta\right]$	Cage frequency; useful for detecting cage faults.	0.38
BPFO (Ball Pass Frequency, Outer Race)	$BPFO = \frac{Z}{2} f_r \left[1 - \left(\frac{d}{D_p}\right)\cos\theta\right]$	Outer race defect frequency.	3.08
BPFI (Ball Pass Frequency, Inner Race)	$BPFI = \frac{Z}{2} f_r \left[1 + \left(\frac{d}{D_p}\right)\cos\theta\right]$	Inner race defect frequency.	4.92
BSF (Ball Spin Frequency)	$BSF = \frac{D_p}{2d} f_r \left[1 - \left(\frac{d}{D_p}\cos\theta\right)^2\right]$	Ball spin frequency; indicates ball defects.	2.05

Figure 1 shows the vibration measurement setup on the centrifugal pump assembly. A tri-axial accelerometer was mounted on the vertical position of the free-end bearing housing, which supports the pump shaft and accommodates axial and thermal expansion during operation.

Figure 1: Tri-axial acceleration sensor mounted on bearing #4 (Free End, 6321) in vertical direction.

4. Results and Discussion

4.1 Time Waveform (TWF)

Figure 2 shows the time waveform (TWF) signals for both axial and radial directions indicate periodic impact patterns with a fundamental period of approximately 0.062 s, corresponding to the shaft rotational speed of around 16.48 Hz. The axial signal exhibits higher impulsive peaks compared to the radial direction, suggesting stronger thrust or axial loading transmitted through the bearing structure. The presence of repeated impacts in both axes implies localized bearing excitation, possibly due to inner-race or rolling-element surface irregularities that generate vibration responses synchronized with shaft rotation.

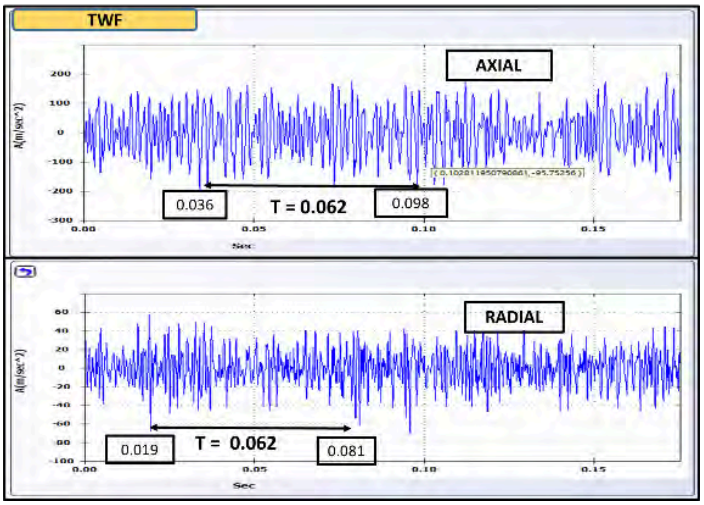

Figure 2: Time waveform (TWF) signals for both axial and radial directions.

4.2 High range spectrum analysis

Figure 3 shows the spectrum shows a dominant peak at 25× order with amplitude ~10.15 mm/s, matching harmonics of BPFI (Ball Pass Frequency Inner race). This indicates advanced inner race fault. The axial direction is most severe because thrust load from the impeller is transmitted through the inner race. Figure 4 shows a strong spectral peak at 21× order with amplitude ~9.17 mm/s. Tangential vibration confirms bearing fault modulation due to spalling. Sidebands around 20× and 22× orders indicate repeated impacts each time rolling elements pass the defect. High tangential amplitude shows the defect is in an advanced stage.

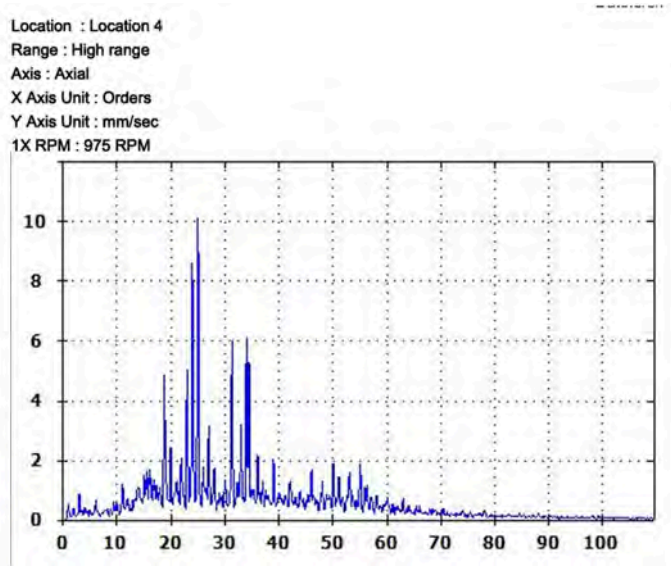

Figure 3. Spectrum Axial (High Range) – Pump Bearing #4 (Free End, 6321).

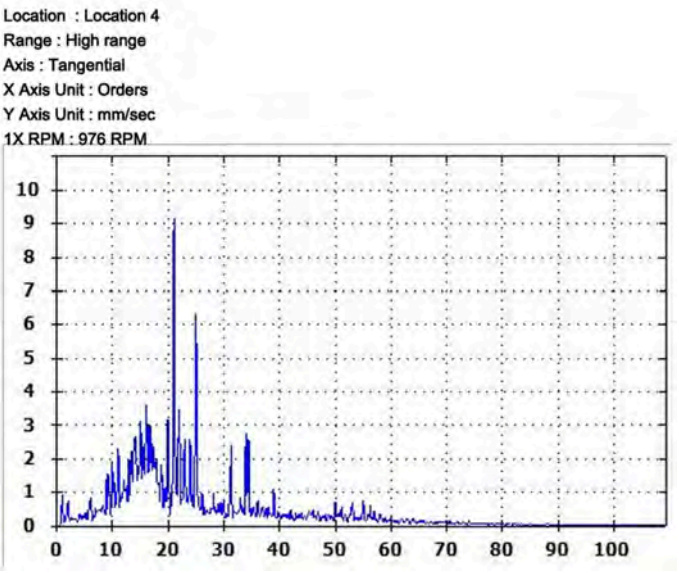

Figure 4: Spectrum Tangential (High Range) – Pump Bearing #4 (Free End, 6321).

Figure 5 shows a zoomed view of the spectral region around the dominant 21× order peak shown in Figure 4. In addition to the principal harmonic at approximately 21×, adjacent spectral components are clearly observed at approximately 20× and 22× orders. The spacing between these peaks is approximately equal to 1× shaft rotational frequency.

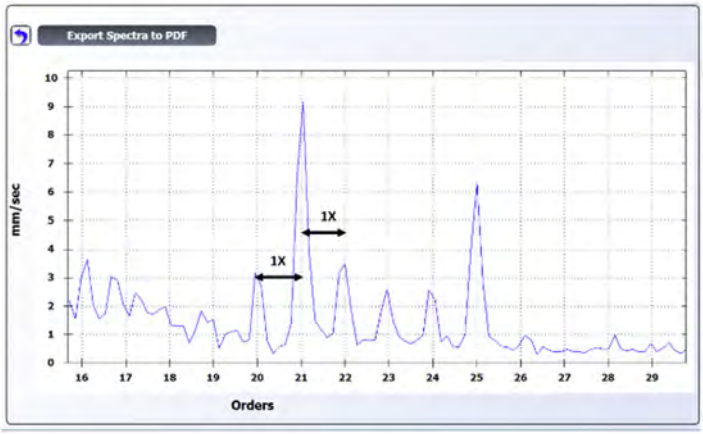

Fig. 5: Enlarged Spectrum from Figure 4 Showing ±1× Sidebands Around the BPFI Harmonic.

Sidebands arise from amplitude modulation, which occurs when a high-frequency defect signal is periodically influenced by a lower-frequency rotating component. In rolling element bearings, a localized defect on the inner race rotates together with the shaft. Each time a rolling element passes over the defect, an impact is generated. However, because the defect itself rotates with the shaft, the impact intensity varies cyclically with shaft rotation. This periodic variation in amplitude produces modulation at the shaft rotational frequency. Such symmetric ±1× spacing indicates amplitude modulation behavior. In rolling element bearings, when a localized inner race defect rotates with the shaft, the impact-induced vibration signal is periodically modulated at shaft rotational frequency.

This produces frequency components of the form:

$$f = f_{\text{fault}} \pm n f_r \tag{5}$$

where f_r is the shaft rotational frequency and n is an integer sideband order.

In the present spectrum, symmetric peaks at approximately 20× and 22× surrounding the dominant 21× component demonstrate clear ±1× spacing. This confirms that the 21× harmonic is modulated by the shaft rotational frequency. Such modulation behavior is widely recognized as a diagnostic signature of inner race defects, as damage on the inner race rotates with the shaft and inherently produces amplitude modulation effects (Lei et al., 2021; Randall & Antoni, 2020).

Figure 6 presents the radial spectrum, which exhibits a lower dominant amplitude of approximately 1.54 mm/s at 25× order but shows broadband excitation extending up to 34× order. This broadband response is characteristic of impact-induced energy exciting structural resonances within the bearing–housing system. Although the radial vibration severity is lower compared to axial and tangential directions, the presence of broadband excitation confirms the propagation of impulsive energy through the housing structure, indicating ongoing fault progression.

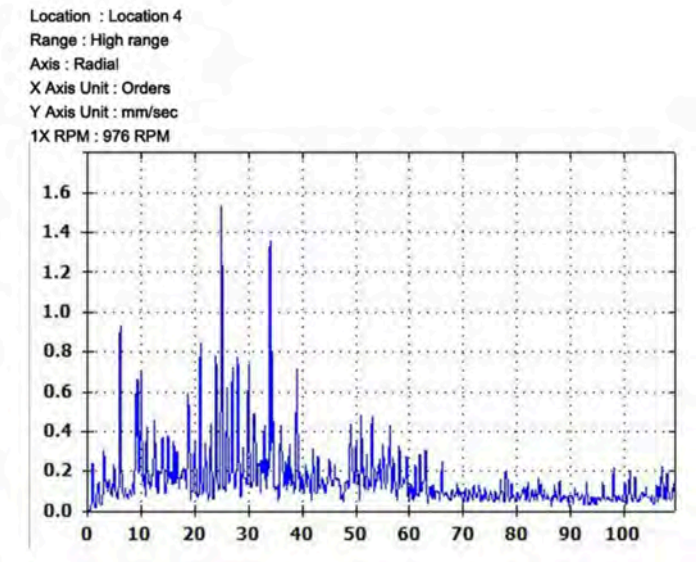

Figure 6: Spectrum Radial (High Range) – Pump Bearing #4 (Free End, 6321).

4.3 Low range spectrum analysis

Figure 7 shows peaks detected at 3.05× (0.86 mm/s) and 6.1× (0.83 mm/s) orders fall within the Ball Spin Frequency (BSF) sideband region, indicating early impact modulation. Although amplitudes are smaller compared to high range, the sideband pattern is an early symptom of inner race defect development. This shows fault initiation before high-order harmonics dominate.

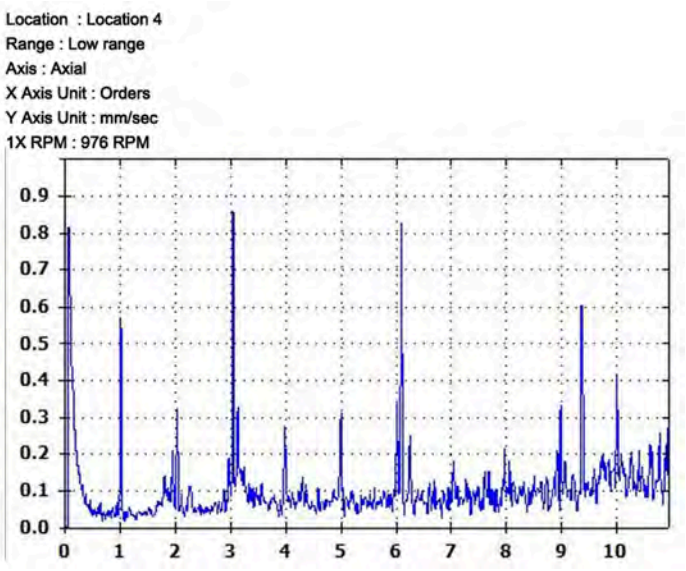

Figure 7. Spectrum Axial (Low Range) – Pump Bearing #4 (Free End, 6321)

Figure 8 shows peaks at 8.84× (1.60 mm/s) and 9.21× (1.45 mm/s) orders align with BPFI (Ball Pass Frequency Inner race). This provides direct evidence of early inner race defect. Sidebands surrounding BPFI confirm repeated rolling element impacts at the defect. Tangential direction is highly sensitive for early-stage detection, making it suitable for long-term trend monitoring.

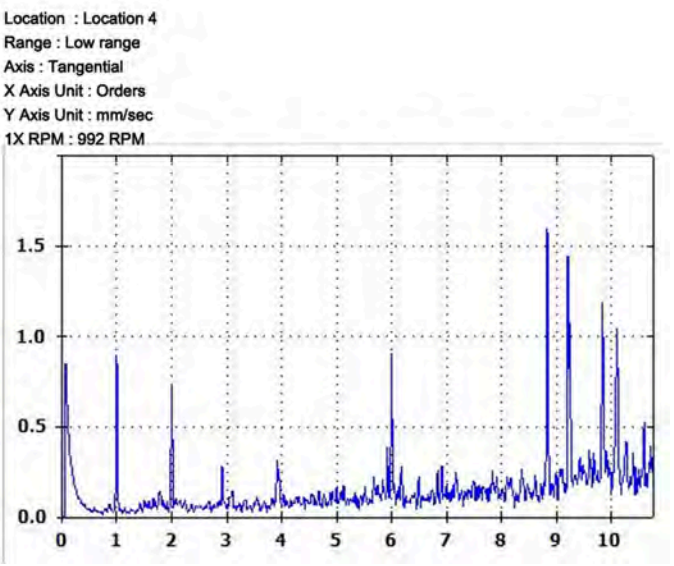

Figure 8: Spectrum Tangential (Low Range) – Pump Bearing #4 (Free End, 6321).

Figure 9 shows a peak around 9.84× order (0.62 mm/s) indicates harmonic/sideband build-up. Although amplitudes are lower than axial/tangential, the radial spectrum confirms that defect energy is spreading. This spectrum acts as secondary evidence supporting inner race fault diagnosis.

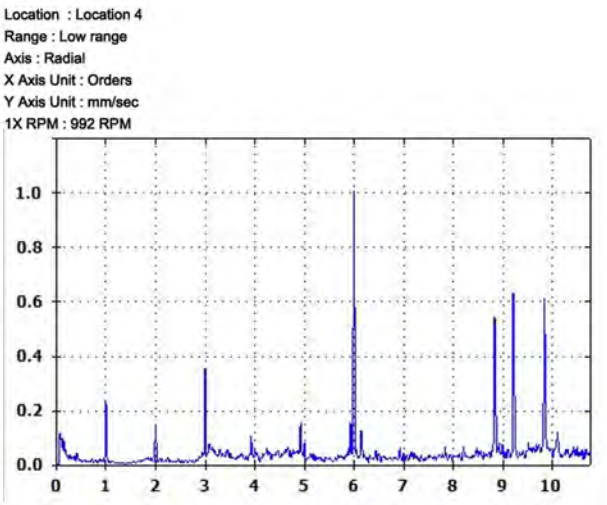

Figure 9. Spectrum Radial (Low Range) – Pump Bearing #4 (Free End, 6321).

Figure 10 shows the physical condition of Pump Bearing #4 (Free End, 6321) after disassembly, confirming the presence of a localized inner race spalling defect. The damage is characterized by a distinct pit and material flaking along the raceway, consistent with surface fatigue failure resulting from repeated rolling contact stress. This type of defect typically develops when localized subsurface cracks propagate to the surface under cyclic loading. The physical evidence aligns with the vibration analysis results, where the BPFI (Ball Pass Frequency of Inner Race) and its harmonics were dominant in both the low- and high-range spectra, indicating progressive inner race degradation. The visual confirmation validates the diagnostic conclusion obtained from the TWF and FFT analyses.

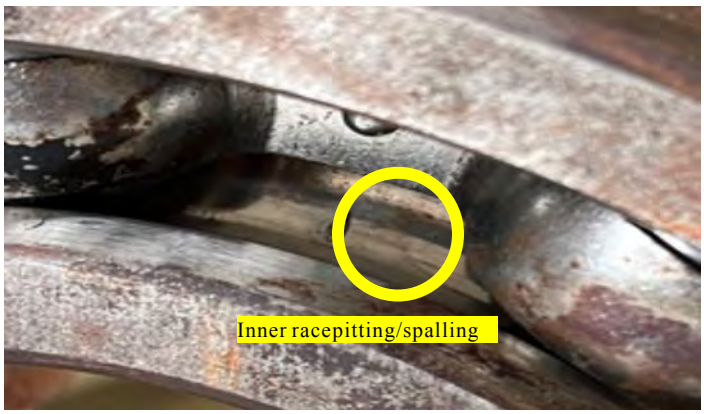

Figure 10. The physical condition of Pump Bearing #4 (Free End, 6321) after disassembly.

5. Conclusion

The time waveform (TWF) and order-based spectral analyses confirm a localized inner race defect in Pump Bearing #4 (Free End, 6321). The repetitive impact impulses, symmetric ±1× sideband spacing, and amplitude modulation behavior provide strong evidence of inner race spalling. The dominant harmonics observed in the 21×–25× order range indicate nonlinear impact excitation and resonance amplification, suggesting that the defect has progressed to an advanced stage.

The combined interpretation of low-range and high-range spectra enables systematic fault progression assessment, where early BPFI-related components evolve into dominant higher-order harmonics as severity increases. From a maintenance perspective, order-based monitoring with sideband verification should be incorporated into routine condition monitoring to support predictive maintenance planning and prevent unplanned failure.

This study was conducted under steady-state operating conditions on a single bearing configuration. Future research should extend the analysis to variable-speed environments and integrate advanced signal processing techniques, such as envelope analysis and spectral kurtosis, to enhance early fault detection and diagnostic reliability.

References

Kumar, S., & Sharma, R. (2024). Multi-sensor data fusion for intelligent predictive maintenance of rotating machinery. Sensors, 24(3).

Lei, Y., Li, N., Guo, L., Li, N., Yan, T., & Lin, J. (2021). Machinery health prognostics: A systematic review from data acquisition to RUL prediction. Mechanical Systems and Signal Processing, 104, 799–834.

Randall, R. B., & Antoni, J. (2020). Rolling element bearing diagnostics—Recent advances. Mechanical Systems and Signal Processing, 145.

Singh, A., & Saini, P. K. (2023). Vibration-based fault diagnosis of centrifugal pumps: A review. Journal of Fluids Engineering, 145(4).

Zhang, X., Qin, Q., & Wang, H. (2022). Order tracking and time–frequency analysis for bearing fault diagnosis under variable speed conditions. Journal of Vibration and Control, 28(5–6), 712–728.

Zhao, R., Yan, R., Chen, Z., Mao, K., & Shen, F. (2020). Deep learning and vibration-based predictive maintenance: A review. IEEE Access, 8, 131363–131378.

IJAMMP

Optimization of Weld Bead Geometry for Cold-Rolled Thin Steel Plate Lap Joints using ColdArc Welding

Saiful Din Sabdin[1,a], Mohd Aidil Shah Abdul Rahim[2,b], Rashdan Awang Abdullah[3]

RESEARCH ARTICLE

ARTICLE INFO

Keywords:

ColdArc, Arc welding, Cold-Rolled, Automotive

Article History

*Received:*24 October 2025
*Revised:*19 February 2026
*Accepted:*28 February 2026
Published:

The profile of weld bead geometry plays a vital role in establishing the joint quality of lap configurations. Refining these geometric attributes is crucial for maintaining the robustness of the structure, particularly within automotive applications. It remains challenging to join thin plates effectively by optimizing process parameters to achieve compatible joints. This study aims to examine the interaction between parameters by developing mathematical equations to predict the bead geometry in ColdArc welding. The experiments were set-up using ER70S-6 steel wire on cold-rolled structural workpieces. Shielding was provided by a gas mixture of 80% Argon and 20% CO_2 with a 1.0 mm diameter mild steel filler wire. A set of experiments was performed to collect data using the Central Composite Design (CCD) technique of Response Surface Methodology (RSM). A total of 20 experiments were conducted based on the RSM design. The results of the confirmation experiments demonstrated that the developed mathematical models could predict the bead geometry with reasonable accuracy. This study proved that interaction effects play a major role in determining bead dimensions. The process successfully minimized the bead width and bead height parameters using RSM.

1.Introduction

Weld bead geometry significantly influences the mechanical and metallurgical features of a weld, which are directly related to the welding process parameters. One of the qualities in the respected components depends on weld bead geometry and coefficient shape of welds and dilution (Biber et al., 2024). The process of depositing a thick layer of filler material on low carbon steel base metal/Weld bead geometry discovers new finding and applications in repairing worn out parts for achieving good corrosion resistant surface. Usually, this process is called surfacing technique in which relatively, thick coating for several millimeters were applied. Bead geometry is a surfacing technique that involves improvement of surface strength of mother metal which considerably to increase service life of the parent material without changing the microstructure of base material (Mondal et al., 2016). The mechanical and metallurgical feature of weld is depending on bead geometry which is directly related to welding process parameters (Wordofa et al., 2024).

[1]Metal Fabrication Department, Advance Training Center (ADTEC), Tangkak Campus, Km 43, Jalan Segamat, Sagil, 84900 Tangkak, Malaysia

[2]Tool Department (Die), Proton Institute @ ADTEC Melaka, 78000 Alor Gajah, Melaka, Malaysia

[3] TWI Technology (S.E.Asia) Sdn Bhd, Section U5, Jalan Utarid U5/13, Mutiara Subang, 40150 Shah Alam, Selangor

Corresponding authors: [a]saifulkdh@yahoo.com, [b] aidilshah@jtm.gov.my

Gas Metal Arc Welding (GMAW) remains a dominant technique for assembling metallic parts in the automotive sector (Basak et al., 2025). Recently, the light engineering industry has implemented more rigorous standards for welding operations, specifically regarding thin-gauge materials (Sabdin, Hussein, Sued, & Ayof, 2018). The prerequisites, which are progressively normal, and have turned out to be set up as objectives for new innovation innovative work (Kah et al., 2012; Zamzami et al., 2017). ColdArc is a variant of GMAW technology based on the short-circuiting transfer concept (Sabdin, Hussein, Sued, Manurung, et al., 2018; Sabdin, Izan, Hussein, Sued, et al., 2018a; Sabdin, Hussein, & Sued, 2019; Sabdin, Hussein, Sued, et al., 2019). Achieving narrow fabrication tolerances and improved weld quality are now standard requirements for new technological developments. Most researcher studied in order to enhance its chance for automation and to get good quality weld (Adamiec et al., 2017; Fronius, 2013; Korzeniowski et al., 2013). Reliability on mechanical properties of the weld metal, metallurgical characteristics and chemical composition of the weld to ensure the quality of a weld structure. This process is characterized by significantly reduced heat input, which is essential for welding thin-walled automotive steels without causing excessive distortion or burn-through (Goecke, 2005; Kah & Martikainen, 2012).

Response Surface Methodology (RSM) is an effective optimization technique used to determine the desired weld bead geometry. By using regression analysis and graphical methods, RSM helps determine the optimal welding

process model (Kiaee & Aghaie-Khafri, 2014; Srivastava & Garg, 2017a, 2017b). Researchers mentioned RSM provides good results over regular experimental regions, or with no irregular points (Biber et al., 2024)(Correia et al., 2004; Myers, 2012; Said et al., 2015). Researcher Sahil Angaria et al (Angaria et al., 2017) Studies application of RSM in the central composite design to perform optimize hardness in GMAW experiments and shows significant results.

The objective of this study is to investigate the effect of current, voltage, and welding speed on the bead geometry of thin-plate cold-rolled steel joints welded using the ColdArc method. Unlike conventional surfacing or cladding techniques that deposit thick layers for wear resistance, this research focuses on lap-joint welding optimization for thin-sheet applications. Mechanisms related to the improvement of weld bead size and shape were investigated by focusing on welding parameters established through the Central Composite Design (CCD) method.

2. Materials and Methods

2.1 Materials

Cold-rolled steel plates (SPCC) with thicknesses of 0.8 mm and 1.0 mm were used shown in Table 1. It is a cold rolled sheet commonly referred as a commercial quality of cold rolled steel sheets (Park et al., 2017).

2.2 Design of Experiments

This investigation focused on three primary variables welding current (A), arc voltage, and travel speed (WS), each evaluated across three distinct levels. A Central Composite Design (CCD) was employed with axial points (α) account for values outside the standard low/high ranges. The design matrix comprises of full replication of $2^4 = 16$, Factorial designs. All welding parameters in levels define is in cube points and combination of each welding parameters at either is highest value (+1) or lowest (-1) in Table 2. Total numbers of 20 experiments were conducted that create estimation of linear, quadratic and two-way interactive effects of process parameters on weld bead geometry in Table 3.

Table 2. The selection of response and variable in the experimental design

Factors	Level	
	Low (-1)	High (+1)
Ampere (A)	32	48
Voltage (V)	6.50	14.50
Welding speed (mm/min)	350	750

Table 3. Design Matrix

Experiment Run	Current (A)	Voltage (V)	Welding speed (mm/min)
1	40.00	3.77	550
2	32.00	6.50	750
3	48.00	6.50	750
4	40.00	10.50	890
5	26.55	10.50	550
6	32.00	6.50	350
7	32.00	14.50	750
8	40.00	10.50	550
9	40.00	10.50	550
10	40.00	10.50	550
11	40.00	10.50	550
12	40.00	10.50	550
13	40.00	10.50	550
14	48.00	6.50	350
15	48.00	14.50	750
16	53.45	10.50	550
17	40.00	17.23	550
18	32.00	14.50	350
19	40.00	10.50	210
20	48.00	14.50	350

Table 1. Chemical composition of the cold-rolled material

Elements	C	Si	Mn	P	S	Cr	Mo	N	Al	Cu	Co	Fe
Cold Rolled	0.045	0.009	0.2	0.01	0.006	0.006	0.006	0.013	0.051	0.013	0.024	Bal.

3. Experimental Setup

A lap joint geometry was selected for the steel specimens to facilitate a more straightforward welding process using the robotic ColdArc system. This specific configuration was implemented to accommodate the maneuverability of the GMAW robotic arm during the welding operation (Germany: EWM, model: alpha Q 352 pulse) (Sabdin, Izan, Hussein, Sued, et al., 2018b) . Table 4 shows dimensions of each plate were set up in these experiments. The study utilized an ER70S-6 filler wire with a diameter of 1.0 mm, known for delivering consistent arc stability and a high-quality surface finish (Sabdin et al., 2017; Sabdin, Hussein, 2018, & 2018, 2018; Sabdin, Izan, Hussein, Sued, et al., 2018a). This mild steel wire is a high-performance filler material, especially for robotic or mechanized welding, and it is commonly used for construction, shipbuilding, automotive parts and fabrication (Nazir, 2023). It can produce smooth and constant arc with low spatter and produce smooth surface finish in the weld bead. Figure 1 shows the schematic of the weld bead geometry measurement. The results obtained was then analyzed using Minitab® Statistical Software version 17.

Table 4: Material Setup

Materials	Size	Represent
Cold Rolled	250 mm x 50 mm x 0.8 mm	Plate 1
Cold Rolled	250mm x 50 mm x 1mm	Plate 2

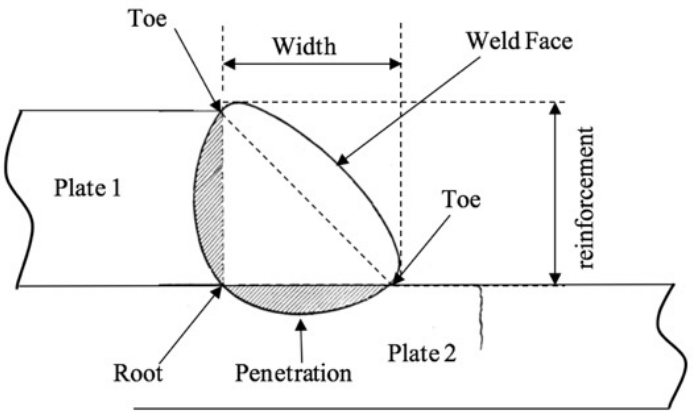

Figure 1. Weld bead geometry

4. Results and Discussion

Figure 2 shows two samples of photographs of welded resulting ColdArc weld of lap joint of cold rolled plates. Overall, the welding process produced joints with negligible levels of spatter. Data analysis Table 5 revealed that the maximum bead width reached 2.1 mm in run 19, whereas the minimum width of 1.55 mm was recorded in sample 2. The height weld was obtained at sample 1 at 1.83 mm and lowest at sample 20 is 1.15 mm. Average width and height weldment geometry size is 1.88 mm and 1.75 mm.

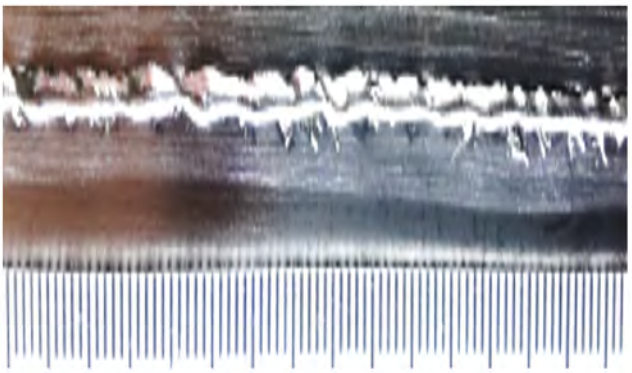

(a)

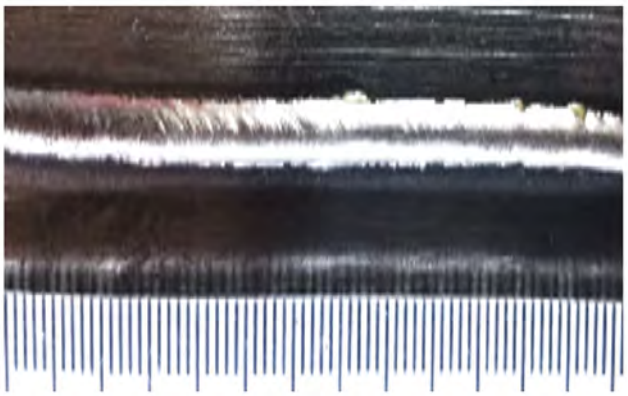

(b)

Figure 2. Sample photographs of the welded joints for a) sample 1 and, b) sample 2

Table 5. The results for experimental design

Run	Current (A)	Voltage (V)	Welding speed (mm/ min)	Bead size	
				Width (mm)	Height (mm)
1	40.00	3.77	550	1.6	1.83
2	32.00	6.50	750	1.55	1.62
3	48.00	6.50	750	1.64	1.5
4	40.00	10.50	890	1.63	1.48
5	26.55	10.50	550	1.67	1.5
6	32.00	6.50	350	1.72	1.47
7	32.00	14.50	750	1.73	1.4
8	40.00	10.50	550	1.8	1.46
9	40.00	10.50	550	1.81	1.4
10	40.00	10.50	550	1.84	1.38
11	40.00	10.50	550	1.9	1.33
12	40.00	10.50	550	1.8	1.35
13	40.00	10.50	550	1.83	1.47
14	48.00	6.50	350	1.82	1.41
15	48.00	14.50	750	1.9	1.43
16	53.45	10.50	550	1.94	1.39
17	40.00	17.23	550	1.98	1.3
18	32.00	14.50	350	2	1.28
19	40.00	10.50	210	2.1	1.22
20	48.00	14.50	350	2	1.15

4.1 Analysis of Variance (Anova)

The ANOVA technique was employed to quantify the individual contributions of each welding parameter toward the total variation in the response. This statistical method serves as a primary tool for evaluating the significance and impact of each input variable on the final weld quality. Model reliability was confirmed by a non-significant "Lack of Fit" value, suggesting that the mathematical equations are suitable for predicting the experimental outcome. In this study, the significance of welding parameters of current, voltage and welding speed were determined using Minitab® Statistical Software version 17.

4.2 Mathematical Mode1: Regression Analysis Bead Width

The analysis of variance results for response surface cubic model for bead width is given in table 6. The ANOVA results for the bead width and bead height models showed high significance with F-values of 54.91 and 8.82, respectively. The "Lack of Fit" was not significant, indicating the models are reliable for navigating the design space. Values of “Prob > F” less than 0.05 indicates that model terms are significant (Srivastava & Garg, 2017a). There is only 0.01% chance that large F-Value could occur due to noise. Values greater than 0.1 indicates the model terms are not significant (Prabaharan et al., 2014). If there are many insignificant model terms, model reduction may improve the model. The “Lack of Fit F-value” of 1.93 shows that lack of fit is not significant relative to the pure error. There is a 24.19% chance that large F − lack of fit value could occur due to noise(Kiaee & Aghaie-Khafri, 2014).

Table 6. ANOVA table for Bead width (BW)

Source	Sum of Squares	df	Mean Square	F-value	p-value	
Model	0.3890	3	0.1297	54.91	< 0.0001	significant
A-current	0.0485	1	0.0485	20.55	0.0003	
B-voltage	0.1734	1	0.1734	73.44	< 0.0001	
C-welding speed	0.1671	1	0.1671	70.73	< 0.0001	
Residual	0.0378	16	0.0024			
Lack of Fit	0.0306	11	0.0028	1.93	0.2419	not significant
Pure Error	0.0072	5	0.0014			
Cor Total	0.4268	19				

Table 7 shows Pred. R-squared" of 0.8521 is in sensible agreement with the 'Adj. R-squared' of 0.8949. "Adq precision" quantifies the signal to noise ratio. A ratio greater than 4 is desirable (Prabaharan et al., 2014). But here the value of "Adeq precision" is 26.0337 that indicates an adequate signal. Therefore, this model can be used to navigate the design space. The graph of predicted bead width and actual bead width is shown in Figure 3.

Table 7. Model Summary Statistic of BW

Std. Dev.	0.0486	**R^2**	0.9115
Mean	1.81	**Adjusted R^2**	0.8949
C.V. %	2.68	**Predicted R^2**	0.8521
Press	0.0631	**Adeq Precision**	26.0337

The mathematical model for the bead width response was developed using multiple linear regression, given by the equation (1):

$$\text{Bead Width} = \beta_0 + \beta_1 A + \beta_2 B - \beta_3 C \quad (1)$$

In equation 1, in which Bead width is the responses value and β0 is the value for the intercept represent the average of all actual responses. While β1, β2 and β3 is the coefficient of factor A, B and C their interaction. The final equation is given by equation 2:

$$\text{Bead width} = 1.523 + 0.0075\,A + 0.0282B - 0.5529C \quad (2)$$

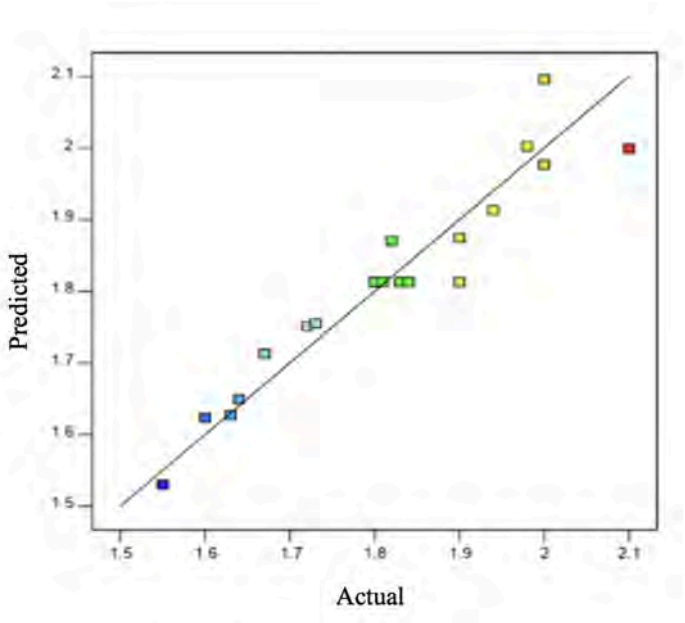

Figure 3. Predicted vs Actual bead width

4.3 Mathematical Model: Regression Analysis Bead Height

Table 8 shows indicated model F with significant 8.82 value. Value of "Prob > F" less than 0.05 indicates that model terms are significant (Srivastava & Garg, 2017a). There is only 0.01% chance that large F-Value could occur due to noise. Values greater than 0.1 indicates the model terms are not significant (Saini et al., 2024)(Prabaharan et al., 2014). If there are many insignificant model terms, model reduction may improve the model. The "Lack of Fit F-value" of 1.71 shows that lack of fit is not significant relative to the pure error. There is a 28.52% chance that large F − value of lack of fit could occur due to noise(Kiaee & Aghaie-Khafri, 2014).

The given Table 9 shows Pred. R-squared" of 0.3812 is in sensible agreement with the 'Adj. R-squared' of 0.7875. "Adeq precision" quantifies the signal to noise ratio. A ratio greater than 4 is desirable (Prabaharan et al., 2014). But here the value of "Adeq precision" is 12.0474 that indicates an adequate signal. Therefore, this model can be used to navigate the design space. The graph of predicted bead height and actual bead height is shown in Figure 4.

Table 8. ANOVA table for Bead Height

Source	Sum of Squares	df	Mean Square	F-value	p-value	
Model	0.3503	9	0.0389	8.82	0.0011	significant
A-current	0.0158	1	0.0158	3.59	0.0875	
B-voltage	0.1949	1	0.1949	44.16	< 0.0001	
C-welding speed	0.0850	1	0.0850	19.26	0.0014	
AB	0.0008	1	0.0008	0.1813	0.6793	
AC	0.0012	1	0.0012	0.2833	0.6062	
BC	0.0032	1	0.0032	0.7252	0.4144	
A^2	0.0005	1	0.0005	0.1224	0.7337	
B^2	0.0340	1	0.0340	7.70	0.0196	
C^2	0.0109	1	0.0109	2.46	0.1476	
Residual	0.0441	10	0.0044			
Lack of Fit	0.0278	5	0.0056	1.71	0.2852	not significant
Pure Error	0.0163	5	0.0033			
Cor Total	0.3945	19				

Table 9 shows Pred. R-squared" of 0.8521 is in sensible agreement with the 'Adj. R-squared' of 0.8949. "Adq precision" quantifies the signal to noise ratio. A ratio greater than 4 is desirable (Prabaharan et al., 2014). But here the value of "Adeq precision" is 26.0337 that indicates an adequate signal. Therefore, this model can be used to navigate the design space. The graph of predicted bead width and actual bead width is shown in Figure 3.

Table 9. Model Summary Statistic of Bead Height

Std. Dev.	0.0664	**R^2**	0.8881
Mean	1.42	**Adjusted R^2**	0.7875
C.V. %	4.68	**Predicted R^2**	0.3812
Press	0.2441	**Adeq Precision**	12.0474

Mathematical model : Regression analysis of Bead height Quadratic equation represent by :

$$\text{Bead Height} = \beta_0+\beta_1A+\beta_2B-\beta_3C+\beta_4AB+\beta_5AC+\beta_6BC+\beta_7A^2+\beta_8B^2-\beta_9C^2 \quad (3)$$

In equation 3, in which Bead Height is the responses value and β_0 is the value for the intercept represent the average of all actual responses. While β_1, β_2, β_3, β_4, β_5, β_6, β_7, β_8 and β_9 is the coefficient of factor A, B and C their interaction. The final Mathematical model equation in terms of coded factors were as follows:

$$\text{Bead Height} = 2.39422-0.019488A-0.119835B + 0.57468C + 0.000312AB + 0.007812AC + 0.025000BC + 0.000096A^2 + 0.003034B^2 -0.686610C^2 \quad (4)$$

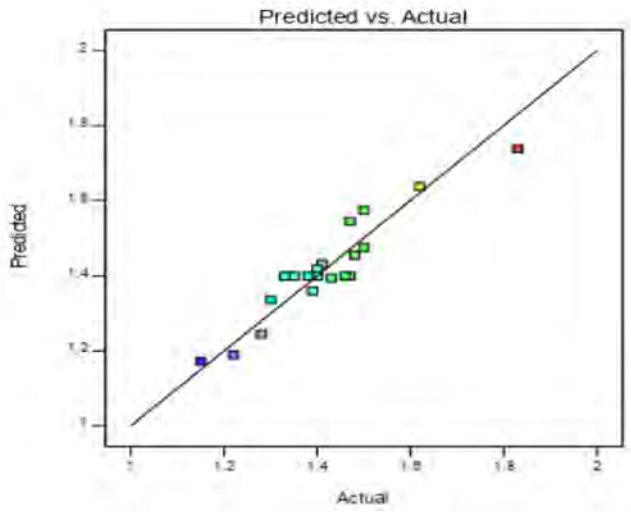

Figure 4. Predicted vs Actual Bead height

4.4 Optimization of Results

The optimized results are given in Table 10 with their desirability. Analysis of the desirable solutions indicated that the first experimental run achieved the highest desirability rating for the target responses in Table 11 (Kiaee & Aghaie-Khafri, 2014; Vedrtnam et al., 2018). Beyond identifying single optimal points for bead dimensions, the Response Surface Methodology (RSM) provided a comprehensive range of ideal operating parameters. The generated surface plots illustrate the complex relationships between input variables on the Z-axis, aiding in the visualization of the optimization landscape. The optimum values of bead width and bead height is shown in the response curves in Figure 5 and 6 respectively. RSM is a technique for optimization of process parameters. By using RSM plots, it is easy to optimize welding process variables to achieve most favorable bead geometries i.e., bead height, bead width and depth of penetration. In the surface plots shown in Figure 5 and 6, 7 two parameters are shown on X and Y axes, and the responses are shown on Z axis.

Table 10: Process Parameter & Response Constraint

Name	Goal	Lower Limit	Upper Limit	Lower Weight	Upper Weight	Importance
A: current	is in range	32	48	1	1	3
B: voltage	is in range	6.5	14.5	1	1	3
C: welding speed	is in range	0.35	0.75	1	1	3
Bead Width	minimize	1.6	3.5	1	1	3
Bead Height	minimize	1.65	3	1	1	3

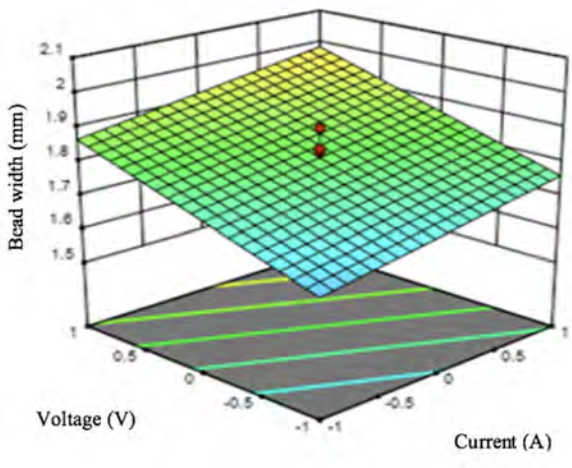

Figure 5. Response graph surface methodology effect Voltage and current on Bead Width

4.5 Confirmation Test

The optimized parameters have been verified by conducting confirmatory tests. For confirmatory test, new set of process parameters were considered for welding. Physically, the reduced heat input of the ColdArc process minimizes the melting of the base metal, which is crucial for maintaining the geometry of thin lap joints in Figure 7. The interaction between current and voltage was found to be the most influential factor in determining bead dimensions. Weldment area and the test results are compared to the predicted values as given in Table 12. Validation of the optimized settings showed that the discrepancy between the theoretical predictions and experimental observations was below 2%. Since the recorded error falls within an acceptable statistical margin, the established models are proven to be highly reliable for achieving minimal bead height and width (Srivastava & Garg, 2017b). Physical measurements of the confirmed weld samples demonstrated that the low heat input characteristic of ColdArc is vital for preserving the structural integrity of thin plates.

Table 12. Comparative results of conformity test

No	Parameter	Optimized parameter (predicted values)	Experimentally observed values	% error
1	Current (A)	32	32	-
2	Voltage (V)	6.5	6.5	-
3	Welding speed (m/min)	0.75	0.75	-
4	Bead Width (mm)	1.530	1.55	1.307
5	Bead Height (mm)	1.637	1.62	1.038

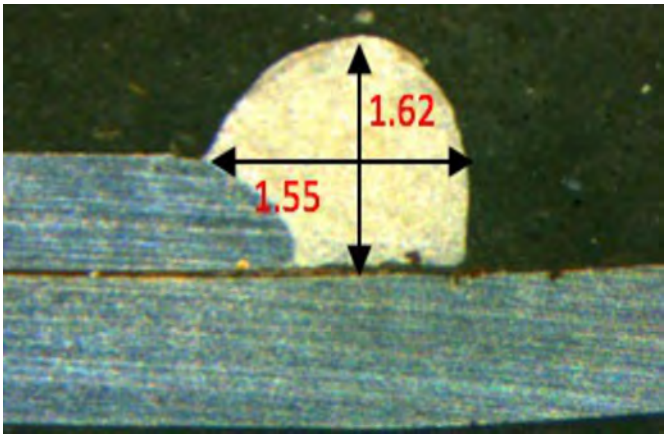

Figure 7. Weld bead confirmation by experimental observed value.

5. Conclusions

In general, it was found that dissimilar SPCC steel plates in lap joint configuration can be successfully welded using the ColdArc technology. The weldment result was consistent with minimal spatter levels. Experiments were done on basis of central composite design technique. Recorded data were used to find out optimal bead geometry i.e. bead height, bead width and depth of penetration. The following conclusions can be drawn from this study:

1. ColdArc technology using the GMAW platform can successfully weld dissimilar cold-rolled mild steel sheets in a lap joint configuration with minimal spatter.
2. The application of Response Surface Methodology (RSM) proved to be an efficient and practical approach for identifying optimal welding settings to achieve minimal bead dimensions.
3. Among the variables analyzed, the interplay between welding current and voltage emerged as the most significant factor affecting the results.
4. The optimized results were validated through confirmation tests, with error rates of less than 2%, proving the models are reliable.
5. Future research should explore the metallurgical properties and fatigue life of these thin-sheet joints to further enhance automotive manufacturing quality.

Acknowledgements

The authors gratefully acknowledge the technical support provided by the Advanced Technology Training Centre (ADTEC), Department of Manpower Malaysia (JTM), Tangkak Campus, Johor, Malaysia; the Scientific and Industrial Research Institute of Malaysia (SIRIM), Shah Alam; the Welding Institute (TWI), Sungai Buloh; and the Faculty of Manufacturing Engineering, Universiti Teknikal Malaysia Melaka (UTeM).

References

Adamiec, J., Pfeifer, T., & Rykała, J. (2017). Modern methods of aluminum alloys welding. 176(2011), 35–38. https://doi.org/10.4028/www.scientific.net/SSP.176.35

Angaria, S., Rao, P. S., & Dhami, S. S. (2017). Application of RSM to Optimize MIG welding Process Parameters for Hardness. International Journal of Emerging Technologies in Engineering Research, 5(9), 31–36.

Basak, S., Khansole, A., & Ghosh, A. (2025). Advances in Arc Welding Process. In B. Acherjee, D. Zhao, & F. A. O. Fernandes, Advanced Welding Technologies (1st ed., pp. 1–40). CRC Press. https://doi.org/10.1201/9781003499688-1

Biber, A., Sharma, R., & Reisgen, U. (2024). Robotic welding system for adaptive process control in gas metal arc welding. Welding in the World, 68(9), 2311–2320. https://doi.org/10.1007/s40194-024-01756-y

Correia, D. S., Gonçalves, C. V., Sebastião, S. C., & Ferraresi, V. A. (2004). GMAW Welding Optimization Using Genetic Algorithms. Journal of the Brazilian Society of Mechanical Sciences and Engineering, 26(1), 28–33. https://doi.org/10.1590/s1678-58782004000100005

Fronius. (2013). CMT : Cold Metal Transfer A hot & cold process makes.

Goecke, S. F. (2005). Low Energy Arc Joining Process for Materials Sensitive to Heat. In EWM HIGHTEC WELDING GmbH.

Kah, P., & Martikainen, J. (2012). Current Trends In welding Processes And Materials: Improve In effectiveness. Rev. Adv. Mater. Sci., 30, 189–200.

Kah, P., Suoranta, R., & Martikainen, J. (2012). Advanced gas metal arc welding processes. International Journal of Advanced Manufacturing Technology. https://doi.org/10.1007/s00170-012-4513-5

Kiaee, N., & Aghaie-Khafri, M. (2014). Optimization of gas tungsten arc welding process by response surface methodology. Materials and Design, 54, 25–31. https://doi.org/10.1016/j.matdes.2013.08.032

Korzeniowski, M., Piwowarczyk, T., Kustroń, P., & Czubak, A. (2013). Low-Energy Welding Methods Used For Semi-Automatic Thin-Walled Automotive Steels. Advances in Materials Science, 13(3), 17–25. https://doi.org/10.2478/adms

Mondal, A., Saha, M. K., Hazra, R., & Das, S. (2016). Influence of heat input on weld bead geometry using duplex stainless steel wire electrode on low alloy steel specimens. Cogent Engineering, 3(1), 1–14. https://doi.org/10.1080/23311916.2016.1143598

Myers, W. (2012). Response Surface Methodology. In Encyclopedia of Biopharmaceutical Statistics, Third Edition (Issue May). https://doi.org/10.1201/b14674-189

Nazir, D. S. (2023). Latest Developments in MIG Welding—A Review. International Journal for Research in Applied Science and Engineering Technology, 11(6), 1138–1141. https://doi.org/10.22214/ijraset.2023.53791

Park, J., Kang, M., Sohn, S. S., Kim, J. S., Kim, H. S., Cho, W. T., & Lee, S. (2017). Tensile properties of cold-rolled TWIP-cored three-layer steel sheets. Materials Science and Engineering A, 686(November 2016), 160–167. https://doi.org/10.1016/j.msea.2017.01.046

Prabaharan, C., Venkatachalam, P., Suresh Kumar, K., & Lenin, K. (2014). Parametric optimization of gas tungsten arc welding processes by using factorial design approach. Journal of Scientific and Industrial Research, 73(6), 415–420.

Sabdin, S. D., Hussein, N., 2018, M. S.-… R. D., & 2018, U. (2018). Weld bead reinforcement on cold rolled carbon steel sheet joint using ColdArc technology. Proceedings of Mechanical Engineering Research Day 2018, 2018(May), 197–198

Sabdin, S. D., Hussein, N. I. S., & Sued, M. K. (2019). A Review on Thin Plates Joining Method Using Arc Welding as The Heat Sources. Journal of Industry, Engineering and Innovation, 1(2), 1–6.

Sabdin, S. D., Hussein, N. I. S., Sued, M. K., Ayob, M. S., M.Fadzil, & Rahim, M. A. S. A. (2019). Effects of ColdArc welding parameters on the tensile strengths of high strength steel plate investigated using the Taguchi approach. Journal of Mechanical Engineering and Sciences, 13(2), 4846–4856. https://doi.org/10.1017/CBO9781107415324.004

Sabdin, S. D., Hussein, N. I. S., Sued, M. K., & Ayof, M. N. (2018). Joining of Thin Plates using Various Arc Welding Heat Sources – A Review. Journal of Advanced Manufacturing Technology, Vol 12, 20(iDECON 2016), 357–370.

Sabdin, S. D., Hussein, N. I. S., Sued, M. K., Manurung, Y. H. P., & Jamaluddin, M. F. (2018). Numerical modelling verification of temperature distribution in ColdArc welding of thin plate. International Journal of Engineering & Technology, 7(4.36), 1569–1573.

Sabdin, S. D., Izan, N., Hussein, S., & Sued, M. K. (2017). Parameters and properties relationship of thin steel plate joint using low energy arc welding. Proceedings of Innovative Research and Industrial Dialogue 2016, 2017(1), 169–170.

Sabdin, S. D., Izan, N., Hussein, S., Sued, M. K., Ayof, M. N., & Shah, M. A. (2018a). The effect of voltage on weldment size cold rolled steel sheet joint using low arc joining technology. Proceedings of Innovative Research and Industrial Dialogue 2018, (July), 1–2.

Sabdin, S. D., Izan, N., Hussein, S., Sued, M. K., Ayof, M. N., & Shah, M. A. (2018b). The effect of voltage on weldment size cold rolled steel sheet joint using low arc joining technology. Proceedings of Innovative Research and Industrial Dialogue 2018, (July), 1–2.

Said, K. A. M., Yakub, I., & Amin, M. A. M. (2015). Overview of Response Surface Methodology (RSM) in Extraction Process. Journal of Applied Science & Process Engineering, 2(April), 279–287. https://doi.org/10.3850/978-981-09-4587-9_p38

Saini, A., Rehalia, V., Talgotra, A., & Shobit. (2024). Design and Assessment of Automatic Arc Welding Machine Based on Programming Logic Controller. International Journal of Engineering and Management Research, 14(6), 31–37. https://doi.org/10.31033/ijemr.14.6.31-37

Srivastava, S., & Garg, R. K. (2017a). Process parameter optimization of gas metal arc welding on IS : 2062 mild steel using response surface methodology. Journal of Manufacturing Processes, 25, 296–305. https://doi.org/10.1016/j.jmapro.2016.12.016

Srivastava, S., & Garg, R. K. (2017b). Process parameter optimization of gas metal arc welding on IS : 2062 mild steel using response surface methodology. Journal of Manufacturing Processes, 25, 296–305. https://doi.org/10.1016/j.jmapro.2016.12.016

Vedrtnam, A., Singh, G., & Kumar, A. (2018). Optimizing submerged arc welding using response surface methodology, regression analysis, and genetic algorithm. Defence Technology, 14(3), 204–212. https://doi.org/10.1016/j.dt.2018.01.008

Wordofa, T. N., Perumalla, J. R., & Sharma, A. (2024). An artificial intelligence system for quality level–based prediction of welding parameters for robotic gas metal arc welding. The International Journal of Advanced Manufacturing Technology, 132(7–8), 3193–3212. https://doi.org/10.1007/s00170-024-13518-7

Zamzami, I. Al, Davison, J. B., & Susmel, L. (2017). Static Strength of aluminium-to-steel thin welded joints: Preliminary results. BSSM 12th International Conference on Advances in Experimental Mechanics, 3–4.

IJAMMP

Bending The Rules: A Review of Cutting-Edge Sheet Metal Forming Technologies

Mohd Aidil Shah bin Abdul Rahim[1,*], Fazlul Rahman bin Mohd Yunus[1], Muhammad Faqrul bin Mohd Zaidi[1] and Saifuldin bin Sabdin[2]

REVIEW ARTICLE

ARTICLE INFO

Keywords:

Hybrid Manufacturing; Incremental Sheet Forming; Industry 4.0; Metal Forming; Sustainable Manufacturing

Article History

Received:
Revised:
Accepted:
Published:

ABSTRACT

Sheet metal forming (SMF) forms an important part of contemporary manufacturing processes, enabling more complex and lightweight components for aerospace, automotive and infrastructure applications. The overall overview of this paper discusses the evolution of technology in sheet metal fabrication from conventional methods to highly precise digitalized systems. This study systematically classifies a host of applications, including stamping, deep drawing, and hydroforming, incremental sheet forming (ISF) and laser-based deformation, in order to compare their overall mechanical fundamentals including plastic deformation, strain hardening and fracture mechanics that govern structural performance. Analysis revolves around the transition of the field to high strength ultra-light alloy and sophisticated surface treatments as prescribed by the modern sustainable goals. Evidence indicates that the melding of Artificial Intelligence (AI), Digital Twin, and Additive Manufacturing (AM) brings about unprecedented opportunities to maximize manufacturing capacities and minimize systemic waste. The future trends will see a transition towards Hybrid Manufacturing in which the AM-produced rapid tooling and conformal cooling channels embedded into traditional formative processes surpass the existing geometric and thermal limitations. In addition, autonomous closed-loop control and real-time springback compensation driven by multi-physics FEA and machine learning are becoming the industry trends. The circular economy model in terms of bio-lubricants and high-recyclability alloys is recognized as the key to overcoming the current situation and, in turn, forming the basis to a sustainable and resilient global manufacturing structure.

1. Background And Functional Framework

Forming sheets of metal is the cornerstone of modern manufacturing, enabling the synthesis of complex lightweight parts of significance for the aerospace, automotive and infrastructure industries. Manufacturers convert flat metal sheets into dedicated geometries, making it possible to make complex parts with accurate dimensions, providing a greater ability for intricate designs at a lower price than alternative routes. Previous studies acknowledge the important role of these processes in producing structures with less material waste and simultaneously higher strength and less weight.

For optimizing industrial applications, the classification of these processes—breaking them down into mechanical, thermal, or chemical interventions—is essential. The methods can be further divided into sub-categories (bending, drawing, stretching, and punching) and differentiated by production scale, i.e., batch versus continuous.

1. Tool Department (Die), Proton Institute @ ADTEC Melaka, 78000 Alor Gajah, Melaka, Malaysia
2. Metal Fabrication Department, Advance Training Center (ADTEC), Tangkak Campus, KM 43, Jalan Segamat, Sagil, 84900 Tangkak, Malaysia

Corresponding author : aidilshah@jtm.gov.my

Current industrial practice shows that the industry is experiencing an organic and transformative change towards incorporation of Industry 4.0 which entails technological convergence of artificial intelligence (AI) and digital twins, which presents novel potential to deal with the limitations and systemic problems arising out of the resource scarcity and inherent inefficiencies.

1.1 Traditional Die-Based Methodologies: Stamping And Deep Drawing

The heart of conventional metal forming is done with stamping and deep drawing, where a die drives a process until the formation of defined shapes in a flat surface. Stamping is an important method for high precision and efficiency in mass production and some of the major limitations are tooling cost. The successful execution of these operations relies almost entirely on die design quality and dimensional integrity where the finished part is concerned. Although these existing methods are efficient, important research gaps remain:

- Adaptive Control: The involvement of smart materials on multi-material hybrids is not explored well enough, or into the real-time adaptive control systems.

- Mitigating Defect: There is a significant gap in real-time correction over stochastic defects (wrinkling and springback) in non-linear, high-strength lightweight alloys.
- Friction and thermal dynamics: There is no comprehensive understanding of the dynamic interaction between tool-surface frictions on the one hand, and localized temperature gradients on the other in such high-speed, automated environments.
- Sustainability: There is an unresolved need for standardized predictive models for recycled metallic feedstock's, so that they can comply well with the circular economy mandates.

Recent studies have begun to address these complexities; Chidambaram and Jayaprakash (2023) focused on embedding smart materials into manufacturing, while Liu et al. (2023) and Oveisi et al. (2024) demonstrated the efficacy of digital twin-driven optimization and warm hydroforming for enhancing formability.

1.2 Advanced Deformation Dynamics: Bending, Hydrofoming, And Roll Forming

Most modern fabrication techniques such as bending, hydroforming, and roll forming also provide specialized solutions for complex geometries. Bending converts workpieces to specified angular shapes, but this is often challenged by the phenomenon of springback. Hydroforming uses isostatic pressure to maintain an even material distribution and consolidate parts with significant weight reduction for aerospace and automotive applications. In contrast, roll forming offers a continuous high-volume manufacturing process for intricate linear geometries with exceptional material efficiency. Nonetheless, some technical problems persist:

- Springback Compensation: Currently there is a deficiency in real-time autonomous springback compensation of anisotropic, non-linear materials.
- Process Synchronization: For hydroforming, the real-time autonomous synchronization of pressure-to-feed ratios for non-homogeneous hybrids is still necessary.
- Roll Dynamics: Multi-modal sensor data should be combined with real-time constitutive modelling to mitigate localized buckling and twisting in roll-formed profiles.
- Tool Integrity: Long-term tool wear influence on automated robotic bending and surface integrity of pre-coated strips has not been investigated.

Innovative research by Nikhare (2021), and Liu et al. (2022) has laid the groundwork for Industry 4.0 sensor implementation to monitor strip tension and roll pressure, aiming to improve operational agility and precision.

2. Emerging Paradigms And Innovative Trajectories In Metal Fabrication

The evolution of metal fabrication underwent a foundational shift during the mid-20th century, as traditional artisanal methodologies began to transition toward numerical control (NC) systems. This era marked the first departure from manual operation, introducing programmable automation that laid the groundwork for modern precision. Expanding upon this legacy, the late 20th and early 21st centuries saw the maturation of Computer Numerical Control (CNC), which fundamentally digitized the tool-material interface. While previous reviews have extensively documented these mechanical and historical foundations (Gao et al., 2022; Liu & Hua, 2022), this study offers a fresh perspective by synthesizing the current leap from standard numerical automation toward holistic, data-driven frameworks and physical-digital convergence.

While previous comprehensive reviews have extensively documented the mechanical fundamentals and historical progression of sheet metal technologies (Gao et al., 2022; Liu & Hua, 2022), this study offers a fresh perspective by synthesizing the convergence of physical deformation with digital intelligence. Traditional literature often treats material behavior and machine control as discrete domains; however, contemporary industrial demands necessitate a metamorphic shift toward holistic, data-driven frameworks. By moving beyond the static analysis of earlier surveys, this review elucidates how the synergy between Digital Twin architectures and Additive Manufacturing is actively redefining the "formability" of high-performance alloys. Consequently, the following sections transition from established deformation principles to the emerging paradigms of Hybrid Manufacturing, where real-time computational feedback resolves the systemic inefficiencies—such as stochastic springback and thermal instability—that have historically hindered the scalability of die-less processes. To address these inefficiencies, the following discussion evaluates a spectrum of advanced methodologies, beginning with cold-state incremental strategies and transitioning toward thermal-assisted and additive-integrated forming solutions.

2.1 Incremental Sheet Forming (ISF) Dynamics and Development

Incremental Sheet Forming (ISF) is distinguished as a highly versatile manufacturing paradigm that deviates from conventional die-based stamping by employing a localized, progressive deformation strategy guided by a CNC-

controlled toolpath. This methodology offers substantial operational benefits, including heightened manufacturing flexibility, the elimination of expensive dedicated dies, and accelerated prototyping cycles, which have catalyzed its adoption for the fabrication of customized components (Ai & Long, 2022). The efficacy of the process is fundamentally contingent upon the optimization of critical parameters, specifically the tool trajectory, vertical step depth, and hemispherical tool diameter (Saleem et al., 2023).

The ISF framework primarily encompasses two variants: Single Point Incremental Forming (SPIF) and Two Point Incremental Forming (TPIF), with the latter utilizing a partial or full supporting die to enhance geometric accuracy. As illustrated in the process diagram (Fig.1), ISF utilizes a localized contact zone, allowing for the fabrication of complex geometries without the prohibitive costs of full-scale die sets. While the technique is increasingly utilized within the aerospace, medical, and automotive industries for bespoke applications, its industrial scalability is currently hindered by constraints such as suboptimal surface integrity, inherent forming limits, and relatively low production speeds (Najm & Paniti, 2024). Consequently, contemporary research is focused on the integration of robotic automation and advanced hybrid forming technologies—such as laser-assisted or ultrasonic-vibration ISF—to broaden the material compatibility and improve the dimensional precision of the finalized parts (Zhu et al., 2021).

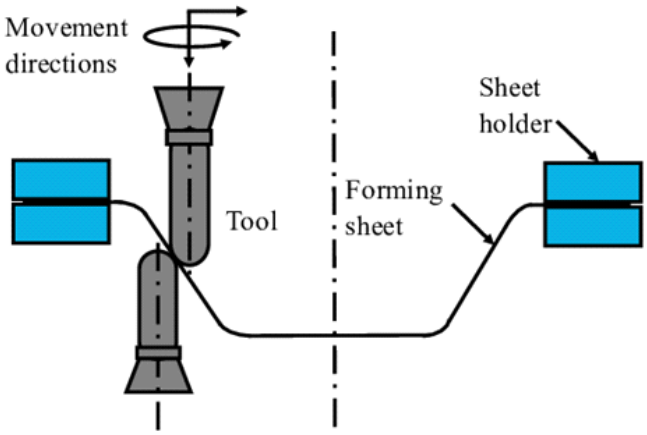

Figure 1. Localized progressive deformation in ISF: Mechanics of the hemispherical tool trajectory and vertical step depth.

While the versatility of ISF is well-documented for bespoke applications, a significant research gap remains regarding its industrial scalability for high-volume production. Current literature is predominantly focused on geometric feasibility and toolpath optimization, leaving the long-term thermomechanical stability of tools and the automated mitigation of surface roughness in a continuous production-line context largely underexplored. Where localized cold deformation reaches its geometric or material limits, thermal-mechanical interventions such as Superplastic Forming offer a viable alternative for extreme elongation.

2.2 Superplastic Forming (SPF) Principles and Industrial Utility

Superplastic Forming (SPF) is recognized as a specialized thermo-mechanical fabrication process capable of producing intricate, near-net-shape geometries with exceptional material efficiency. This technique leverages the unique rheological properties of superplastic materials, which exhibit remarkably high tensile ductility and low flow stress, allowing for extreme elongation without the onset of localized necking or premature fracture (Bordbar-Khiabani et al., 2022). To activate these superplastic characteristics, the process must be meticulously maintained under specific elevated temperatures—typically above half the absolute melting point of the metal—and low, controlled strain rates, which differentiates it from high-speed conventional stamping methods (Sridhar et al., 2023).

Due to its capacity for generating lightweight and structurally complex components, SPF is extensively utilized within the aerospace, defense, and biomedical sectors for shaping advanced titanium and aluminium alloys (Mulyadi et al., 2021). Despite its technical superiority in achieving complex contours, the widespread industrial adoption of SPF is occasionally restricted by the high cost of specialized fine-grained alloys and the characteristically long cycle times required for the material to flow into the die cavities (Prabhu et al., 2024). Current research trajectories are consequently investigating Quick Plastic Forming (QPF) and the application of grain-refinement techniques to enhance production throughput and reduce operational expenses (Rao et al., 2022). However, while SPF remains dependent on specialized dies and fine-grained alloys, the industry is increasingly looking toward non-contact, energy-driven methods like laser forming to achieve high-precision shaping without physical tooling.

2.3 Laser Forming Principles and Technological Evolution

Laser forming is an innovative, non-contact manufacturing technology that utilizes concentrated thermal energy to induce controlled plastic deformation through the establishment of steep temperature gradients across the material thickness. This process offers substantial strategic advantages, including high dimensional precision, exceptional operational flexibility, and the total elimination of hard tooling, which facilitates its deployment across diverse industrial sectors (Gisario et al., 2021). By selectively heating the workpiece surface, the resulting thermal stresses lead to localized bending or shaping,

a mechanism that is particularly advantageous for the rapid prototyping of complex geometries and the adjustment of pre-formed components (Salah et al., 2025).

Even with its advantages over classical mechanical forming, there are a number of technical problems that remain, including limited processing speeds and material absorption rates due to varying metallic alloys (Pabgaonkar et al., 2024). Studies and work currently being conducted in this area of study are mainly aimed at the tuning of laser scanning strategies and the development of closed-loop control systems to enhance the predictability of the final shape (Deswal et al., 2022). Additionally, future directions of study are rapidly focusing on integration with multi-physics simulation and machine learning for the improvement of process efficiency and extension of the compatibility of laser forming with reflective or highly conductive materials (Safari et al., 2023).

Although laser forming offers a promising die-less alternative, there is an unresolved tension between processing speed and material integrity. A critical deficiency exists in predictive modeling for multi-material hybrids, where disparate thermal expansion coefficients lead to unpredictable residual stresses—a limitation that current single-alloy studies have yet to address. The pursuit of die-less flexibility eventually converges with the capabilities of Additive Manufacturing (AM). Rather than solely deforming existing sheets, AM redefines the fabrication cycle by enabling the creation of high-complexity, functional tooling that supports traditional forming workflows.

2.4 Additive Manufacturing (AM) Integration in Sheet Metal Fabrication

The integration of Additive Manufacturing (AM) into sheet metal forming represents a profound paradigm shift, transitioning industrial workflows from rigid, subtractive methodologies toward agile, digital fabrication (Haleem & Javaid, 2019). By transcending traditional geometric constraints, AM facilitates the production of high-fidelity rapid tooling—such as dies and punches—and complex internal architectures, like conformal cooling channels, which are fundamentally unattainable through conventional machining (Tebianian et al., 2023). These advancements optimize thermal management and part quality while significantly reducing material redundancy and scrap rates, thereby aligning production with contemporary sustainability frameworks (Aslam et al., 2025). Furthermore, the synergy between specific AM modalities, such as Selective Laser Melting (SLM) and Directed Energy Deposition (DED), and hybrid manufacturing systems promises to unlock new possibilities for functional, multi-material components (Marqués et al., 2024). Ultimately, this convergence of additive processes with DIgital workflows is expected to revolutionize production cycles, enabling the rapid deployment of specialized solutions across the aerospace and medical sectors (Tebianian et al., 2023).

Despite the theoretical benefits of AM-integrated dies, current research lacks empirical longitudinal data on the wear resistance of 3D-printed tool surfaces under high-cycle industrial stamping. The interface between printed microstructures and sheet-metal tribology remains a vital but under-investigated frontier that prevents the full-scale industrialization of hybrid manufacturing systems.

3. Characterizing Material Attributes in Contemporary Forming Operations

3.1 Materials in Sheet Metal Forming: Characteristics and Selection

The efficacy of sheet metal forming operations is fundamentally predicated on the metallurgical properties of the chosen substrate, which determine its suitability for specific industrial applications. Aluminium alloys are extensively utilized within the automotive and aerospace sectors due to their high strength-to-weight ratio and inherent corrosion resistance (Hussain et al., 2021). While steel continues to be the bedrock of the manufacturing sector, its variants spanning ductile mild steels to advanced high-strength low-alloy (HSLA) and stainless steels present a versatile balance between structural integrity and fracture toughness (Muzammil et al., 2022).

In addition, copper and its alloys are desirable for their superior thermal and electrical conductivity and for the excellent formability for intricate electronic components (Zhang et al., 2023). In high-performance environments, titanium alloys are used due to their exceptional strength-to-weight performance and biocompatibility but also require specialized forming conditions (Gisario et al., 2021). Furthermore, magnesium alloys are the frontier of light weighting strategies and are characterized by significant mass reduction and favourable machinability despite challenges related to their hexagonal close-packed (HCP) structure at room temperature (Prabhu et al., 2024). In the end, the choice of material is a multi-objective optimization problem, involving cost-effectiveness, feedstock availability, and required mechanical performance, so that a comprehensive understanding of material behaviour is required for choosing the most compatible forming process (Badr et al., 2022).

3.2 Surface Treatments and Functional Coatings

Surface engineering and the application of functional coatings constitute a critical phase in the manufacturing lifecycle, significantly augmenting the performance characteristics of sheet metal components.These

treatments are primarily utilized to enhance corrosion resistance, thereby substantially extending the operational longevity of structural elements in aggressive environments (Zheludkevich et al., 2021). Specialized methodologies, such as anodizing, galvanizing, and electrostatic powder coating, are employed to improve wear resistance and surface durability, which directly correlates with the functional efficiency of the part during service (Vasiliev et al., 2023).

Beyond protective qualities, the surface finish serves as a foundational parameter that influences both the aesthetic appeal and the tribological behaviour during subsequent forming operations (Sivakumar et al., 2022). Recent scholarly focus has shifted toward the development of eco-friendly and chrome-free coatings to align with stringent environmental regulations, although the widespread industrial standardization of these "green" alternatives remains an ongoing challenge (Zhu et al., 2024). Ultimately, the strategic selection of a coating system involves a complex trade-off between technical performance and economic viability, as the associated costs significantly impact the overall feasibility of the manufacturing project (Javaid et al., 2024).

3.2 Influence of Material Properties on Forming Dynamics

Comprehensive characterization of material properties is indispensable for optimizing sheet metal forming outcomes and ensuring structural reliability. Primary mechanical attributes—specifically yield strength, ductility, and hardness—serve as the foundational determinants for establishing forming limits and predicting potential fracture modes (Badr et al., 2022). While elevated yield strength dictates the force requirements for achieving complex geometries, high ductility is essential to mitigate the risk of localized necking or cracking during intensive plastic deformation (Muzammil et al., 2022). Furthermore, material hardness is a critical factor influencing the rate of interfacial tool wear and the resultant surface integrity of the finalized component (Vasiliev et al., 2023).

Beyond macroscopic mechanical properties, the deformation behaviour is significantly governed by microstructural variables, including grain size, crystallographic anisotropy, and the sensitivity of the material to temperature and strain rate (Sridhar et al., 2023). Anisotropy, in particular, must be accounted for in process simulations to prevent unexpected thinning or earing in deep-drawn parts (Wang & Lin, 2021). Additionally, the nominal thickness of the sheet establishes the definitive Forming Limit Curve (FLC), necessitating a strategic equilibrium between high-performance design specifications and the economic constraints of material selection and tooling maintenance (Najm & Paniti, 2024).

Currently, characterization models for sheet metal forming rely heavily on virgin material data. There is a conspicuous absence of constitutive models that account for the stochastic property variations in recycled metallic feedstocks. This represents a major hurdle for the industry's transition to a truly circular manufacturing economy, as predicted behavior often deviates from empirical results when utilizing secondary materials.

4. Functional Deployment of Metal Forming Across Key Industrial Domains

4.1 Automotive Industry Applications and Strategic Evolution

Sheet metal forming serves as a cornerstone of automotive manufacturing, facilitating the high-volume production of body-in-white (BIW) panels, chassis components, and critical structural assemblies. The contemporary transition toward light weighting has significantly enhanced fuel economy and minimized carbon footprints, aligning the sector with global sustainability mandates (Hussain et al., 2021).

To achieve stringent dimensional tolerances and design specifications, the industry has increasingly integrated advanced high-strength steels (AHSS) and aluminium alloys, supported by the widespread implementation of robotics and automated production lines to optimize throughput and consistency (Rusu et al., 2024).

Notwithstanding all these developments, manufacturers are confronted with obstacles in performing the complex aerodynamic geometries required by contemporary car design and performance (Sheu et al., 2023). The rapid growth of electric vehicles (EVs) has also introduced new challenges, specifically regarding the integration of heavy battery enclosures and the demand for enhanced crashworthiness, which impacts traditional forming workflows (Muzammil et al., 2022).

The diagram (Fig. 2) illustrates the emerging hybrid manufacturing paradigm driven by growing demand for enhanced crashworthiness in heavy electric vehicle (EV) architectures. It integrates high-strength sheet forming with localized Additive Manufacturing (AM) reinforcements (e.g., for crush zones) and multi-material joining. This convergence enables multi-objective optimization for structural integrity and vehicle performance, providing a path to overcome constraints associated with traditional production cycles (Hussain et al., 2021; Muzammil et al., 2022). Consequently, there is a heightened focus on circular economy principles, where material selection is increasingly governed by recyclability and the lifecycle assessment of the metallic substrates used in the forming process (Javaid et al., 2024).

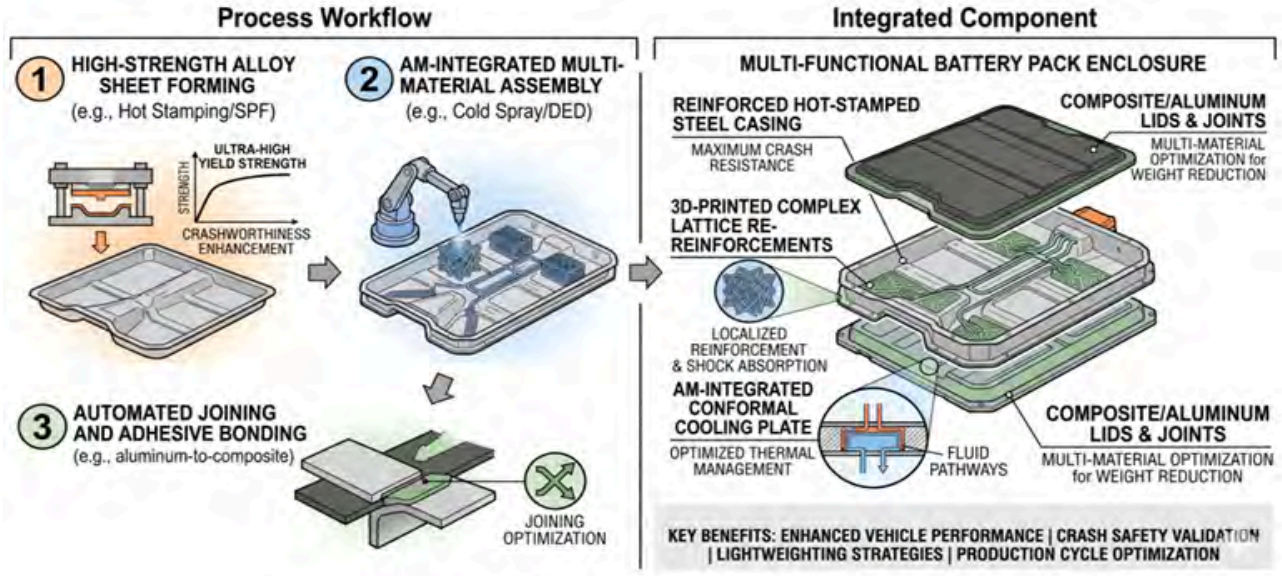

Figure 2. Advanced sheet metal workflow for EV battery enclosure optimization.

4.2 Aerospace Applications and Structural Integrity

In the aerospace sector, the imperative for weight reduction necessitates the strategic utilization of lightweight metallic substrates for the fabrication of primary structural assemblies, including fuselages, wing skins, and empennage sections. The aerodynamic efficiency of an aircraft is fundamentally linked to the precision of the forming methodologies employed, which must adhere to exceptionally stringent dimensional tolerances and rigorous safety standards (D'Amato et al., 2023). Advanced techniques such as Superplastic Forming (SPF) and Stretch Forming are critical in this domain, as they facilitate the production of streamlined contours that minimize drag and maximize structural performance (Bordbar-Khiabani et al., 2022).

Although modern advancements in digital manufacturing have resulted in an increase in throughput, the manufacturing technology needed to fabricate very intricate, integrated geometries for next-generation aircraft has been a major technical challenge. The cooperation of hybrid forming processes and multi-scale simulation is currently the most significant focus in studying material behavior under extreme deformation (Zhu et al., 2021). In the future, the development of aerospace structures will probably be driven by the integration of advanced nanocomposites and high-temperature titanium alloys, as well as the use of automated additive-formative manufacturing techniques designed to optimize both structural reliability and operational lifespan.

4.3 Electronics and Consumer Goods Fabrication

Sheet metal forming serves as a fundamental manufacturing pillar for the electronics industry, facilitating the fabrication of durable enclosures, internal chassis, and intricate structural components. In the realm of consumer electronics, the strategic application of lightweight substrates, such as aluminium and magnesium alloys, is prioritized to enhance portability and ergonomic handling (Hussain et al., 2021). The implementation of high-precision forming methodologies is essential not only to satisfy contemporary aesthetic standards but also to guarantee the structural and functional integrity of miniaturized assemblies (Zhang et al., 2023).

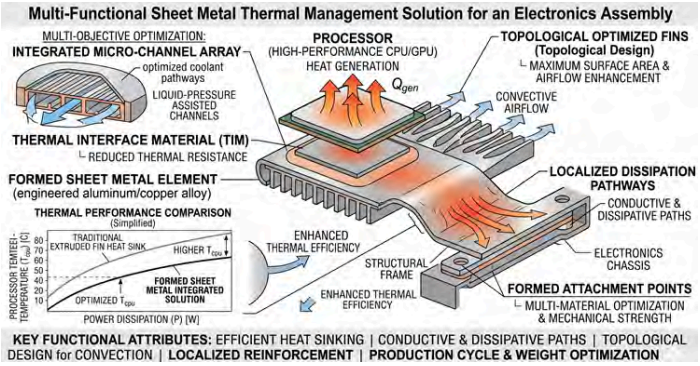

Figure 3. Integrated sheet metal heat sink and dissipation path for high performance processor.

A critical dimension of sheet metal utilization in this sector involves thermal management, where formed metallic elements are engineered to serve as efficient heat sinks and dissipation paths for high-performance processors (Liu et al., 2023). Fig. 3 shows the utilizing advanced forming (like ISF or liquid-assisted pressing) to create complex surface fin arrays for optimized convective and dissipative paths (labeled 'Topological Design' and 'Fins'). Furthermore, the adoption of flexible manufacturing techniques, such as Incremental Sheet Forming (ISF), allows for high levels of customization and the production of bespoke hardware designs (Najm & Paniti, 2024).

Aligning with global environmental mandates, the industry is increasingly emphasizing sustainability by integrating recycled metallic feedstocks and adopting "green" manufacturing workflows to reduce the ecological footprint of consumer goods (Zhu et al., 2024).

4.4 Construction and Structural Engineering Applications

Sheet metal forming serves a pivotal function in the contemporary construction industry, facilitating the fabrication of critical structural elements such as high-capacity beams and columns. The integration of lightweight metallic substrates has revolutionized architectural design by enabling superior load management and reducing the dead load on building foundations (Javaid et al., 2024). In addition, the inherent durability and corrosion resistance of modern sheet metal alloys maintain the long-term structural integrity of assets, especially in environments exposed to extreme meteorological conditions or corrosive pollutants (Vasiliev et al., 2023).

Sheet metal is a highly cost-efficient medium, allowing for highly flexible construction that can be customized according to a project's requirements (Sivakumar et al., 2022). Its industrial importance is underscored by its place in prefabricated construction, where shop-fabricated parts can be quickly assembled on-site and smoothly incorporated with hybrid materials to improve overall seismic resilience (Najm & Paniti, 2024).

Amid the shift in the sector toward Industry 4.0, sustainability has become one of its drivers where infinitely recyclable metals and low-carbon production techniques are growingly critical in aligning production to global environmental mandates and circular economy goals (Zhu et al., 2024).

5. Challenges And Future Directions In Sheet Metal Forming

5.1 Technological Challenges

With such complexities at play, there are significant technical difficulties in introducing industrial automation and robotic systems into sheet metal forming frameworks, especially around the deployment of high-fidelity real-time monitoring systems and adaptive closed-loop control architectures (Rusu et al., 2024). Moreover, existing metallurgical limitations often limit the formability and mechanical performance of substrates, leading to a challenge of achieving consistent quality standards during large-scale manufacturing (Badr et al., 2022). In addition, environmental factors and sustainability challenges in energy-intensive forming processes, as well as the capital expenditures needed to design and configure advanced tooling, further contribute to this technical challenge (Javaid et al., 2024).

Continuing this systemic inefficiency, a widening skills mismatch within the global labor market hampers efficient use and maintenance of advanced, digitally integrated machinery (Najm & Paniti, 2024). Also in the manufacturing sector is rapid prototyping and high-level customization alongside the required safety protocols that accompany fast automated systems (Zhu et al., 2021). Thus, the establishment of strong, intelligent strategies to integrate production speed with operational safety is an ongoing theme of multidisciplinary research and development (Liu et al., 2022). A strategic evaluation of contemporary forming technologies reveals a complex "problem-solution-limitation" dynamic that defines current industrial struggles. Traditional manufacturing has long grappled with the problem of rigid tooling and high material waste, a challenge ostensibly addressed by the solution of Additive Manufacturing (AM) integration and Incremental Sheet Forming (ISF). These technologies offer unprecedented geometric freedom and "die-less" flexibility; however, their industrial efficacy is tethered to significant limitations.

Specifically, the relatively low production throughput of ISF and the high surface roughness of AM-printed dies necessitate extensive post-processing, which often offsets the initial time gains. Furthermore, while Digital Twin architectures provide a solution for real-time monitoring, they are limited by the high computational cost of multi-physics simulations and the current lack of standardized constitutive models for recycled alloys. Identifying these constraints highlights the industry's central struggle: the difficult transition from small-scale, high-fidelity "smart" prototyping to the robust, high-volume consistency required for global mass production.

5.2 Socio-Economic and Environmental Metrics of Modern Forming

The transition to advanced forming methodologies is increasingly dictated by a multi-dimensional evaluation of socio-economic and environmental metrics. From an industrial standpoint, each technological shift is a direct response to a specific "pain point" that threatens commercial viability. For instance, the adoption of Incremental Sheet Forming (ISF) addresses the high capital expenditure (CAPEX) associated with small-batch prototyping, while Additive Manufacturing (AM) integration resolves the systemic downtime caused by traditional tooling lead times. Environmentally, the move toward servo-electric systems and Near-Net-Shape (NNS) manufacturing directly mitigates the energy intensity and material scrap rates of the previous century.

5.3 Environmental Considerations and Sustainable Manufacturing

Sheet metal forming has become a multidimensional issue with environmental considerations including energy efficiency, advanced waste management techniques, and a circular material economy. The carbon footprint of conventional forming processes, which is predominantly due to heavy power demands in hydraulic and mechanical presses, has spurred a move to more energy-efficient platforms, such as servo-electric presses, capable of saving up to 50% of power consumption (Mestek, 2025; Rusu et al., 2024). Furthermore, industrial by products and solid waste generation are being mitigated through the adoption of Near-Net-Shape (NNS) manufacturing and AI-powered nesting algorithms, which optimize material layout to minimize scrap (Zeng et al., 2022; Zhang et al., 2024). 12

Central to these sustainability initiatives is the recyclability of metallic substrates; for instance, recycling aluminum requires only 5% to 10% of the energy compared to primary smelting, while steel remains 100% recyclable without a loss in structural integrity (Peng et al., 2022; Jiménez, 2021). To further reduce atmospheric pollutants and volatile organic compound (VOC) emissions, the industry is increasingly replacing mineral-based oils with vegetable-based bio-lubricants or advanced dry-film and water-based solutions (Altharan et al., 2024). These eco-friendly innovations are often validated through rigorous Life Cycle Assessments (LCA), which utilize digital twin simulations to quantify environmental impacts from "cradle-to-gate," ensuring that automation and Industry 4.0 integration serve as catalysts for a lower-carbon manufacturing future (Liu et al., 2023; Javaid et al., 2024).

5.4 Innovations and Future Trajectories in Sheet Metal Forming

As intelligent materials, digital transformation, and sophisticated computational tools converge, the sheet metal forming landscape is currently experiencing a radical shift. The rise of smart materials and shape-memory alloys is changing the classical deformation limit and the application of AI algorithms in machine learning is allowing for a higher level of process optimization and predictive maintenance than to have ever been made possible before (Badr et al., 2022). They have been further supported by advanced robotics and autonomous systems that have evolved beyond basic and repetitive activities to sophisticated and adaptive operations that have increased manufacturing accuracy, as well as an improved capacity of operation (Rusu et al., 2024).

Also, the industry has recently focused on sustainable innovation which have given rise to the bio-based lubricants and high-recyclability alloys, in order to meet global legislation and systems of economy framework (Zhu et al., 2024). High performance lightweight materials as the focus for a large number of new energy-efficient transport systems is the trend of preference, with Digital Twin technology serving this, providing high quality real time process monitoring (Liu et al., 2023).

Furthermore, the availability of state-of-the-art finite element analysis (FEA) and multi-physics simulation software and computer systems enable the rapid iteration of complex designs, resulting in a manufacturing environment marked by high flexibility and customization (Wang & Lin, 2021).

These approaches are being supplemented with a strategic amalgamation of Additive Manufacturing (AM) and conventional formative technology, often described as hybrid manufacturing, and expand the range of geometric complexity, resulting in a more flexible and resilient industrial ecosystem (Sivakumar et al., 2022).

6. Conclusion

In conclusion, this review demonstrates the transformation of sheet metal forming from a purely mechanical process to a high-fidelity and digital domain in contemporary construction. Shifting away from a staid, mid-20th century tooling to more modern Hybrid Manufacturing is more than a technological innovation; it’s strategically in response to growing international needs for agility and resource utilization.

Combining established metallurgical concepts to new trends, such as Incremental Sheet Forming (ISF) and Additive Manufacturing (AM) incorporation, manufacturers can reduce the "tooling bottleneck" that has traditionally inflated lead times and capital expenditure. In the end, the comparative significance of this study is in providing a unified platform indicating that the combination of Digital Twin architectures alongside metallurgical science is the key to solving the problem of mass-customization paradox.

This convergence enables mass-production of lightweight, complex components while alleviating chronic systemic inefficiencies such as springback, material thinning. This innovation is the latest evolution in sheet metal forming to make sure sheet metal forming continues to be the backbone with sustainable footprint for this next wave of aerospace and electric vehicle (EV) structural assembly with the lean and robust profile that is critical for the new global economy.

In order for industrial resilience and to maintain the pace of progress that these leaps in technology represent, we urge future research to follow on three strategic lines of inquiry:

- Cognitive Process Integration: Development of multi-physics FEA models and machine learning algorithms for real-time, predictive springback compensation for non-linear, high strength alloys.
- Hybrid Scalability: Broadening exposure to additive-formative systems, addressing a need for 3D-printed rapid tooling to the next generation of production facilities at scale to reduce CAPEX and the lead time.
- Circular Metallurgical Ecosystems: Enabling cross disciplinary collaboration to validate the efficacy of recycled metallic feedstock's and bio-based lubricants — to ensure Industry 4.0 is inherently connected to a low-carbon, circular economy.

Acknowledgement

Special thanks towards researchers' and collaborators' perspectives and expertise supporting the completion of this study. The Proton Advance Automotive Technical Institute (ADTEC Melaka) is the receiving and special thank you for the institutional structure, equipment and specialized support resources considered in conducting this research. Besides, the authors recognize the technical staff for its help in helping a better understanding of the industrial applications presented here.

References

Abeyrathna, B., Rolfe, B., & Weiss, M. (2021). The effect of process parameters on the longitudinal strain and bow in roll forming of high strength steel. *Journal of Materials Processing Technology*, *291*, 117025. https://doi.org/10.1007/s00170-017-0164-x

Ai, S., & Long, H. (2022). A review of incremental sheet forming: Process fundamentals, material behavior, and industrial applications. *Journal of Manufacturing Processes, 75*, 1121–1135. https://doi.org/10.1016/j.jmapro.2022.01.053

Aiswarya, S., Senthil, P., & Amirthagadeswaran, K. S. (2024). A review of binder jetting and laser sintering techniques for the production of complex sheet-based metal components. *Materials Today: Proceedings, 99*, 560–567. https://doi.org/10.1016/j.matpr.2023.11.050

Al-Wajidi, A. I., Yusof, F., & Al-Zubaydi, A. (2024). Mechanical behavior and deformation mechanisms in modern alloy sheets. *Materials Chemistry and Physics, 312*, 128645. https://doi.org/10.1016/j.matchemphys.2023.128645

Altharan, Y. M., Shamsudin, S., Al-Alimi, S., Saif, Y., & Zhou, W. (2024). A review on solid-state recycling of aluminum machining chips and their morphology effect on recycled part quality. *Heliyon*, *10*(1), e34433. https://doi.org/10.1016/j.heliyon.2024.e34433

Aslam, J., Saleem, A., Lai, K., & Kim, Y. B. (2025). Critical successes factors for the adoption of additive manufacturing. *Technological Forecasting and Social Change, 213*, 124041. https://doi.org/10.1016/j.techfore.2025.124041

Awasthi, A., Saxena, K. K., & Arun, V. (2021). Sustainable and smart metal forming manufacturing process. *Materials Today: Proceedings, 44*(1), 2069–2079. https://doi.org/10.1016/j.matpr.2020.12.170

Badr, O. M., Rolfe, B., Hodgson, P., & Weiss, M. (2022). The influence of material properties and sheet thickness on the bending behavior of high-strength steels. *Journal of Materials Processing Technology, 302,* 117495. https://doi.org/10.1016/j.jmatprotec.2022.117495

Bambach, M., & Hirt, G. (2024). Digital twins in metal forming: A review. *Journal of Materials Processing Technology, 323*, 118212. https://doi.org/10.1016/j.jmatprotec.2023.118212

Bell, C., Corney, J., & Sherlock, A. (2022). Economic and technical barriers in the adoption of hydroforming. *Journal of Manufacturing Systems, 62*, 455–468. https://doi.org/10.1016/j.jmsy.2022.01.002

Bordbar-Khiabani, B., Gashti, M. P., & Mirshahi, F. (2022). Advances in superplastic forming of titanium alloys. *Journal of Alloys and Compounds, 911*, 165034. https://doi.org/10.1016/j.jallcom.2022.165034

Cao, J., & Banu, M. (2020). Opportunities and challenges in metal forming for lightweighting: Review and future work. *Journal of Manufacturing Science and Engineering*, *142*(11), 110813. https://doi.org/10.1115/1.4047732

Chidambaram, N., & Jayaprakash, N. (2023). Smart materials in additive manufacturing. *Journal of Manufacturing Processes*. https://doi.org/10.1016/j.jmapro.2023.04.055

D'Amato, G., Segreto, T. S., & Teti, R. (2023). Advanced stretching and bending analysis for titanium alloy components. *Journal of Manufacturing Processes, 95*, 214–228. https://doi.org/10.1016/j.jmapro.2023.04.015

Deswal, N., Kant, R. Machinability Analysis During Laser Assisted Turning of Aluminium 3003 Alloy. *Lasers Manuf. Mater. Process.* **9**, 56–71 (2022). https://doi.org/10.1007/s40516-022-00163-9

Duan, J., Gao, J., & Wang, Y. (2023). Advances in plastic deformation modeling. *Journal of Manufacturing Processes, 85,* 245–260. https://doi.org/10.1016/j.jmapro.2022.11.042

Facturee. (2025). Sheet metal forming report.

Fortune Business Insights. (2024/2025). Market Analysis Reports.

Gao, T., Jiao, H., & Zhang, W. (2022). A review of sheet metal forming: Classification, mechanisms, and future trends. *Materials, 15*(3), 841. https://doi.org/10.3390/ma15030841

Ghaffar, S. H., Corker, J., & Fan, M. (2022). Additive manufacturing technology implementation. *Renewable and Sustainable Energy Reviews, 156*, 111977. https://doi.org/10.1016/j.rser.2021.111977

Gisario, A., Barletta, M., & Venettacci, S. (2021). Laser forming of titanium and aluminum alloys. Optics & Laser Technology, 141, 107101. https://doi.org/10.1016/j.optlastec.2021.107101

Haleem, A., & Javaid, M. (2019). Additive Manufacturing Applications in Industry 4.0: A Review. Journal of Industrial Integration and Management, 4(4), 1930001. https://doi.org/10.1142/S2424862219300011

Javaid, M., Haleem, A., Singh, R. P., & Dhall, S. (2024). Role of virtual reality in advancing education with sustainability and identification of Additive Manufacturing as its cost-effective enabler. Sustainable Futures, 8, 100324. https://doi.org/10.1016/j.sftr.2024.100324

He, X. T., Chen, Z. P., & Sun, J. Y. (2026). Springback behavior of metal sheets. International Journal of Mechanical Sciences. https://doi.org/10.1016/j.ijmecsci.2025.110001

Hussain, M. S. J., et al. (2021). Role of aluminum alloys in aerospace. Materials Today: Proceedings, 46, 7642–7647. https://doi.org/10.1016/j.matpr.2021.01.884

Jiménez, A. (2021). Steel as a cornerstone of the circular economy. Journal of Cleaner Production, 290, 125184. https://doi.org/10.1016/j.jclepro.2020.125184

Liu, Y., Zheng, J., & He, Z. (2023). Digital twin-driven process optimization for hydroforming. Int. J. Adv. Manuf. Technol., 126, 1145–1160. https://doi.org/10.35534/ism.2024.10007

Marqués, A., et al. (2024). Analysis of Energy and Material Consumption for Aeronautical Tooling. Materials, 17(13), 3066. https://doi.org/10.3390/ma17133066

Salah, ES., Mostafa, R., Tawfik, M.M. et al. Laser forming technology: a comprehensive review of mechanisms, process optimization, and industrial applications. Int J Mater Form 18, 82 (2025). https://doi.org/10.1007/s12289-025-01943-2

Sivakumar, D., et al. (2022). Hybrid manufacturing: Combining AM with sheet metal forming. Journal of Manufacturing Processes, 82, 115–129. https://doi.org/10.1016/j.jmapro.2022.07.054

Tebianian, M., et al. (2023). A Review of the Metal Additive Manufacturing Processes. Materials, 16(24), 7514. https://doi.org/10.3390/ma16247514

Zhu, H., Ou, H., & Popov, A. (2021). Incremental sheet forming: Mechanisms and modeling. Manufacturing Letters, 30, 12–18. https://doi.org/10.1177/09544089221093306